UNIVERSIDADE FEDERAL DO PARANÁ

MATHEUS ALVES DA SILVA

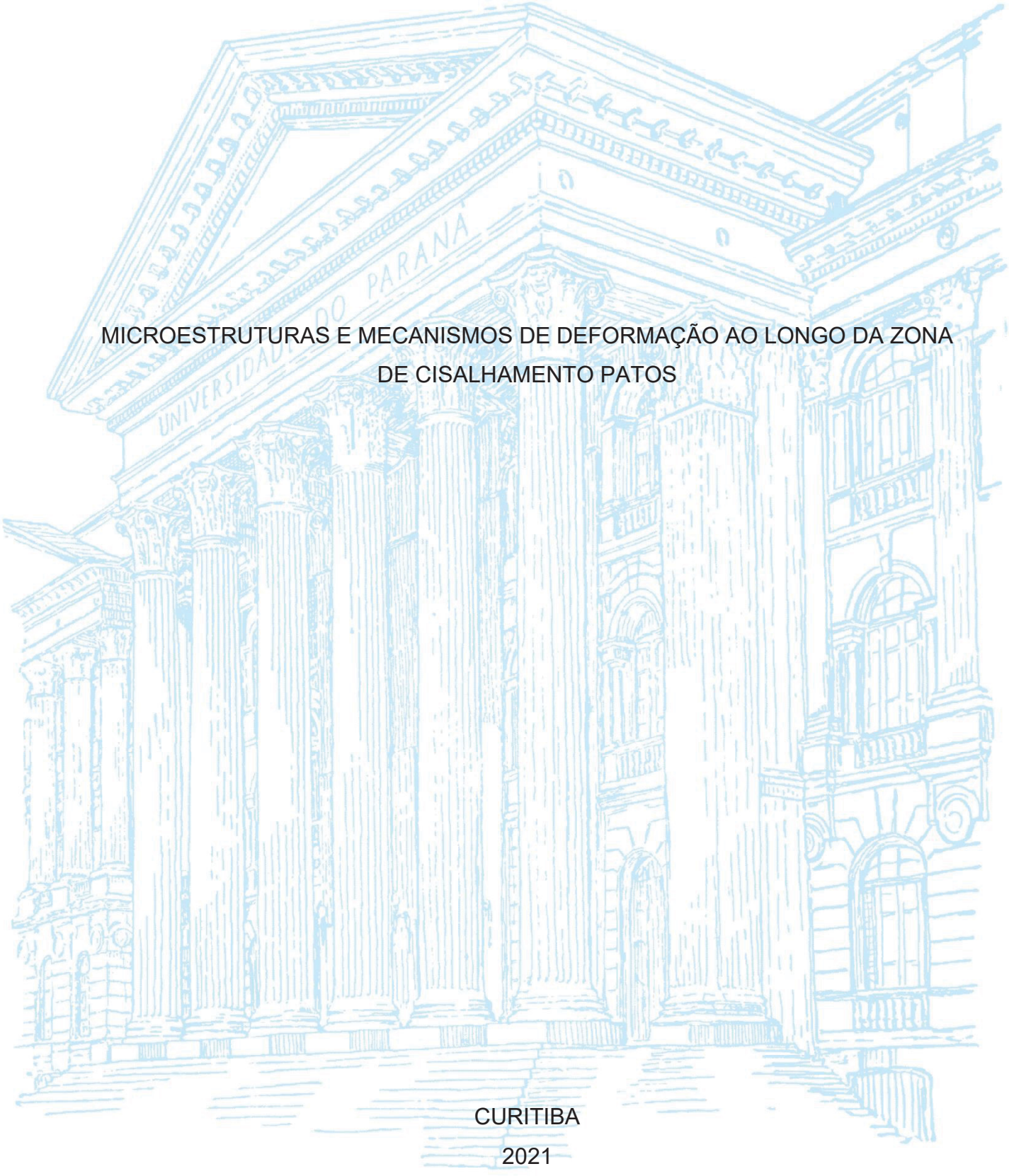

MICROESTRUTURAS E MECANISMOS DE DEFORMAÇÃO AO LONGO DA ZONA DE CISALHAMENTO PATOS

CURITIBA

2021

MATHEUS ALVES DA SILVA

MICROESTRUTURAS E MECANISMOS DE DEFORMAÇÃO AO LONGO DA ZONA DE CISALHAMENTO PATOS

Dissertação apresentada ao Programa de Pós-graduação em Geologia, Setor de Ciências da Terra, Universidade Federal do Paraná, como requisito parcial à obtenção do título de Mestre em Ciências.

Orientador: Prof. Dr. Leonardo Evangelista Lagoeiro
Coorientadora: Profa. Dra. Paola Ferreira Barbosa

CURITIBA

2018

Catalogação na Fonte: Sistema de Bibliotecas, UFPR
Biblioteca de Ciência e Tecnologia

S586m Silva, Matheus Alves da

Microestruturas e mecanismos de deformação ao longo da zona de cisalhamento Patos [recurso eletrônico] / Matheus Alves da Silva – Curitiba, 2021.

Dissertação (mestrado) - Programa de Pós-Graduação em Geologia, Setor de Ciências da Terra, Universidade Federal do Paraná.

Orientador: Prof. Dr. Leonardo Evangelista Lagoeiro
Coorientadora: Profa. Dra. Paola Ferreira Barbosa

1. Geologia. 2. Rochas - Deformação. 3. Cisalhamento. I. Universidade Federal do Paraná. II. Lagoeiro, Leonardo Evangelista. III. Barbosa, Paola Ferreira. IV.Título.

CDD 551.872

Bibliotecária: Nilson Carlos Vieira Junior CRB9/1797

TERMO DE APROVAÇÃO

Os membros da Banca Examinadora designada pelo Colegiado do Programa de Pós-Graduação GEOLOGIA da Universidade Federal do Paraná foram convocados para realizar a arguição da Dissertação de Mestrado de **MATHEUS ALVES DA SILVA** intitulada: **MICROESTRUTURAS E MECANISMOS DE DEFORMAÇÃO AO LONGO DA ZONA DE CISALHAMENTO PATOS**, sob orientação do Prof. Dr. LEONARDO EVANGELISTA LAGOEIRO, que após terem inquirido o aluno e realizada a avaliação do trabalho, são de parecer pela sua APROVAÇÃO no rito de defesa.

A outorga do título de mestre está sujeita à homologação pelo colegiado, ao atendimento de todas as indicações e correções solicitadas pela banca e ao pleno atendimento das demandas regimentais do Programa de Pós-Graduação.

CURITIBA, 20 de Dezembro de 2021.

Assinatura Eletrônica
20/12/2021 14:31:18.0
LEONARDO EVANGELISTA LAGOEIRO
Presidente da Banca Examinadora

Assinatura Eletrônica
20/12/2021 17:28:55.0
CARLOS JOSÉ ARCHANJO
Avaliador Externo (UNIVERSIDADE DE SÃO PAULO)

Assinatura Eletrônica
20/12/2021 13:23:22.0
LUIZ FERNANDO GRAFULHA MORALES
Avaliador Externo (INSTITUTO FEDERAL DE TECNOLOGIA DE ZURIQUE)

A todos que lutaram pela inclusão dos pretos e pretas nas universidades por meio das cotas e possibilitaram minha chegada até aqui

AGRADECIMENTOS

Primeiramente, eu agradeço a Deus pelo meus pais, Audifax e Teresinha de Jesus, minha irmã Eveline, minhas cachorrinhas Kiara e Nina e pelo meu orientador Leonardo Lagoeiro, a quem sou profundamente grato por todo suporte emocional, espiritual, financeiro e intelectual que me mantiveram motivado no decorrer de toda a minha pesquisa durante a minha estadia em Brasília e em Curitiba no meio de uma Pandemia.

Sou muito grato também ao meu colega de graduação e companheiro inicial de quarto, o bolado, por compartilhar sofrimentos e angustias nos primeiros meses, aos amigos que fiz na UFPR, como a Jéssica, o Luiz, a Iana e o Coxinha (amigo das nerdices), ao pessoal do LabGeol, como a Lili e a Camila, pelas discussões e momentos divertidos, aos membros do clube de dança da UFPR pelos momentos divertidos no pós-almoço e pelas festas, e, em mais do que especial, a Andressa, a quem possuo um imenso carinho, e que fez com que os meus dias nessa cidade fria e cinzenta chamada Curitiba fossem mais alegres e calorosos.

Não posso esquecer dos amigos latinos que fiz no pensionato durante a pandemia, especialmente o Guido, a Tatiana, a Carol, a Renata, a Andrea e o mascote caramelo. Else foram minha segunda família no Paraná e são pessoas que, cuja amizade, quero levar pro resto da vida.

Minha pesquisa não teria sido feita sem a colaboração da minha coorientadora, Paola Ferreira Barbosa, que me auxiliou nas análises e correções finais, e das técnicas Flávia e Bruna que preparam as minhas amostras e me ajudaram a realizar as análises de EBSD.

Agradeço profundamente ao Programa de Pós-graduação em Geologia da Universidade Federal do Paraná – PPGEO-UFPR, pela oportunidade de seguir a carreira científica, a CAPES pela bolsa concedida, que me possibilitou a minha estadia em Curitiba para terminar o meu mestrado e ao SUS, é claro, pela vacina em um período que tantos precisávamos.

Espero que eu tenha contribuído de algum modo para a ciência nacional.

"A geologia é uma cachaça"
Luiz José Homem D'El-Rey

RESUMO

Estudos microestruturais e texturais em milonitos quartzo-feldspáticos são fundamentais para compreender como a deformação é localizada na crosta intermediária. Contudo, estudos de tais naturezas em zonas de cisalhamento brasileiras são escassos. Dentre estas estruturas, se destaca o lineamento Patos, uma zona de cisalhamento com mais de 600 km de extensão de que deformou o embasamento paleoprotoerozóico da Província Borborema sob diferentes condições de temperatura. De modo a compreender os processos no estado sólido responsáveis por localizar e acomodar a deformação ao longo do Lineamento Patos, e o consequentemente enfraquecimento crustal promovido pelo seu desenvolvimento, milonitos quartzo-feldspáticos foram investigados por meio de microscopia óptica, microscópio eletrônico de varredura e principalmente por meio da técnica de difração de elétrons retroespalhados (EBSD). Os resultados obtidos indicam uma deformação extremamente heterogênea, caracterizada pela acomodação da deformação em zonas cada vez mais estreitas conforme a temperatura decresce durante o soerguimento das rochas afetadas pelo lineamento. Em condições de altas temperaturas (>700°C), após uma deformação predominantemente no estado magmático, camadas ricas em biotita tornam-se os domínios reológicos mais fracos, com a deformação sendo principalmente acomodada nestas camadas por meio da fluência de deslocações nos feldspatos, que registram a ativação do sistema (010)[100], e no quartzo, que registra a ativação dos sistemas Prisma-<a> e Prisma-[c]. Sob condições de temperaturas intermediárias (550-480°C), a deformação foi principalmente acomodada pela fluência de deslocações no quartzo e no plagioclásio, e de modo restrito no feldspato potássico. O quartzo apresenta microestruturas que indicam recristalização durante a transição de migração por borda de grão para rotação de subgrão. Os principais sistemas de deslizamento ativos foram (010)[100], (010)[001] e possivelmente (011)[100] no plagioclásio, (010)[100] no feldspato potássico, e prisma-<a> no quartzo. Recristalização do plagioclásio e mimerquitização do feldspato potássico seguido pela sua precipitação ao longo de sombras de pressão promoveram a redução do tamanho dos grãos e a formação de agregados poliminerálicos de granulação fina, que deformaram por meio de deslizamento de borda de grão assistido por fluência de deslocações ou por fluido, com a possível ativação dos

sistemas (011)[1-11], (010)[100], (10-1)[111] e (1-1-1)[110], deste modo promovendo mais enfraquecimento nas rochas deformadas. Sob condições de baixas temperaturas (<450°C), na faixa sul do lineamento, o feldspato registra deformação por meio de fraturamento e fluência por dissolução e precipitação. O quartzo mostra evidências de recristalização por *bulging* e fluência de deslocações, com a ativação dos sistemas prisma-<a> e romboédrico-<a> de modo subordinado. A expressão desta deformação nos milonitos de media a alta temperatura ao norte da borda sul ocorre na forma de delgadas zonas de cisalhamentos localizadas ao longo de descontinuidades estruturais como contato entre camadas e fraturas transgranulares. Além disso, foi sugerido que os sistemas (100)[010] no feldspato potássico e (021)[1-12] no plagioclásio reportados em trabalhos prévios podem ser fruto de interpretações errôneas.

Palavras-chave: EBSD. Quartzo. Feldspato. Mecanismos de deformação. Zona de cisalhamento Patos.

ABSTRACT

Microstructural and textural Studies of quartzo-feldspathic mylonites are essential to understand how the strain is localized and accommodated in the mid-crust. However, such studies in Brazilian shear zones are few. One of these structures is the Patos Lineament, a ~600 km long shear zone that deformed the paleoproterozoic basement of Borborema Province under different temperature conditions. In order to comprehend the solid-state processes responsible for strain localization and accommodation in the Patos shear zone, and the consequent crustal weakening promoted by its development, quartzo-feldspathic mylonites were investigated by means of optical microscopy, scanning electron microscopy and electron backscattering diffraction technique (EBSD). The results obtained from this study point out a heterogeneous deformation characterized by the accommodation of deformation in increasingly thinner high strain zones under decreasing temperatures during uplifting. At high-temperature deformation conditions (>700°C), after magmatic-state deformation, biotite-rich layers turn into the rheologically weaker domains which accommodated strain via dislocation creep, with the activation of (010)[100] in feldspar and prism-<a> and prism-[c] in quartz. Under medium-temperature conditions (550-480°C), deformation was mainly accommodated by dislocation creep in the quartz and plagioclase, and in a restricted way in the K-feldspar. The quartz display microstructures that indicate recrystallization during the transition from Grain boundary migration to subgrain rotation. The main active slip system were (010)[100], (010)[001] and possibly (011)[100] in the plagioclase, (010)[100] in the K-feldspar, and prism-<a> in the quartz. Recrystallization of plagioclase and myrmekitization of k-feldspar followed by the precipitation by solution in strain shadows promoted grain-size reduction and formation of the fine-grained polymineralic aggregates which deformed by dislocation-accommodated or fluid-assisted grain boundary sliding, with the activation of the easy slip systems (011)[1-11], (010)[100], (10-1)[111] and (1-1-1)[110], thus favouring further strain weakening of rocks. Under low-temperature conditions (<450°C), in the southern part of Patos shear zone, the feldspar record deformation by fracturing and dissolution-precipitation creep. The quartz show evidence of bulging recrystallization and dislocation creep, with the activation of prism-<a> and minor rhomb-<a> slip systems. The low-temperature deformation in the medium- to high-temperature mylonites

located at the northern block of the Patos shear zone is expressed by small-scale shear zones localized along structural discontinuities like layer contacts and transgranular fractures. Furthermore, was suggested that the slip systems (100)[010] in K-feldspar and (021)[1-12] in plagioclase reported in previous studies may be products of misinterpretation.

Key-words: EBSD. Quartz. Feldspar. Deformation mechanisms. Patos Shear Zone.

LISTA DE FIGURAS

LISTA DE TABELAS

LISTA DE FIGURAS DO MANUSCRITO

LISTA DE TABELAS DO MANUSCRITO

SUMÁRIO

1 INTRODUÇÃO

A deformação na crosta é extremamente heterogênea e tende a se localizar ao longo de estruturas denominadas de zonas de cisalhamento (Ramsay, 1980; Fossen e Cavalcante, 2017). A maneira na qual as rochas na litosfera respondem a deformação imposta nestas estruturas é controlada pela reologia de seus minerais constituintes, sendo que na parte intermediária da crosta este controle é principalmente exercido pela reologia do quartzo e do feldspato. O contraste reológico entre estes dois minerais durante a deformação depende do mecanismo pelo qual cada um a acomoda, que por sua vez, depende de fatores como taxa de deformação, tensão diferencial, temperatura, pressão, presença de fluidos e distribuição e tamanho inicial das fases (Handy, 1994; Burlini e Bruhn, 2005; Lopez-Sanchez e Llana-Fúnez, 2015). A caracterização de tais mecanismos, o entendimento de como eles acomodam a deformação durante a evolução das zonas de cisalhamento, e a determinação dos parâmetros condicionantes, tem levado geocientistas a se debruçar no estudo das microestruturas e texturas (ou orientações cristalográficas preferenciais - OCPs) de rochas monominerálicas ou poliminerálicas deformadas naturalmente e experimentalmente por meio de diversos instrumentos, tais como microscópio óptico, microscópio eletrônico de transmissão (MET) e de varredura (MEV) e estágio universal (e.g., Behrmann e Mainprice, 1987; Hirth and Tullis, 1992; Stünitz et al., 2003). Desde a década de 90, diversos trabalhos têm se utilizado da difração de elétrons retroespalhados para investigar as OCPs (Prior et al., 1999, Randle, 2010). Esta técnica permite a aquisição de uma alta quantidade bruta de dados de orientações cristalográficas de diferentes minerais de maneira rápida e relativamente simples, e vem se mostrando de grande importância no estudo de rochas deformadas.

No presente trabalho, utilizando a técnica de elétrons retroespalhados, foram investigadas as microestruturas e as texturas de milonitos quartzo-feldspáticos, formados sob diferentes condições de temperaturas durante o desenvolvimento da zona de cisalhamento Patos a fim de compreender os processos responsáveis pela localização e acomodação da deformação, e o consequente enfraquecimento crustal.

1.1 ESTRUTURA DA DISSERTAÇÃO

A dissertação está dividida em 7 capítulos. Os 4 primeiros são referentes a introdução da dissertação, com as justificativas, objetivos gerais e específicos, e localização da área de estudo (capitulo 1); Contexto geológico da área do estudo, sumarizando os estudos regionais prévios que trabalharam na região (Capítulo 2); fundamentação teórica na qual foi baseada a pesquisa (capitulo 3); e os materiais e métodos utilizados (capitulo 4). Os resultados (capitulo 5), estão apresentados na forma de um manuscrito em inglês intitulado "*Microstructures, slip systems and strain localization in quartzo-feldspathic mylonites from Patos shear zone revealed by EBSD data*", e incluem os principais resultados e discussões do trabalho. No capítulo 6 estão inclusas as considerações finais e as recomendações, onde são discutidas as principais conclusões e contribuições da pesquisa na área além das recomendações para trabalhos futuros. As Referências bibliográficas utilizadas na dissertação, fora o manuscrito, estão apresentadas no capitulo 7. Os dados referidos no manuscrito como "*supplementary material"* estão anexados no final da dissertação, nos apêndices.

1.2 JUSTIFICATIVA E OBJETIVOS GERAIS E ESPECÍFICOS

Estudos, envolvendo análises microestruturais e do desenvolvimento de OCPs, tem sido realizados por diversos pesquisadores internacionais em diversas zonas de cisalhamento desde 1960, com diversos avanços tem sido feito em relação a compreensão de como a deformação é localizada e acomodada nestas estruturas. Contudo, estudos desta natureza no âmbito nacional são escassos, e apenas recentemente avanços têm sido feitos em relação ao estudo das microestruturas e da textura de rochas deformadas por zonas de cisalhamento em território nacional. Neste contexto, o lineamento Patos, uma mega estrutura de escala continental que atravessa o nordeste brasileiro e possui conexão com lineamentos no continente africano, é uma zona de cisalhamento de grande relevância tectônica, e na qual pouco se conhece sobre os mecanismos na escala do grão que possibilitaram a localização e a acomodação da deformação no decorrer se seu desenvolvimento.

Deste modo, o presente trabalho tem como objetivo geral, investigar os processos responsáveis pela localização da deformação e os mecanismos pelo qual

o quartzo e o feldspato acomodaram a deformação, a partir do estudo das microestruturas e OCPs em milonitos quartzo-feldspáticos deformados sob diferentes condições de temperatura. Dentre outros objetivos mais específicos estão:

- Estimar de modo qualitativo as condições de deformação dos milonitos;
- Determinação dos sistemas de deslizamento ativos no feldspato e no quartzo;
- Comparar os mecanismos observados nos diferentes domínios;
- Caracterizar o particionamento da deformação durante a evolução microestrutural do Lineamento Patos.

1.3 LOCALIZAÇÃO DA ÁREA DE ESTUDO

FIGURA 1 - a) Áreas estudadas no contexto da Província Borborema. b) Pontos de estudo e de coleta de amostras no domínio Oeste do Lineamento Patos. c) Pontos de estudo e de coleta de amostras no domínio Central, próximo a cidade de Patos.

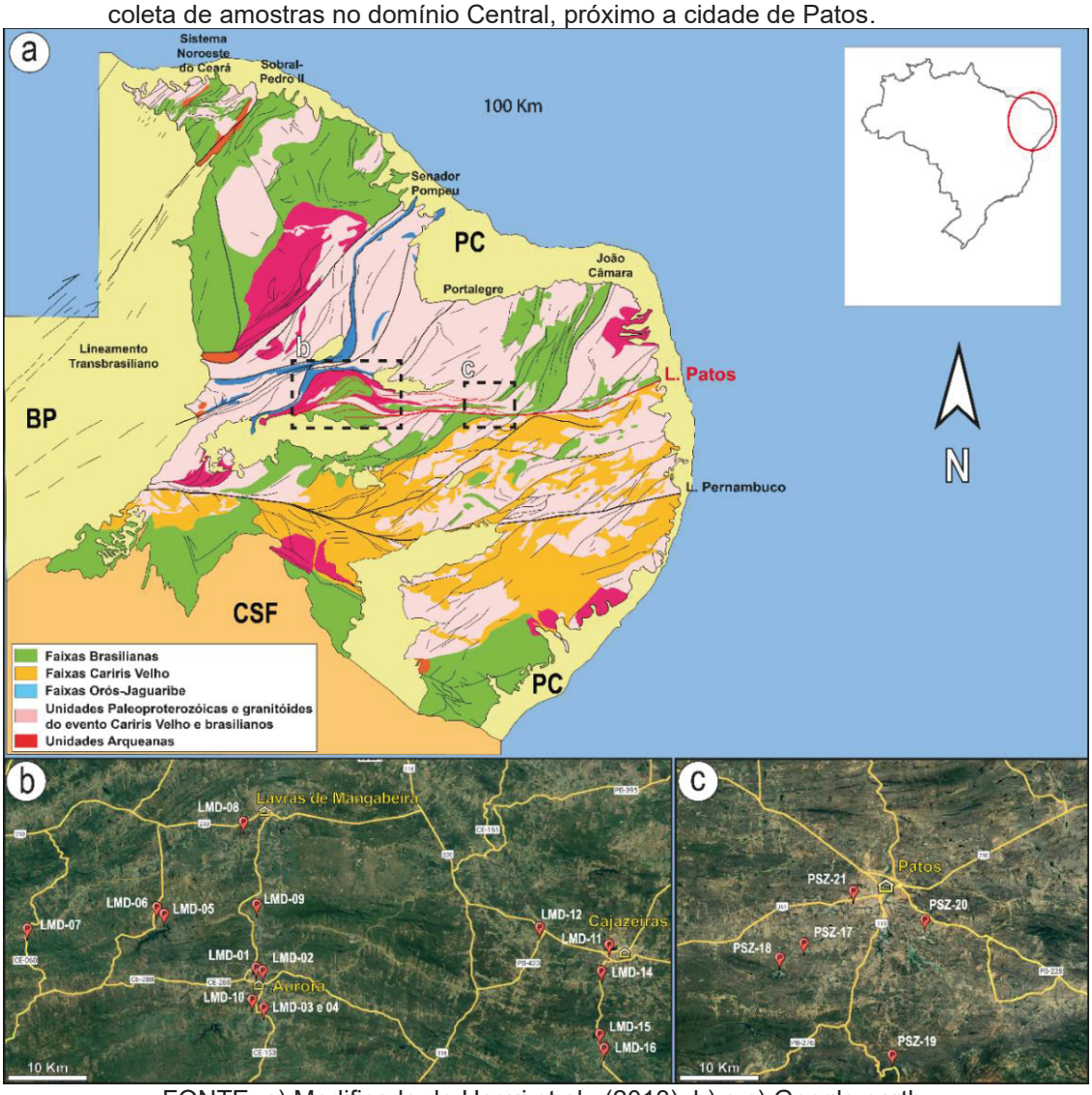

FONTE: a) Modificado de Hasui et al., (2013). b) e c) Google earth.

O Lineamento Patos é uma mega estrutura que abrange os estados do Piauí (PI), Ceará (CE), Rio Grande do Norte (RN) e Paraíba (PB) e é dividida em três domínios (Oeste, Central e Leste). O presente trabalho se concentrou na porção leste do domínio Oeste, que abrange as cidades de Cajazeiras (PB) e Aurora (CE) e no domínio Central, na região da cidade de Patos (PB)(FIGURA 1a). A fim de investigar os diversos aspectos da zona de cisalhamento Patos, a coleta de amostras ocorreu em dois perfis norte-sul, onde foram amostrados milonitos de alta a baixa temperatura. O mapa de pontos está indicado nas FIGURAS 1b e 1c.

2 CONTEXTO GEOLÓGICO

2.1 PROVÍNCIA BORBOREMA

A Província Borborema (Almeida et al., 1981) situa-se no nordeste do Brasil, sendo limitada ao sul pelo Cráton do São Francisco (CSF), a oeste pela Bacia do Parnaíba, e de norte a nordeste pela Província Costeira (FIGURA 1a)(Brito Neves et al., 2000). Esta faixa orogênica é resultante da aglutinação dos paleocontinentes São Francisco/Congo, Amazônico e Oeste-Africano/São Luís durante a amalgamação do Gondwana ocidental no Neoproterozóico. A província é constituída, de modo geral, por um embasamento arqueano-paleoproterozóico gnáissico/migmatítico, faixas xistosas neoproterozóicas semicontínuas, além de inúmeras intrusões Brasilianas (Neves, 2003). Estas unidades compõem domínios e terrenos tectônicos limitados por uma rede de zonas de cisalhamento regionais denominada de Sistema de Cisalhamento Borborema (SCB), que também é correlacionada com estruturas similares no continente africano (Vauchez et al., 1995) (FIGURA 2).

A SCB é dividida nos domínios oeste e domínio leste. O domínio oeste, situado majoritariamente no estado do Ceará, compreende zonas de cisalhamento retilíneas de tendência NE-SW, predominante dextrais, e incluem as zonas de cisalhamento Granja, Sobral, Senador-Pompeu, Tatajuba e Potengi. O domínio leste apresenta um arranjo mais complexo, sendo caracterizado por dois lineamentos continentais de tendência EW (Zona de Cisalhamento Patos e Pernambuco) que convergem para faixas transpressionais (Faixas Seridó e Cachoeirinha) e zonas de

cisalhamento subsidiárias de tendência NE, com evidências de movimento inicialmente dextral e sinistral tardiamente (Vauchez et al., 1995). As zonas de cisalhamento que compõe o SCB compartilham de diversas características em comum tais como: deformação cisalhante concomitante a um magmatismo sincinemático; intrusões de diques paralelos a foliação milonítica; presença de migmatitos e faixas miloníticas de alta e baixa temperatura coexistentes (Vauchez et al., 1995; De witt et al., 2003; Van schmus et al., 2008).

FIGURA 2 - Sistema de Cisalhamento Borborema

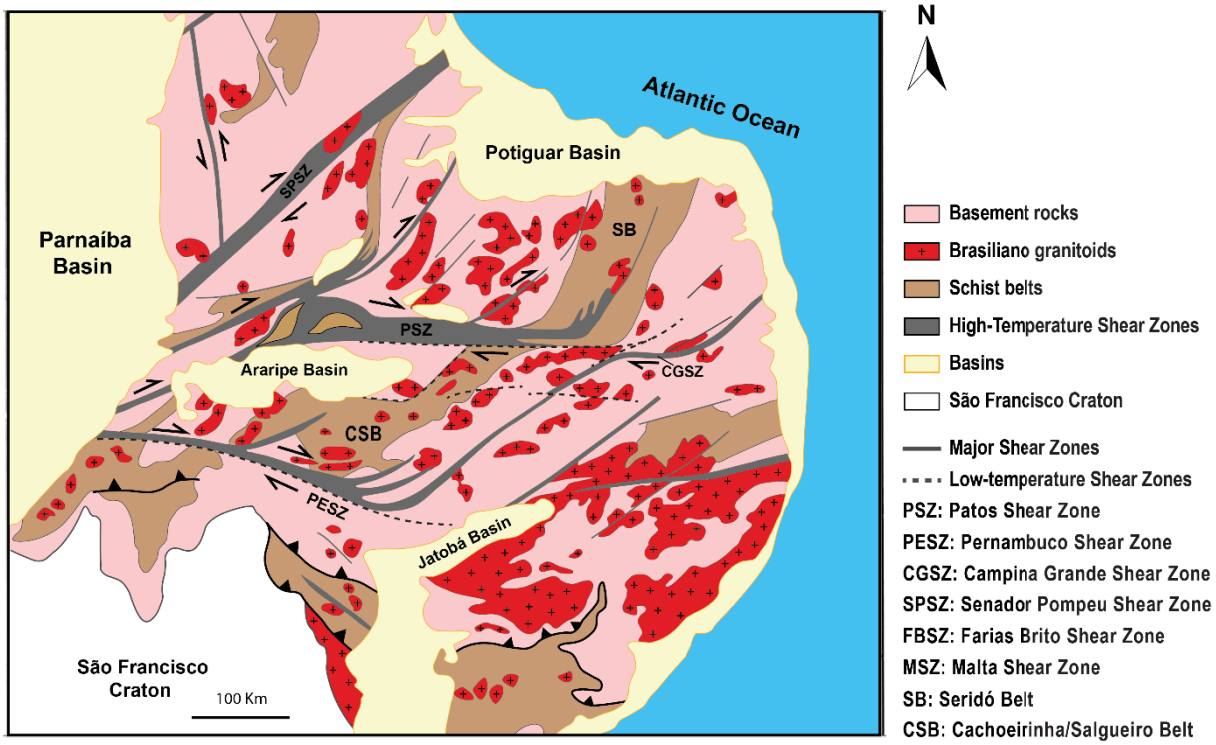

FONTE: Modificado de Neves et al. (2000)

2.2 ZONA DE CISALHAMENTO PATOS

A Zona de Cisalhamento Patos (ZCPa) (FIGURA 3) é uma falha de rejeito direcional de cinemática dextral de aproximadamente 600 km de extensão e com até 30 km de largura em seu segmento central (Viegas et al., 2013). Ela separa o bloco norte, constituído de rochas arqueanas a paleoproterozóicas que formam o embasamento da Faixa Seridó (FS), do bloco sul, que compreende rochas meso- a neoproterozóicas da Zona Transversal (Brito Neves et al., 1995). No contato com o bloco sul, a ZCPa é separada do terreno Cachoeirinha-Salgueiro por uma faixa de milonítica em fácies xisto verde de 1-2 km de espessura (Corsini et al., 1991;

Vauchez et al., 1995). As principais unidades afetadas pela ZCPa consistem no embasamento gnáissico-migmatítico paleoproterozóico (Complexo Caicó e Granjeiro), faixas metassedimentares neoproterozóicas representada pelo grupos Seridó e pela Formação Lavras de Mangabeira, além de diversos corpos plutônicos anatéticos sin-cinemáticos.

A ZCPa é compartimentada por alguns autores em três domínios estruturais chamados de Domínio Leste, Central e Oeste (Viegas et al., 2014; Cavalcante et al., 2016). No Domínio Leste, localizado a leste da FS, a ZCPa sofre uma diminuição na espessura, as estruturas são rotacionadas de E-W para NE-SW e o seu braço sul se conecta com a zona de cisalhamento Campina Grande em uma configuração tipo en-échelon (Vauchez et al., 1995). O domínio central compreende ortognaisses miloníticos e milonitos de alta temperatura de direção EW que migram para anatexitos na conexão com a FS. Nesta conexão as estruturas mudam progressivamente sua orientação para NE, indicando uma continuidade mecânica entre a ZCPa e a FS (Corsini et al., 1991). O domínio oeste é caracterizado por uma estrutura em duplex, denominado Duplex Lavras de Mangabeira (DLM), que se conecta com as zonas de cisalhamento Tatajuba e Potengi, pertencentes ao domínio oeste do SCB (Vauchez et al., 1995; Corsini et al., 1996).

FIGURA 3 - Mapa simplificado das principais unidades afetadas pela zona de cisalhamento Patos. Os afloramentos visitados indicados pelas estrelas vermelhas.

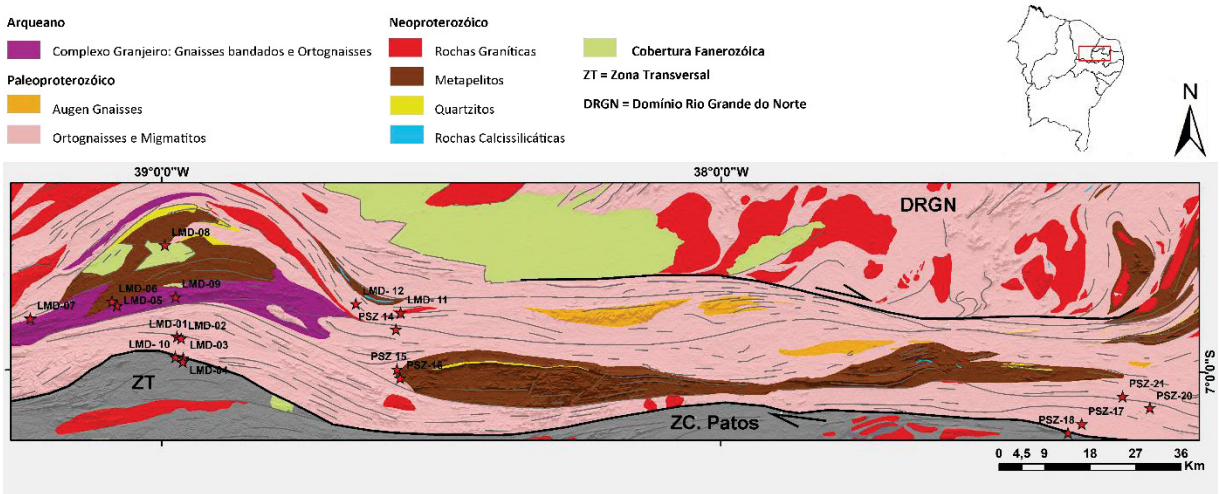

FONTE: Compilado a partir dos trabalhos de Angelim et al. (2004), Medeiros et al. (2005), Costa et al. (2018), Palheta et al. (2019)

2.3 DUPLEX LAVRAS DA MANGABEIRA

Situado no domínio oeste da ZCPa, e um dois principais alvos deste trabalho, o DLM (FIGURA3) consiste em uma estrutura duplex que acomoda a mudança na direção de rejeito que ocorre na transição da PSZ para as zonas de cisalhamento Potengi e Tatajuba (Vauchez et al., 1995). A norte, o duplex ramifica nas zonas de cisalhamento Porto Alegre e Jaguaribe de direção NE. Esta estrutura, com espessura máxima de 50 Km e aproximadamente 150 Km de extensão, é caracterizada por um arranjo arqueado de zonas de cisalhamento anastomosadas de espessura quilométricas que envolve lentes de material não milonitizado (Corsini et al., 1996). A leste, próximo a cidade de Cajazeiras, todas as zonas de cisalhamento convergem juntas para formar o segmento central da ZCPa. Diversos indicadores cinemáticos indicam uma cinemática dextral, e a geometria e as estruturas geológicas presentes sugerem um regime deformacional transpressivo, caracterizando uma estrutura em flor positiva assimétrica (Corsini et al., 1996). O mergulho da foliação dentro do DLM diminui progressivamente de sul para norte e cavalgamentos subsidiários sobrepõe unidades do embasamento sobre sequências metassedimentares mais jovens (Corsini et al., 1996). É possível que essa configuração tenha sido favorecida por uma trama de baixo ângulo pré-existente a zona de cisalhamento.

O núcleo do DLM ou Bloco Assaré (Caby et al., 1995) compreende o embasamento arqueano-paleoproterozóico representado pelos Complexos Granjeiro e Caicó e pelas rochas metassedimentares da Formação Lavras da Mangabeira de idade Neoproterozóica.

O Complexo Caicó, principal unidade estudada neste trabalho, representa o embasamento do Grupo Seridó e de suas formações metassedimentares correlatas (Souza et al., 2007). Na região, ela ocorre nas bordas do DLM, envolvendo o Complexo Granjeiro. O complexo é composto de granitóides e ortognaisses migmatíticos de composição tonalítica a granodiorítica, com rochas metassedimentares e anfibolitos subordinados (Caby et al., 1995). Idades U-Pb apontam um período de formação entre 2.1 e 2.24 Ga (Hackspacher et al., 1990; Legrand et al., 1991; Dantas, 1996). A assinatura geoquímica destas rochas sugere duas interpretações genéticas. A primeira onde os ortognaisses consistem de uma suíte arqueana tipo TTG formada por vários pulsos de magmatismo e processos

associados de *mixing* e *migling* de magma (Dantas, 1992; Petta, 1995). O segundo sugere que magmas parentais foram derivados a partir da fusão parcial de um mando enriquecido (Souza et al., 1993).

2.4 CONDIÇÕES DE DEFORMAÇÃO NA ZCPA

A ZCPa apresenta um complexo padrão de estilos e regimes deformacionais. No Domínio central, próximo a cidade de Patos (PB), a assembleia metamórfica em metapelitos e leucossomas sin-cinemáticos sugerem temperaturas acima de 700°C e pressões que variam de 3 a 4 Kbar (Caby et al., 1995; Vauchez et al., 1995; Corsini et al., 1996; Corsini et al., 1998). Próximo a Cajazeiras (PB), temperaturas em torno de 700 °C e pressões de 5 a 6 Kbar foram obtidas em metepelitos (Corsini et al., 1996). No núcleo do bloco Assaré, assembleias metamórficas em metapelitos apontam temperaturas em torno de 600°C e pressões em torno de 3 a 3,5 Kbar (Caby et al., 1995; Monié et al., 1997). Além disso, a presença de veios e pacotes de leucossomas cisalhados, o paralelismo da foliação magmática dos migmatitos com foliação de estado-sólido nos ortognaisses miloníticos encaixantes, além da transição de microestruturas de estado-sólido para magmáticas nos milonitos de oeste para leste indicam que a deformação cisalhante de alto grau foi concomitante a fusão parcial. As estimativas de temperaturas supracitadas juntamente com microestruturas sugerem que a deformação na ZCPa ocorreu em fácies anfibolito e em baixas pressões, acompanhado por fusão crustal (Corsini et al., 1991). Análises $^{40}Ar/^{39}Ar$ em cristais de hornblenda e biotita nos domínios central e oeste, indicam uma taxa de resfriamento mais lenta no primeiro em relação ao segundo. Tais características indicam um gradiente termal na ZCPA, com uma diminuição da temperatura de leste a oeste e diferentes histórias de resfriamento, possivelmente devido ao maior volume de material fundido presente no domínio central da ZCPa (Monié et al., 1997; Corsini et al., 1998).

3 FUNDAMENTAÇÃO TEÓRICA

3.1 DEFORMAÇÃO CRISTAL-PLÁSTICA (OU INTRACRISTALINA)

Sob elevadas temperaturas, minerais podem se deformar permanentemente sem que haja rompimento de sua estrutura cristalográfica devido à presença e mobilidade de defeitos cristalinos. Isto é chamado de deformação intracristalina ou deformação cristal-plástica. Os defeitos podem ser divididos em defeitos pontuais, defeitos lineares e defeitos planares. Os defeitos pontuais podem ser classificados em “vacâncias” ou “impurezas” (FIGURA 4a), caracterizados respectivamente pela ausência de átomos e pela presença átomos extras no retículo cristalino do cristal. Este último ainda pode ser do tipo intersticial, caracterizados pela ocupação de um espaço vazio no retículo cristalino, ou substitucional, em que ocorre a substituição de um átomo do retículo por um outro diferente (FIGURA 4b).

FIGURA 4 - Defeitos cristalinos mais comuns. a) Vacâncias (v) e impurezas (i); b) Impurezas, podendo ser do tipo substitucionais (II) ou intersticiais (I).

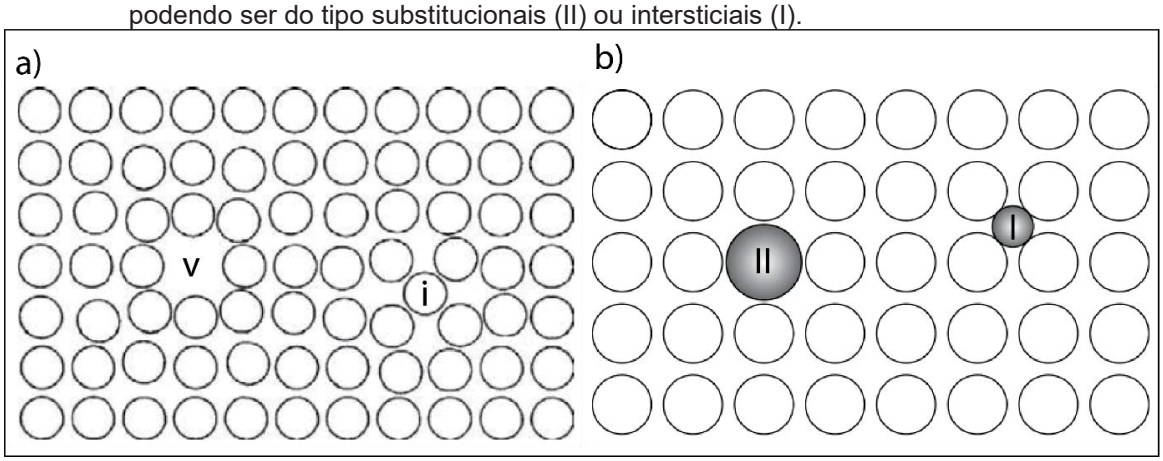

FONTE: a) Modificado de Hull e Bacon (2011)

Os defeitos lineares, ou deslocações, são definidos pela presença de um plano cristalográfico extra no retículo cristalino que delimita uma região que se deslocou em relação a outra. Elas geralmente nucleiam a partir de pequenas regiões chamadas fontes de Frank-Read (*Frank-Read sources*) e se espalham no retículo na forma de loops expansivos (Hobbs et al., 1976; Tullis, 2002). Uma deslocação pode ser descrita por meio de um vetor **i** paralelo a linha de deslocação e pelo vetor ***burger*** que indica a direção do deslocamento. Quando os vetores são perpendiculares definem um *edge dislocation* (FIGURA 5a), e quando paralelos, um *screw dislocation* (FIGURA 5b), ambos membros finais de uma série de combinações chamadas de deslocações mistas (Hull e Bacon, 2011).

O movimento de deslocações é um processo denominado de deslizamento de deslocações (*dislocation glide*), e ocorre pela ativação de um ou mais sistemas

de deslizamento (*slip system*) assim que a sua energia de ativação de moção é atingida (van der Pluijm e Marshak, 2004). Um sistema de deslizamento é caracterizado por um plano de deslizamento (*slip plane*) e uma direção de deslizamento (*slip direction*), sendo representados pelas notações (*hkl*)[*uvw*] ou {*hkl*}<*uvw*> (quando se refere a um conjunto de planos e direções simetricamente equivalentes, Miranda et al., 2016) que descrevem respectivamente os índices de Miller do plano e da direção do sistema. Para que um sistema seja ativado é necessário que a tensão cisalhante critica resolvida (*Critical resolved shear stress* ou CRSS) do sistema seja excedida, cujo valor varia para cada sistema de deslizamento, e depende da temperatura, tensão diferencial, atividade química e da taxa de deformação (Passchier e Trouw, 2005). A fonte da força motriz do deslizamento pode ser a distorção do retículo ao redor de uma deslocação ou devido a aplicação de uma tensão diferencial (van der Pluijm e Marshak, 2004). Via de regra, os planos cristalográficos mais compactados e as direções cristalográficas com os vetores reticulares mais curtos e com ligações mais fracas do cristal tendem a definir os sistemas de deslizamento (Tullis, 2002; Twiss e Moores, 2007).

FIGURA 5 - Ilustração simplificada de uma deslocação do tipo “*edge*” e do tipo “*screw*”.

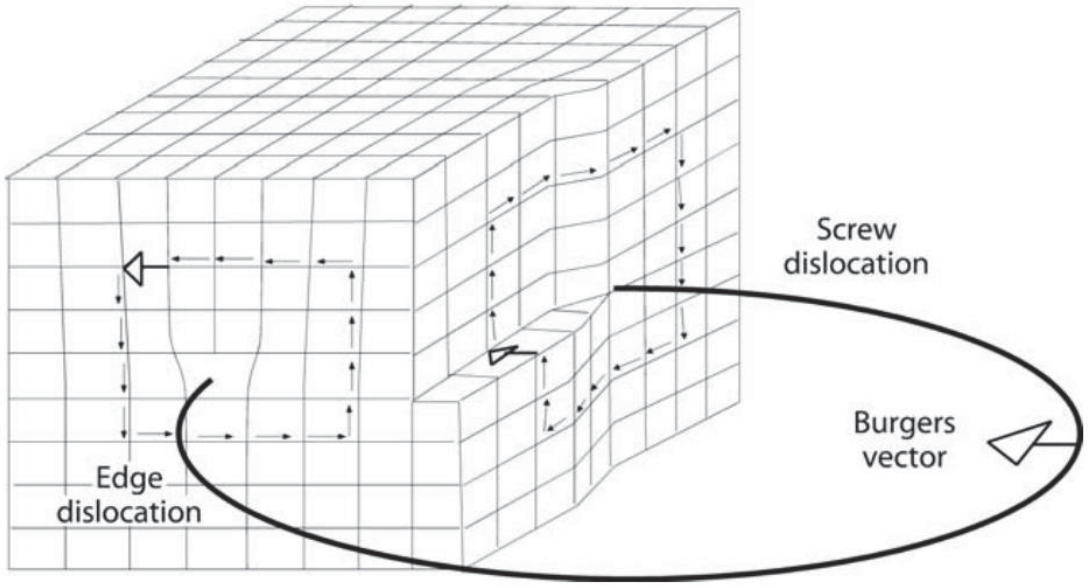

FONTE: Adaptado de Passchier e Trouw (2005)

Quando as temperaturas não são o suficientemente altas a movimentação de deslocações pode ser bloqueada ou dificultada pela presença de impurezas normalmente presentes no retículo cristalino do material, podendo levar a um

aumento na densidade de deslocações e a criação de locais de acumulação de deslocações chamados de emaranhados de deslocações (*dislocation tangle*), que por sua vez, resulta em endurecimento por deformação (*strain hardening*) (Tullis e Yund, 1987; Van der Pluijm e Marshak, 2004; Passchier e Trouw, 2005). Se a temperatura for elevada o suficiente, o material tende a diminuir a densidade de deslocações por meio de vários processos que facilitam o movimento das *edge escrew dislocations*, tais como escalada de deslocações (*dislocation climb*) em relação a primeira e deslizamentos cruzados (*cross-slip*) em relação a segunda. A atuação conjunta destes processos com o deslizamento de deslocações caracteriza a fluência de deslocações (*dislocation creep*) (Tullis, 1983; Passchier e Trouw, 2005).

O aumento na densidade de deslocações em um cristal por meio do acúmulo de defeitos e de emaranhados de deslocações devido a resposta a uma tensão diferencial aplicada, leva a um aumento na energia deformacional interna (Passchier e Trouw, 2005). A fim de reduzir esta energia diversos processos atuam para diminuir a densidade de deslocações sem envolver a formação de novos grãos, um processo chamado de recuperação (Hobbs et al., 1976; White, 1977). Além dos processos citados anteriormente (*climb* e *cross-slip*), mecanismos de aniquilação e a formação de subgrãos (FIGURA 6) são meios que atuam para rearranjar e eliminar deslocações (Hobbs et al., 1976; Trimby et al., 1998; Tullis, 2002). O processo de recuperação é evidenciado pela presença de bandas de deformação (*deformation bands*) e subgrãos (Vernon, 2004; Passchier e Trouw, 2005).

FIGURA 6 - Formação de um subgrão por meio do processo de recuperação.

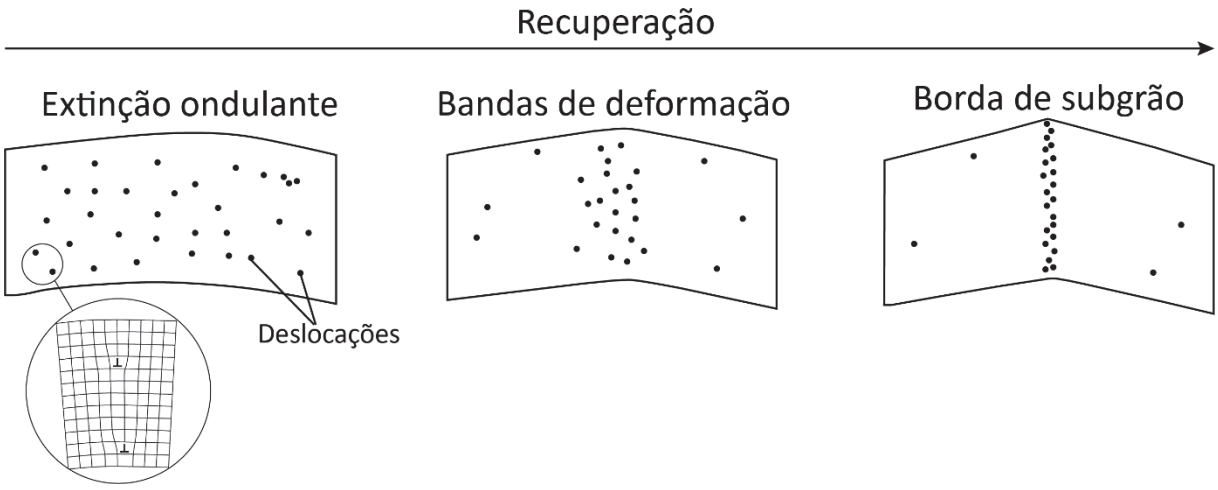

FONTE: Adaptado de Passchier e Trouw (2005)

A recristalização de um agregado policristalino que ocorre na ausência de uma deformação é denominada de recristalização estática (Urai et al., 1986). Este tipo de recristalização envolve vários processos que buscam a eliminação de deslocações, bordas de subgrãos e formas irregulares dos cristais, a fim de chegar a um estado de energia livre interna mínimo. Tais processos incluem aqueles presentes na recuperação e a redução da área de borda de grãos (*grain boundary area reduction*, Passchier e Trouw, 2005). Dentre as principais evidências deste processo estão o crescimento de cristais opticamente livres de deformação interna, poligonais, com bordas retilíneas ou levemente curvadas e de granulação grossa (Vernon, 2004; Passchier e Trouw, 2005).

3.2 RECRISTALIZAÇÃO DINÂMICA

FIGURA 7 - Características comuns das tramas resultantes dos mecanismos de recristalização. a) BLG; b) SGR e c) GBM.

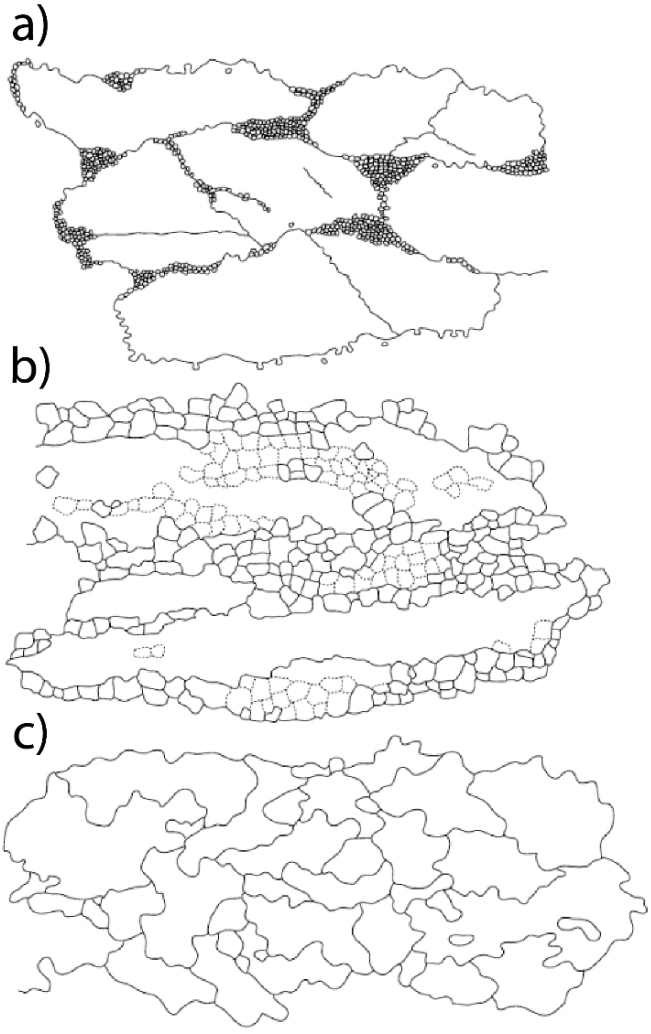

FONTE: Adaptado de Stipp et al. (2002)

A recristalização dinâmica pode ser definida como o retrabalhamento do tamanho, forma ou orientação dos cristais induzido por deformação, com pouca ou nenhuma mudança química (Poirier e Guillopé, 1979). Esta recristalização é governada por dois processos principais, denominados de migração de borda de grão e rotação de subgrão. Estes processos não operam de modo independente, mas interagem de modo a definir, de acordo com Stipp et al., (2002), três principais tipos de mecanismos de recristalização chamados de: i) recristalização por *bulging* (*Bulging recrystallization* - BLG); ii) recristalização por rotação de subgrão (*subgrain rotation recrystallization* - SGR*)* e iii) recristalização por migração de borda de grão (*grain boundary migration recrystallization* - GBM) e correspondem respectivamente aos regimes 1, 2 e 3 de fluências de deslocações de Hirth e Tullis (1992). A transição sucessiva do regime 1 ao 3 ocorre com o aumento da temperatura e/ou diminuição da taxa de deformação (além da presença de fluidos) e resulta em tamanhos de grãos progressivamente maiores.

A recristalização por *bulging* (FIGURA 7a) é caracterizada por uma mobilidade de borda de grão localizada, na qual a borda de um cristal migra em direção a outro com maior densidade de deslocação, formando um diminuto novo cristal, geralmente livre de deformação (Urai et al., 1986, Stipp et al. 2002). Os novos grãos recristalizados tendem a nuclear em junções tríplices, bordas de grãos normais a foliação e fraturas. Os grãos reliquiares tendem a apresentar bordas irregulares e lobadas com lobos do tamanho dos novos grãos (Passchier e Trouw, 2005), além de apresentarem extinção ondulante, lamelas de deformações e até fraturamento rúptil. A SGR é caracterizada pela continua adição de deslocações a bordas de subgrãos de modo que a desorientação entre o subgrão e o cristal hospedeiro é aumentada até que defina um novo grão recristalizado, ou seja, por uma rotação do subgrão (Passchier e Trouw, 2005). As principais evidências deste mecanismo são a presença de grãos recristalizados livres de deformação interna e de tamanho uniforme e similar aos subgrãos, os grãos relictos em geral são achatados, formam cordões (*ribbons*), apresentam microestruturas típicas de deformação intracristalina e contém bordas na qual há uma transição gradual dos subgrãos para os novos grãos recristalizados (FIGURA 7b, Stipp et al., 2002; Passchier e Trouw, 2005). A GBM é caracterizada pela rápida e extensiva migração de borda de grão na qual pode chegar a consumir grãos inteiros, removendo deslocações e subgrãos. A rotação de subgrão pode ainda estar ativa durante o

processo, mas as bordas de subgrão se tornam altamente móveis assim que se tornam novos grãos (Passchier e Trouw, 2005). Os grãos recristalizados são grandes e tendem a apresentar formas ameboides com bordas bastante lobadas e com interdigitações (FIGURA 7c). Este mecanismo produz algumas microestruturas típicas como as microestruturas do tipo p*inning*, *window*, *dragging*, *left-over grains* e *castellate* que podem ser utilizadas para indicar a direção de migração (Jessel, 1987). Stipp et al. (2002) ainda sugeriu a subdivisão deste mecanismo em dois tipos, recristalização por migração de borda de grão do tipo I (controlados por impurezas) e do tipo II (não controlado por impurezas), dependendo do controle do *pinning* na mobilidade das bordas.

3.3 MECANISMOS SENSÍVEIS AO TAMANHO DO GRÃO

Alguns mecanismos de deformação são ativados quase que exclusivamente em agregados de granulação muito fina. Tais mecanismos são denominados coletivamente de mecanismos sensíveis ao tamanho do grão (Rutter e Brodie, 1988; Fukuda et al., 2012), e exercem grande influência na reologia do material e na localização da deformação (Menegon et al., 2013; Platt, 2015).

FIGURA 8 - Tipos de fluência difusiva que ocorrem através do retículo cristalino (Nabarro-Herring) ou ao longo das bordas dos cristais (Coble).

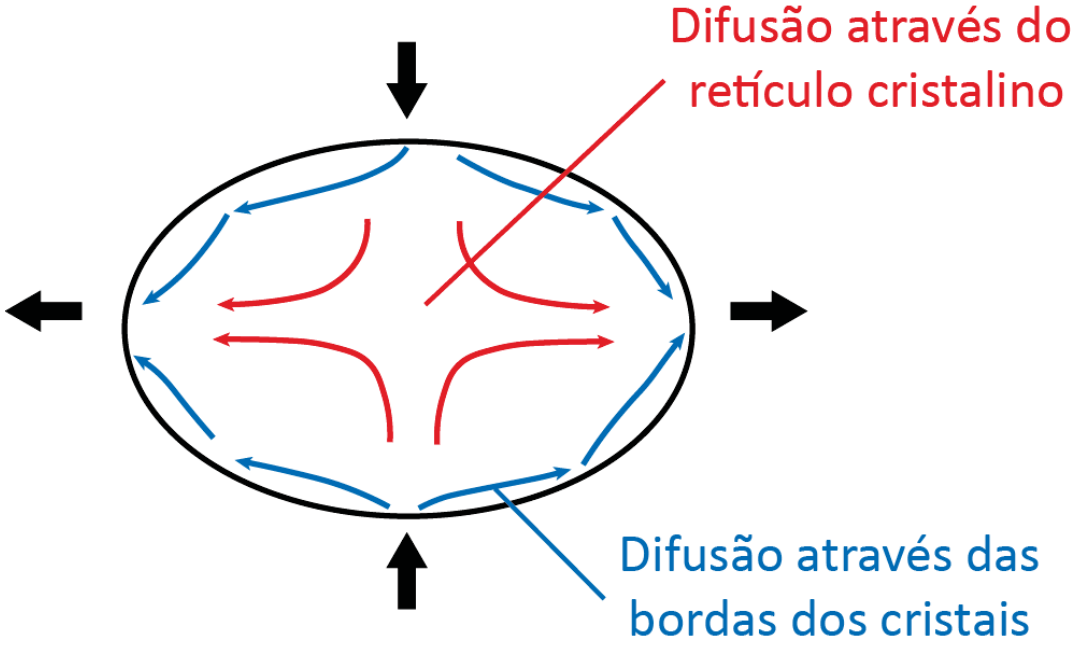

FONTE: Modificado de McClay (1977).

Sob altas temperaturas e baixas tensões diferenciais, os cristais podem se deformar por meio da migração de vacâncias e de átomos através do retículo cristalino entre áreas onde as tensões aplicadas são máximas e mínimas, em um processo denominado de transferência de massa difusiva na escala do grão (Grain-scale diffusive mass transfer; Passchier e Trouw, 2005; Venon, 2004). Este processo é divido em dois tipos: Fluência de Coble e fluência de Nabarro-Herring (FIGURA 8). Sendo o primeiro caracterizado pela difusão ao longo das bordas do material e o segundo por meio da difusão através do retículo cristalino. A fluência de Coble tende a ser mais rápida e é mais efetiva em menores temperaturas do que a fluência de Nabarro-Herring, pois apresenta uma energia de ativação mais baixa (Poirier, 1985; Twiss e Moores, 2007).

FIGURA 9 - Ilustração simplificada do mecanismo de fluxo granular, evidenciando a atuação do deslizamento de borda de grão no cristal do arcabouço (rosa), com os vazios criados sendo preenchidos por material transportado por solução ou difusão (amarelo).

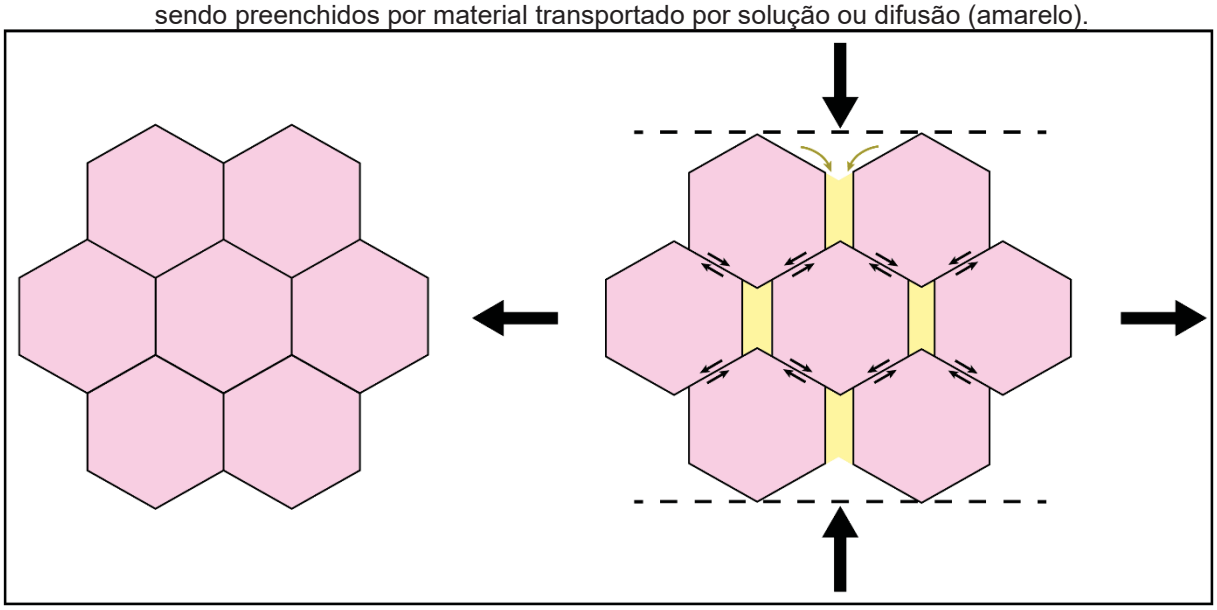

FONTE: Modificado de Poirier (1985).

Em agregados muito finos, um grão pode deslizar em relação ao outro sem que haja perda de coesão em um processo chamado de deslizamento de borda de grão (*Grain boundary sliding*, Ashby e Verrall, 1973). Este mecanismo normalmente produz incompatibilidades que são acomodadas ou limitados por outros mecanismos tais como fluência de deslocações (Dislocation-accommodated GBS – DisGBS) ou formação de lacunas, que são preenchidas por material advindo via transferência difusiva de massa ou por dissolução e precipitação (FIGURA 9, Etheridge e Wilkie, 1978), um mecanismo chamado por alguns autores de fluxo granular (Tullis, 2002;

Oliot et al., 2014). Diversos trabalhos apontam como indícios da atuação da fluência difusiva e deslizamento de borda de grãos a falta de orientações cristalográficas preferenciais e de forma (*shape preferred orientation*-SPO), e a mistura de fases em agregados com grãos equidimensionais muito finos (e.g., Kilian et al., 2011; Oliot et al., 2014; Mehl e Hirth, 2008). Outros autores ainda sugerem o termo superplasticidade, que caracteriza um material com grãos uniformes muito finos, e que sob altas temperaturas e por intermédio do fluxo granular, pode sofrer intensa deformação sem sofrer salsichamento (*boudinage*, Passchier e Trouw, 2005).

3.4 ORIENTAÇÕES CRISTALOGRÁFICAS PREFERENCIAIS

A deformação plástica de volume rochoso pode acarretar no desenvolvimento de uma textura cristalográfica, isto é, uma orientação cristalográfica preferencial (OCP), definida pelo arranjo sistemático de planos e eixos cristalográficos dos cristais. O padrão de uma OCP de uma rocha deformada é resultado de um conjunto de fatores, dentre eles o tipo de mecanismo de deformação, história deformacional (trajetória, magnitude e geometria do elipsoide da deformação finita) e dos sistemas de deslizamento ativos (FIGURA 10a, Schmid e Casey, 1986; Law, 1990; Barth et al., 2010). Portanto, a análise acurada dos OCPs de uma rocha deformada pode revelar informações sobre a geometria da deformação aplicada, mecanismos de deformação e a temperatura de deformação na qual a rocha esteve submetida durante a deformação (e.g., Kruhl, 1996; Bons e Brok, 2000; Menegon et al., 2008).

Embora uma OCP possa ser obtida por outros mecanismos de deformação, como por exemplo fluência por dissolução e precipitação (e.g., Bons e den Brok, 2000; Menegon et al., 2008), a fluência de deslocações é tido como o principal mecanismo responsável pelo desenvolvimento de OCPs em rochas deformadas plasticamente (Bons e Brok, 2000). De acordo com Hobbs et al., (1976) o desenvolvimento de uma OCP mediante fluência de deslocações pode ser resultante de dois processos: i) via rotação de corpo rígido e atividade de sistemas de deslizamento particulares nos grãos; ii) por meio de mecanismos de recristalização. No primeiro caso, quando um cristal se deforma por meio de um único sistema de deslizamento, o plano e a direção de deslizamento deste sistema tendem a rotacionar de modo a se paralelizar com o eixo de estiramento máximo (λ_1) de modo a acomodar a incompatibilidade gerada entre a vorticidade interna e a externa (Lister

et al., 1978). Deste modo, um sistema de deslizamento pode ser indiretamente inferido observando a distribuição dos planos e direções em relação a um referencial do elipsoide de deformação. No caso de rochas os referenciais geralmente são foliações e lineações minerais ou de estiramento (e.g., Schmid e Casey, 1986; Heidelbach et al., 2000; Keller and Stipp, 2011). Contudo, a fim de manter uma certa compatibilidade durante deformação, os cristais de um agregado deformando-se desta maneira devem ter pelo menos cinco sistemas de deslizamentos independentes ativos (teoria de Taylor-Bishop-Hill), ou devem rotacionar de modo que minimizem o desajuste (*misfit*) geométrico em um agregado que deforma com um limitado número de sistema de deslizamentos (modelo de minimização de desajuste, Twiss e Moores, 2007). Diversas simulações utilizando tais modelos teóricos tem reproduzidos padrões de orientações cristalográficas bastante similares aos observados naturalmente (e.g., Lister e Dornsiepen, 1981; Stipp et al., 2002) e experimentalmente (Wagner et al., 1982; Dell'Angelo e Tullis, 1989). A recristalização dinâmica atua normalmente consumindo cristais não favoráveis ao deslizamento, embora o inverso também possa ocorrer (Schmid e Casey, 1986).

FIGURA 10 - a) Padrão de OCP de acordo com o tipo de deformação. b) Tipos de guirlandas cruzadas.

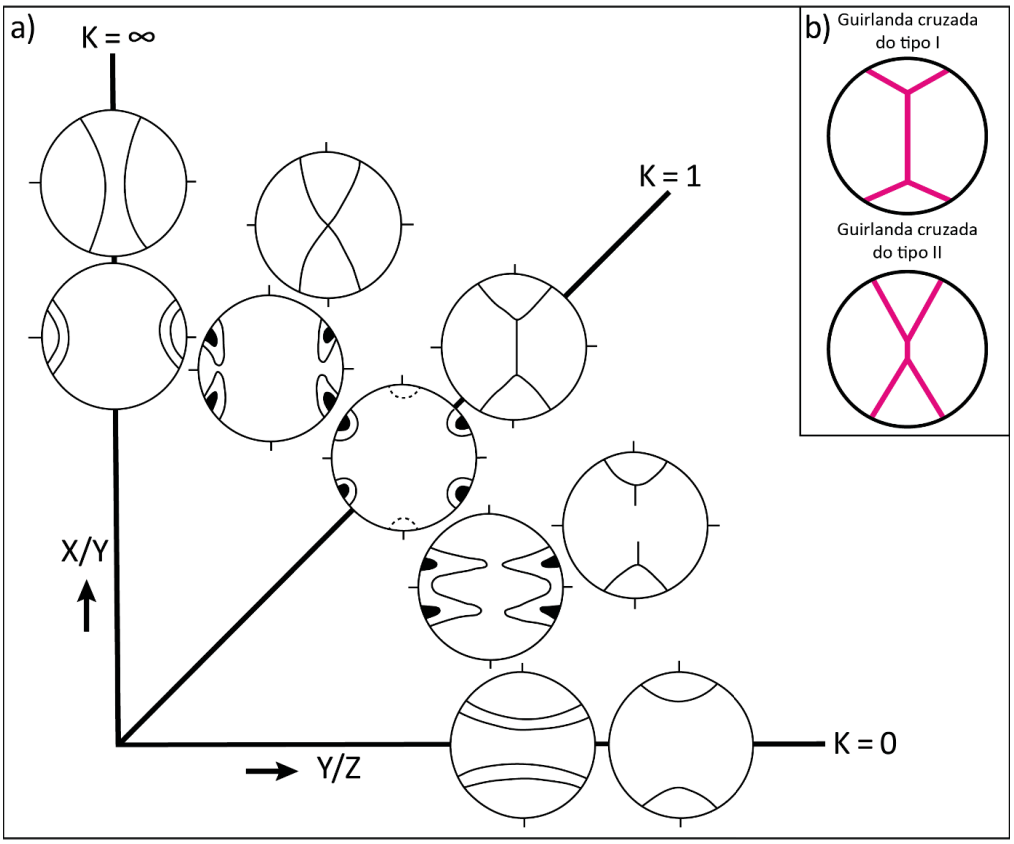

FONTE: a) Modificado de Urai et al. (1986).

Há diversas maneiras de representar graficamente orientações cristalográficas (ver capitulo 4.3), a mais comumente utilizada é por meio de figuras de polo (FIGURA 10). Nas figuras os padrões geralmente ocorrem na forma de elementos geométricos como pontos máximos, guirlandas circulares pequenas ou grandes, ou guirlandas singulares (*single girdles*) e cruzadas (*crossed girdles*) (FIGURA 10b). Os padrões são interpretados de acordo com sua assimetria interna (forma do padrão) e externa (com relação a um referencial externo) (Law, 1990).

FIGURA 11 - Padrões de OCP do quartzo de acordo com os sistemas de deslizamento ativos e a temperatura. a) Planos e direções de deslizamento principais do quartzo. b) Posição dos planos nas figuras de polo de acordo com o sistema de deslizamento ativo. C) Mudança no padrão de OCP de acordo com a temperatura e com o acúmulo de *strain*.

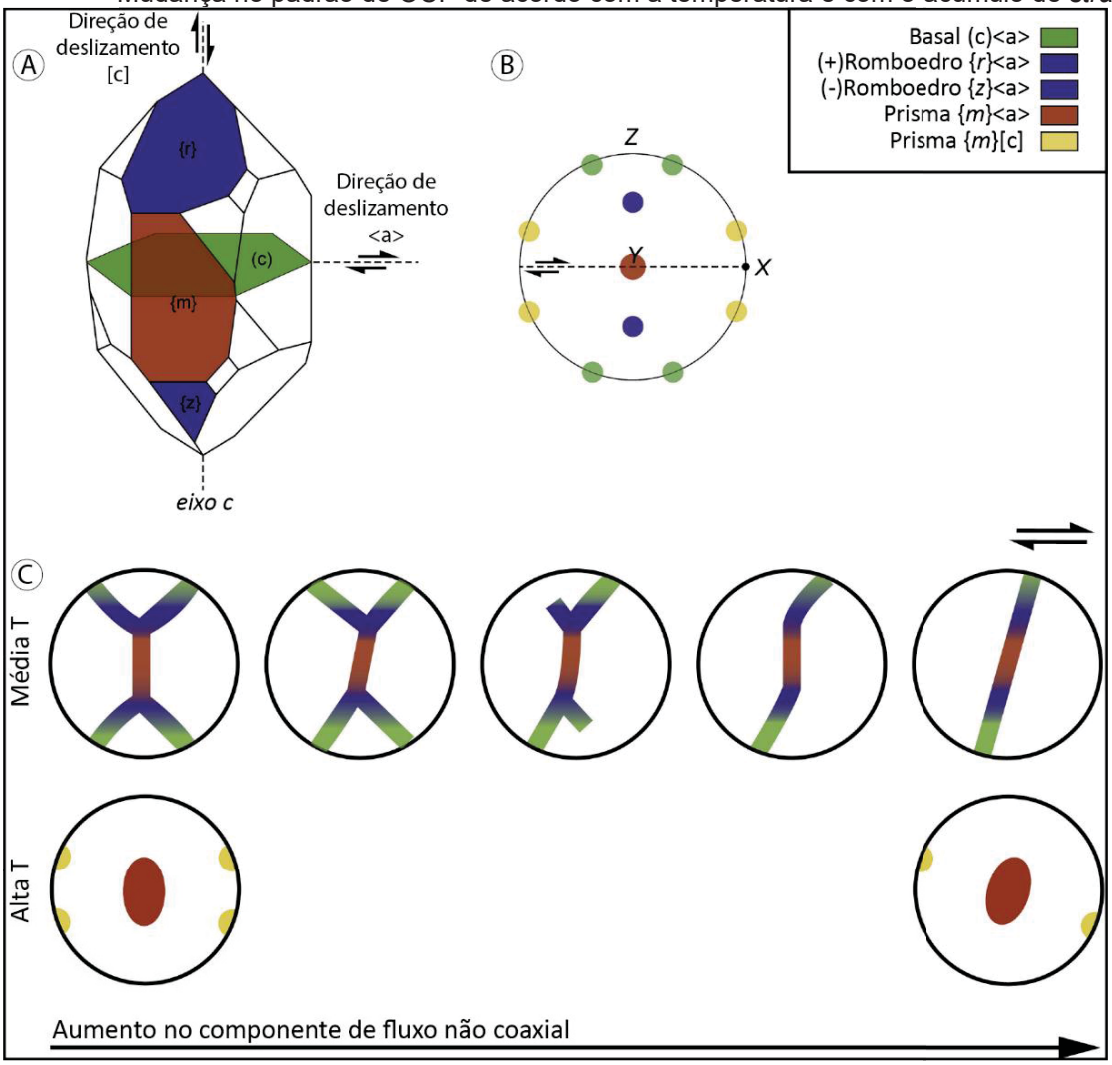

FONTE: Modificado de Hunter et al. (2018).

Como um sistema de deslizamento é termicamente ativado, a ativação de um ou mais sistemas também irá depender da temperatura (Law, 1990; Tullis, 2002) e da presença de fluidos (Law, 2014) como ilustrado na FIGURA 11c. Alguns autores

sugerem que a abertura das guirlandas cruzadas tem correlação com a temperatura, e podem ser utilizadas como geotermômetros (Kruhl, 1996, 1998; Hunter et al., 2018).

O padrão das OCPs também reflete a geometria da deformação, logo, a forma do padrão pode revelar informações sobre o tipo ou a simetria da deformação (Figura 10a). Um volume de rocha deformado coaxialmente dispõe de padrões de OCP simétricos, sendo bastante comum o desenvolvimento guirlandas cruzadas do tipo I e do tipo II (FIGURA 10b, Lister, 1978). Aqueles que refletem uma trajetória de deformação não coaxial apresentam padrões assimétricos, normalmente na forma de guirlandas singulares ou cruzadas assimétricas (FIGURA 11c), e pode ser utilizado como indicador cinemático (e.g., Law, 1990; Kilian et al., 2011). O tipo de deformação uni-, bi- ou triaxial (como achatamento, deformação planar ou constrição) também formam distintos padrões de guirlanda para um mesmo sistema ou conjunto de sistemas de deslizamento ativos (Lister e Hobbs, 1980), como ilustrado na FIGURA 10a. Além disso, a progressão da deformação em um agregado pode acarretar na ativação de diferentes sistemas de deslizamentos e na acentuação de uma OCP (FIGURA 11c) (e.g., Heilbronner e Tullis, 2006).

3.5 REOLOGIA DO QUARTZO E FELDSPATO

A crosta continental é uma zona extremamente heterogênea, e por ser constituída por rochas com diferentes composições mineralógicas, seu comportamento reológico é bastante complexo, sendo controlado essencialmente por agregados poliminerálicos (Handy, 1990; Kenis et al., 2005). Além disso, os minerais apresentam diferentes resistências (*strength*) e deformam-se por meio de diferentes mecanismos de deformação dada a mesma condição físico-química de deformação (Dell'Angelo e Tullis, 1996; Tullis, 2002). Visto que, na porção intermediária da crosta, devido a sua composição majoritariamente granítica, há uma grande influência da reológica do quartzo e do feldspato (Fitz Gerald e Stuniz, 1993; Mukai, 2014; Wehrens et al., 2016), o estudo de ambas as fases é de suma importância para compreender o comportamento mecânico da crosta intermediária e o desenvolvimento de zonas de cisalhamento que comumente nucleiam nesta zona e acomodam grande parte da deformação crustal (FIGURA 12) (e.g., Schulmann et al., 1996; Park, 2006).

FIGURA 12 - Perfil reológico simplificado da crosta superior e intermediária indicando os mecanismos de deformação mais comuns observados no quartzo e feldspato.

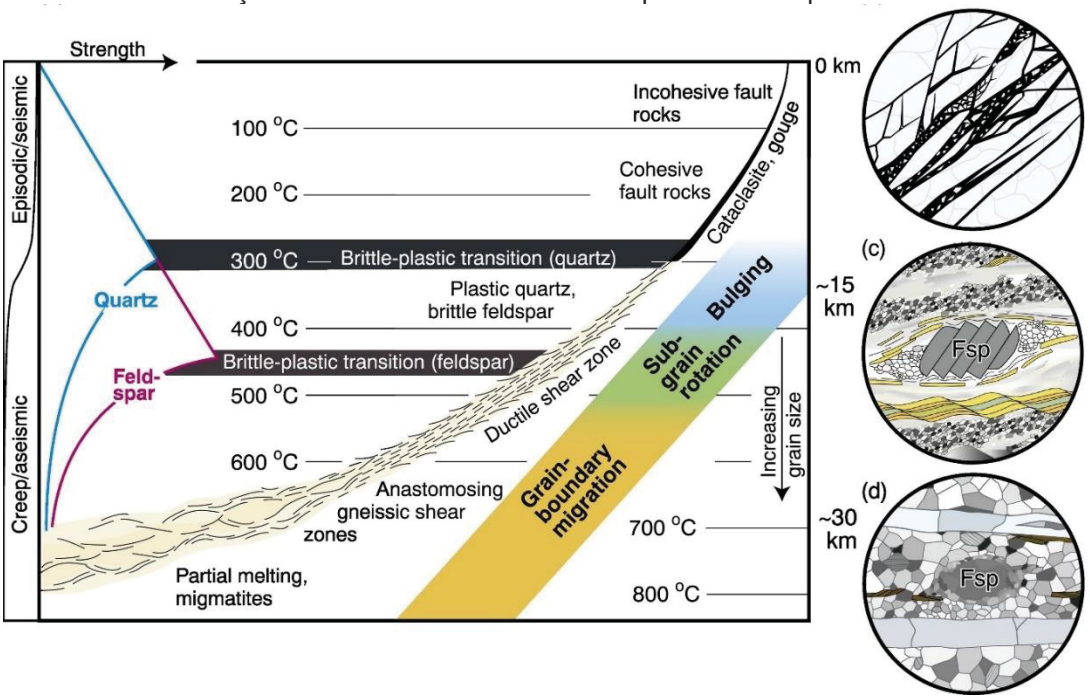

FONTE: Adaptado de Fossen e Cavalcante (2017).

3.5.1 Quartzo

O quartzo é um dos minerais mais amplamente estudados, com diversos trabalhos caracterizando experimentalmente e naturalmente as condições físico-químicas em que ocorrem os mecanismos de deformação cristal-plástica e na qual os sistemas de deslizamentos são ativados (e.g., Hirth e Tullis, 1992; Stoeckert et al., 1999; Stipp et al., 2002). Tais trabalhos sugerem que geralmente, entre 280 e 310°C, o deslizamento de deslocações supera o fluxo cataclástico como principal mecanismo de deformação do quartzo, definindo a chamada zona de transição rúptil-dúctil em uma crosta de composição granítica (Sibon, 1977). A partir desta temperatura, microestruturas típicas de recuperação e deformação intracristalina se tornam recorrentes e a recristalização por *bulging* começa a operar. A partir de 400 °C, a fluência por deslocações passa a ser dominante, com a SGR sendo o principal mecanismos de recristalização. Acima de temperaturas de 500°C a recristalização via GBM é prevalente. Stipp et al., (2002) ainda sugere que acima de 630°C a recristalização por migração de borda ocorre sem influência de *pinning*, juntamente com a transição do quartzo-α para o quartzo-β, e com o aparecimento de extinção

do tipo “xadrez” (*chessboard extinction).* Sob condições hidratadas o comportamento reológico se torna mais complexo (Tullis, 2002), e a temperatura na qual os mecanismos atuam diminuem drasticamente, sendo reportados a transição entre os três mecanismos em intervalos que compreendem 250 a 330°C (Dunlap et al., 1997).

Sua estrutura cristalográfica, definida por tetraedros de sílica em arranjos trigonais no quartzo-α (baixa temperatura) ou hexagonais no quartzo-β (alta temperatura) é bastante estável, e o deslizamento ocorre pelas quebras das ligações Si-O nas direções mais curtas (Lister et al., 1978). No quartzo os planos de deslizamento mais comuns são respectivamente os planos prismático{m}, romboédrico positivo{r} e negativo{z}, e basal (c), e as direções são os eixtos <a> e [c] (FIGURAS 11a e 11b, Lister et al., 1978; Tullis, 2002). O quartzo também apresenta outros sistemas de deslizamentos, mas em geral são subordinados, e raramente reportados em rochas naturalmente deformadas.

3.5.2 Feldspato

Devido a presença de clivagens excelentes, largas celas unitárias e baixa simetria os feldspatos possuem sistemas de deslizamentos mais restritos e complexos do que os apresentados pelo quartzo, o que dificulta o deslizamento de deslocações (Tullis, 1983). Consequentemente o feldspato começa a apresentar um comportamento dúctil em temperaturas superiores em relação ao do quartzo (450-500°C, Tullis, 2002). Além disso, a transição de deformação dominada por fluxo cataclástico para dominada por fluência de deslocações acomodada por recristalização pode ocorrer sobre um amplo intervalo de temperaturas (Tullis e Yund, 1987), com o feldspato, mesmo sob altas temperaturas (>700°C), ainda podendo apresentar comportamento rúptil devido a sua complexidade estrutural e química (Tullis, 2002; Menegon et al., 2013). Alguns trabalhos sugerem que os primeiros indícios de deformação intracristalina do feldspato (extinção ondulante, *kink bands*, geminações mecânicas) começam a surgir por volta de 400 a 500 °C de temperatura (Passchier e Trouw, 2005). Apesar de que algumas destas microestruturas possam ser produto de microfissuramento (Tullis e Yund, 1987), a transição de regime rúptil-dúctil para dúctil na crosta situa-se em torno desta temperatura. De acordo com Tullis (2002) entre 400 e 650°C os cristais de

feldspatos podem começar a ser afetados pela recristalização por *bulging* (regime 1 de fluência de deslocações). Já a recristalização por rotação de subgrão (regime 2) é dominante em condições de alto grau metamórfico de fácies anfibolito superior, granulito ou eclogito (cerca de 600 e 850°C). Por outro lado, a recristalização por migração de borda de grão (regime 3) são muito raras, sendo observadas em rochas deformadas em condições de ultra-alto grau metamórfico (>850°), próximo ao *solidus* da rocha. Contudo, a presença de água pode reduzir drasticamente a temperatura na qual a recristalização começa a atuar.

Como abordado previamente, os sistemas de deslizamento nos feldspatos são bem restritos, e os sistemas variam conforme a composição e estrutura cristalina do tipo de feldspato. Em geral, os planos de deslizamento mais comuns são aqueles associados a planos com menor quantidade de ligações T-O por área, como os planos de clivagem (010) e (001), e as direções de deslizamento com a distância de repetição mais curtas como [001], [110] e [100] (Tullis, 2002). Os sistemas de deslizamento mais comuns observados naturalmente para o plagioclásio são (001)[100], (010)[100] e (001)<110> (Satsukawa et al., 2013); já para os feldspatos alcalinos é o plano (010) nas direções [100], [001] e [101] (Menegon et al., 2008). A tabela 1 e a Figura 13 lista outros sistemas de deslizamentos reportados na literatura tanto para o plagioclásio, quanto para o feldspato potássico.

FIGURA 13 - Projeção dos planos e direções de deslizamento mais comuns no (a) feldspato alcalino monoclínico (2/m) e no (b) plagioclásio com estrutura C1.

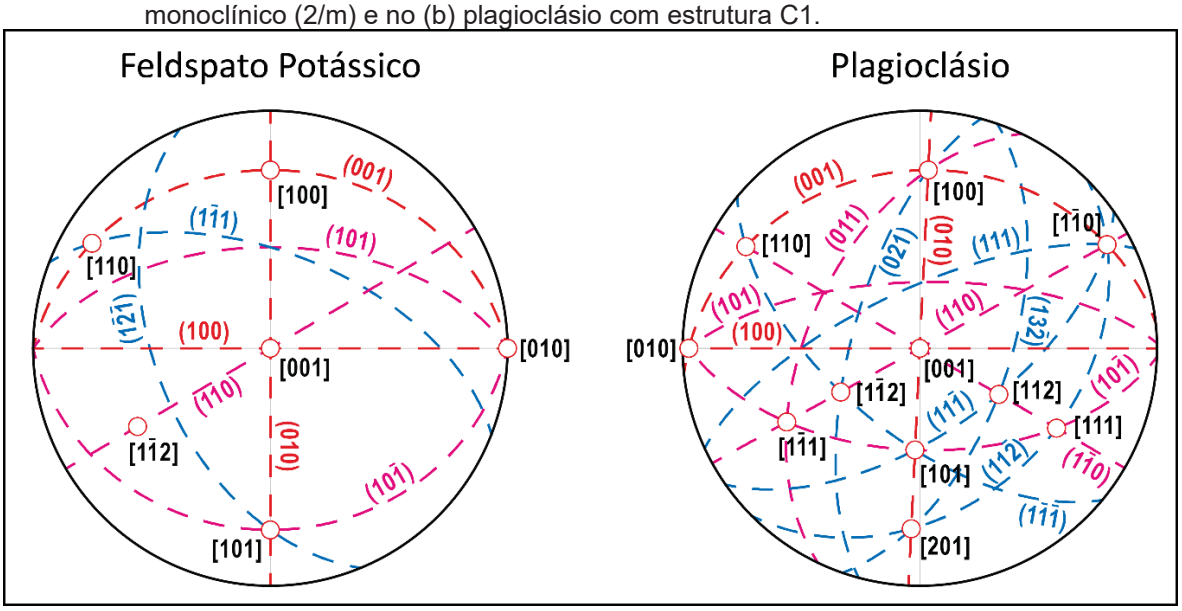

TABELA 1 - Sistemas de deslizamentos determinados em cristais experimentalmente e naturalmente deformados de feldspato potássico e plagioclásio reportados na literatura. Legenda: M.A = Método analítico, E = Espécime experimentalmente deformada, N = Espécime naturalmente deformada, TEM = Microscópio eletrônico de transmissão, EBSD = Difração por elétrons retroespalhados, US = Estágio universal.

Sistemas de deslizamento em feldspatos alcalinos			
Planos	Direções	Deformação da amostra	M.A
(010)	[100]	E (1, 2); N (4, 5, 6)	TEM, EBSD
	[001]	E (1, 2); N (4, 5, 7, 9, 10)	TEM, EBSD
	[101]	E (1, 2); N (4)	TEM, EBSD
	½[1-12]	N (4)	TEM, EBSD
(001)	[100]	N (6)	EBSD
	½[110]	E (1, 2)	TEM, EBSD
(100)	[010]	N (8)	EBSD
	[001]	N (9)	EBSD
(110)	½[1-12]	E (1, 2)	TEM, EBSD
(101)	[010]	N (8)	EBSD
(10-1)	[101]	N (3)	TEM
(1-2-1)	[101]	E (1, 2); N (4)	TEM, EBSD
(1-11)	½[110]	E (1, 2)	TEM, EBSD
1: Willaime et al. (1979)	5: Schulmann et al. (1996)	9: Oliot et al., (2014)	
2: Scandale et al. (1983)	6: Martelat et al. (1999)	10: Czaplinska et al., (2015)	
3: Willaime e Gandais (1977)	7: Franek et al. (2006)		
4: Sacerdoti et al. (1980)	8: Ishii et al. (2007)		
Sistemas de deslizamento no plagioclásio			
Planos	**Direções**	**Deformação da amostra**	**M.A**
(010)	[100], ½[100]	E (1), N (3, 9, 7)	TEM, EBSD
	[001], ½[001]	N (2, 3, 4, 5, 6, 7, 8, 10, 11)	TEM, EBSD, US
	½[110]	N (11)	TEM
	[101]	N (2)	TEM
(001)	[100]	E (1), N (9, 10)	TEM, EBSD
	[110], ½[110]	N (2, 5, 6, 8)	TEM, EBSD
	½[1-10]	N (2)	TEM
(110)	½[1-12]	N (2)	TEM
(1-10)	[110]	E (1)	TEM
(011)	[100]	N (10)	EBSD
	[1-11]	N(12)	TEM
(101)	½[111]	E (1)	TEM
	½[1-11]	E (1)	TEM
	½[201]	E (1)	TEM
	[101]	E (1)	TEM
(10-1)	½[111]	E (1), N (10)	TEM, EBSD
	½[1-11]	E (1)	TEM
(111)	[110]	N (6, 10)	TEM, EBSD
(11-1)	½[1-10]	N(2)	TEM
	½[112]	N(2)	TEM
(1-1-1)	[110], ½[110]	N (2, 5, 10)	TEM, EBSD
(11-2)	½[201]	E (1)	TEM
(13-2)	½[111]	E (1)	TEM
	½[201]	E (1)	TEM
(021)	[1-12]	N (3, 8, 13)	EBSD, US
1: Marshall e MacLaren (1977a, 1977b)	5: Kruse et al., (2001)	10: Miranda et al., (2016)	
2: Olsen and Kohlstedt (1984)	6: Stünitz et al., (2003)	11: Olsen e kohlstedt (1981)	
3: Kruhl (1987)	7: Mehl e Hirth (2008)	12: Montard and Mainprice (1987)	
4: Shaocheng e Mainprice (1988)	8: Svahnberg and Piazolo (2010)	13: Baratoux et al., (2005)	
	9: Satsukawa et al., (2013)		

4 MATERIAIS E MÉTODOS

4.1 MICROSCÓPIO ELETRÔNICO DE VARREDURA

O Microscópio Eletrônico de Varredura (MEV) é um dos instrumentos de imageamento mais versáteis e amplamente utilizado nas geociências para a caracterização das superfícies dos materiais em escala nanométrica a micrométrica, devido principalmente a simplicidade de preparo da amostra e ao baixo custo de operação. Um típico MEV consiste de uma fonte de emissão, na qual gera um feixe concentrado de elétrons altamente energéticos dentro de uma câmara selada a alto vácuo e detectores para a captação de diferentes tipos de radiação. A interação entre os elétrons do feixe e o espécime é utilizado para obter informações acerca da topografia, composição, cristalografia, dentre outras propriedades físicas e químicas de um espécime (Goldstein et al., 2018).

FIGURA 14 - Ilustração simplificada dos diversos tipos de eventos de espalhamento que ocorrem dentro do volume de interação.

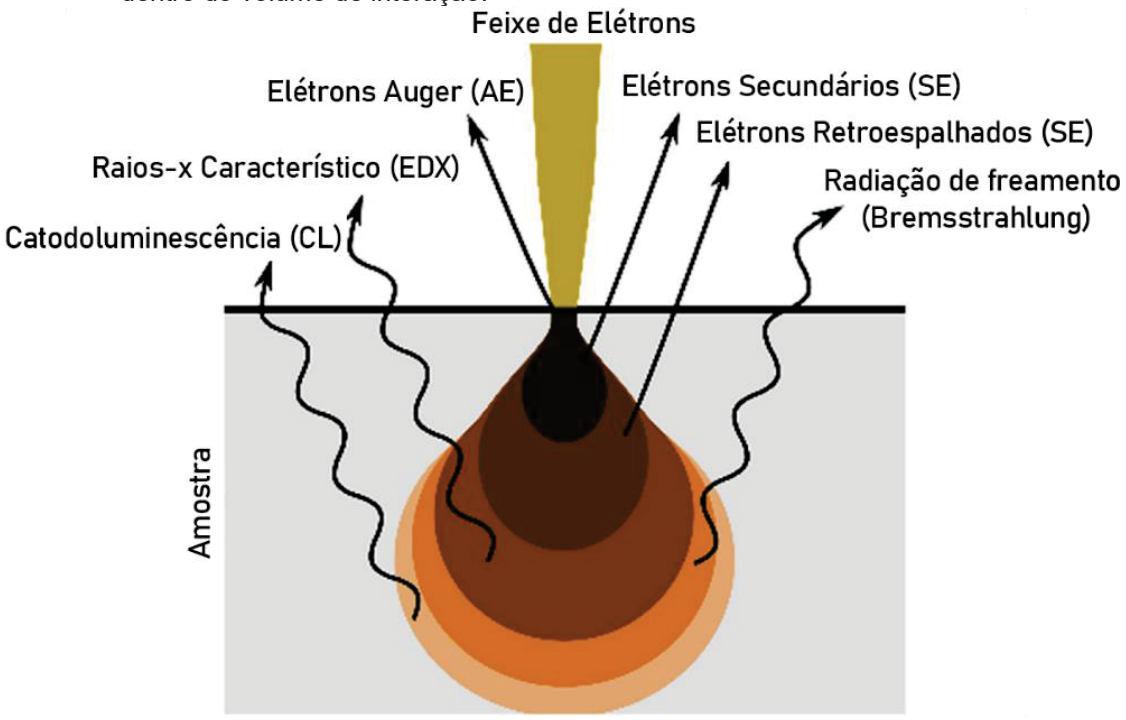

FONTE: Modificado de Ezzahmouly et al., 2019

Assim que um feixe de elétrons de alta energia atinge a superfície de um material, os elétrons do feixe interagem com o alvo por meio de uma série de “eventos de espalhamentos”, dentro de uma região denominada de volume de

interação ou “pera de ionização” (Goldstein et al., 2018). Dentro deste volume os elétrons do feixe interagem com os átomos do espécime, transferindo a energia do feixe para os átomos do espécime. Tais eventos incluem interações elásticas e inelásticas, além da emissão de elétrons secundários e retroespalhados (produtos das interações elásticas e inelásticas respectivamente), elétrons auger, raios-x, catodoluminescência e de elétrons transmitidos (FIGURA 14). A microscopia eletrônica de varredura trabalha principalmente na captação e processamento destas radiações, gerando produtos tais como imagens topográficas ou de contrastes composicionais a partir da captação de elétrons retroespalhados e secundários por meio de seus detectores. Outros detectores podem ser acoplados ao equipamento para a detecção de outras tipos de emissão tais como a catodoluminescência.

4.2 DIFRAÇÃO DE ELÉTRONS RETROESPALHADOS (*ELECTRON BACKSCATTER DIFFRACTION* – EBSD)

Introduzida no MEV, a Difração de elétrons retroespalhados (*Electron Backscatter diffraction* – EBSD) é uma das técnicas analíticas mais amplamente utilizadas nas ciências da terra para uma completa análise textural quantitativa de diversos materiais geológicos. Em comparação as técnicas mais antigas, tais como a platina universal acoplada em um microscópio óptico ou o difratômetro de Raios-X com goniômetro de texturas, o EBSD permite uma rápida aquisição de dados cristalográficos de forma relativamente simples, rápida, automática e estatisticamente significante de diversos minerais pertencentes aos sete sistemas cristalográficos, desde o cúbico ao triclínico (Mariani et al., 2008). A técnica possibilita a investigação e obtenção de diversas informações a respeito do espécime analisado, que incluem a identificação de fases minerais e a obtenção de desorientações, orientações cristalográficas, mapas de orientação, geometria de bordas de grãos e subgrãos, medição de *strain*, entre outros (Mariani et al., 2008; Randle, 2008).

4.2.1 Princípio

Dentre as principais formas de interação entre os elétrons do feixe e os átomos do espécime estão as interações inelásticas e elásticas. Os espalhamentos inelásticos consistem de diferentes tipos de processos físicos que tendem a reduzir a energia dos elétrons do feixe transferindo sua energia para os átomos do espécime. Já os espalhamentos elásticos envolvem deflexões ao redor do campo elétrico de um átomo com ângulos que variam entre 0 e 180° de acordo com a proximidade do elétron com o núcleo do átomo do espécime, em que há pequena ou nenhuma perda significante de energia (Prior et al., 1999). Como o diâmetro do feixe é maior do que o espaçamento atômico, os elétrons incidentes encontram-se em diferentes distâncias em relação aos átomos do espécime, e, consequentemente, irão ser espalhados em diversas direções. Aqueles elétrons que sofrem um ou mais eventos de espalhamento e emergem do espécime via superfície de incidência são chamados de elétrons retroespalhados (Mariani et al., 2008). Dentre os elétrons retroespalhados, aqueles que satisfazem a equação de Bragg (Eq. 1) para certos planos cristalográficos sofrem a difração, percorrendo trajetórias que, tridimensionalmente, apresentam formas cônicas, sendo denominados de cones de difração ou cones de Kossel (FIGURA 15).

$$n\lambda = 2d \sin\theta \quad \text{(Eq. 1)}$$

Cada plano cristalográfico gera dois cones de difração, cuja intensidade depende do tipo de átomo presente no plano (Prior et al., 1999). Em seguida, os cones são projetados e imageados em uma tela fosforescente como mostrado na FIGURA 15. A equação de *Bragg* mostra que comprimentos de onda curtos de elétrons, típicos da voltagem de aceleração usada no MEV (10-30 kV), resultam em ângulos de Bragg de aproximadamente 2°, por consequência a projeção destes cones na tela ocorre na forma de duas linhas paralelas aproximadamente retilíneas denominadas de linhas de Kikuchi e que formam as bandas de Kikuchi (FIGURA 15). As linhas de uma banda são separadas por uma distância que equivale ao dobro do ângulo de Bragg. A linha mediana da banda representa o plano cristalográfico que difratou o feixe. As bandas de kikuchi se intersectam em vários pontos luminosos chamados de eixos de zona, que correspondem as direções cristalográficas. As bandas de Kikuchi juntamente com eixos de zonas formam o padrão de elétrons retroespalhados (*electron backscattering pattern* – EBSP) ou padrão de Kikuchi na qual pode ser interpretado como a projeção goniométrica da

estrutura cristalina do espécime (Schwarzer et al., 2009), deste modo, a partir de um processo chamado de indexação, os elementos de simetria da estrutura cristalina podem ser reconhecidos e a orientação da estrutura em relação a um sistema de referência pode ser obtida.

FIGURA 15 - Ilustração simplificada da difração de elétrons retroespalhados e a geração das linhas de kikuchi.

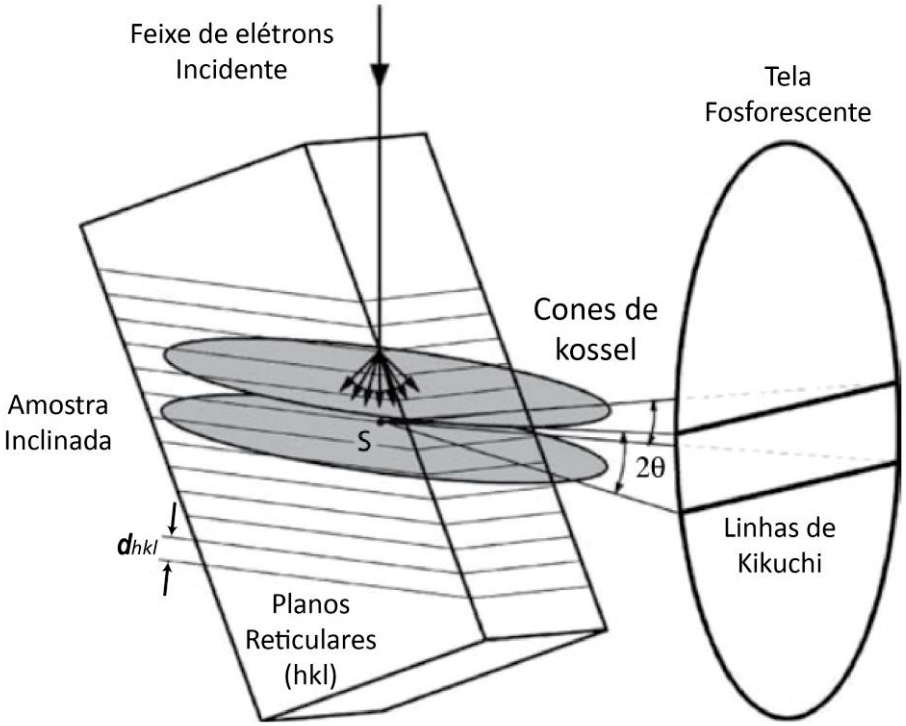

FONTE: Randle (2010).

4.2.2 Configuração e condições de rotina

A técnica MEV-EBSD compreende 3 componentes principais (Schwarzer et al., 2009):

- MEV
- Dispositivo de aquisição de padrão (ou câmera)
- Software

Estes componentes são integrados conforme ilustrado na FIGURA 16. Nesta configuração a amostra é fixada em um estágio dentro da câmara do MEV inclinado a 20° em relação ao feixe de elétrons disparado geralmente por um canhão de emissão de campo (Field Emission Gun – FEG) situado geralmente entre 15 e 30 mm de distância (*working distance*). O dispositivo de aquisição é composto por uma

tela fosforescente e uma câmera CCD posicionada logo atrás. O dispositivo é móvel e geralmente é posicionado a 2 cm da amostra, na qual permite que a tela capture um EBSPs com um grande alcance angular (Mariani et al., 2008). Esta distância entre o ponto de origem (*source point*) e o centro do padrão (*pattern center*) é chamada de distância tela-espécime. O software é responsável pelo controle da câmera, processamento de dados, indexamento de padrões, analises e pela geração dos dados de saída (*outputs*).

FIGURA 16 - Configuração dos componentes presentes em um MEV com detector de EBSD acoplado.

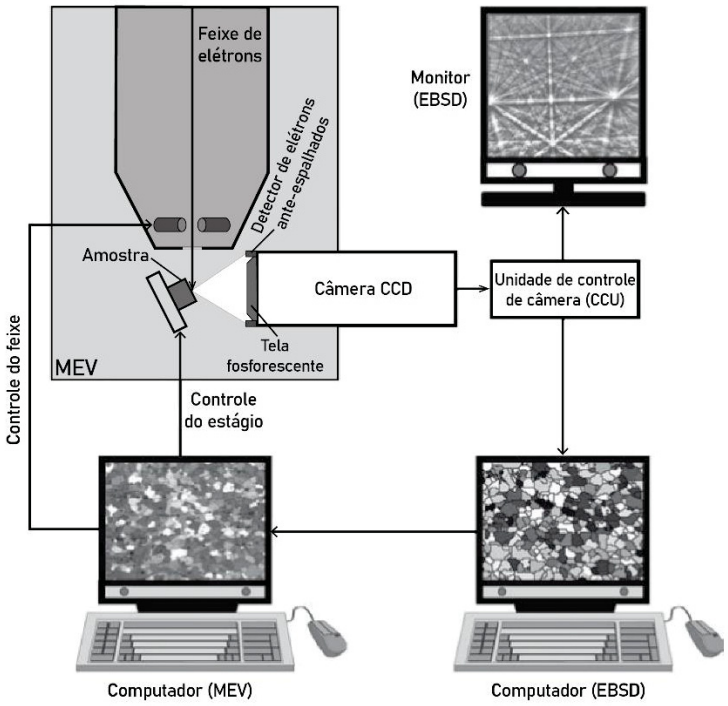

FONTE: Modificado de Randle (2010).

4.2.3 Preparação das amostras

A rotina de preparação segue 3 etapas: polimento mecânico, polimento químico e o revestimento. O polimento mecânico é feito com pasta diamantada, nessa etapa é realizada a remoção de irregularidades na superfície do espécime com o objetivo de se obter uma superfície o mais plana possível. O polimento químico é realizado utilizando uma solução de sílica coloidal, que é responsável pela eliminação da camada amorfa produzida durante o desbaste mecânico. A rotina de preparação adotada está ilustrada de maneira simplificada na FIGURA 17. O

polimento mecânico consistiu em 3 estágios de polimento consecutivos de 30 minutos cada em uma politriz, utilizando-se de pastas diamantadas de 3, 1 e 0,25 µm. A seguir, as amostras foram polidas quimicamente durante 90 minutos. Após o polimento as lâminas foram limpas utilizando-se de um equipamento de ultrassom e as áreas a serem analisadas foram delimitadas por fitas de cobre. O revestimento por fita de cobre ou carbono é essencial para espécimes não condutoras, pois ele reduz o efeito do carregamento e o do dano do feixe (*beam damage*) (Randle, 2010).

FIGURA 17 - Rotina de preparação das amostras para EBSD e MEV.

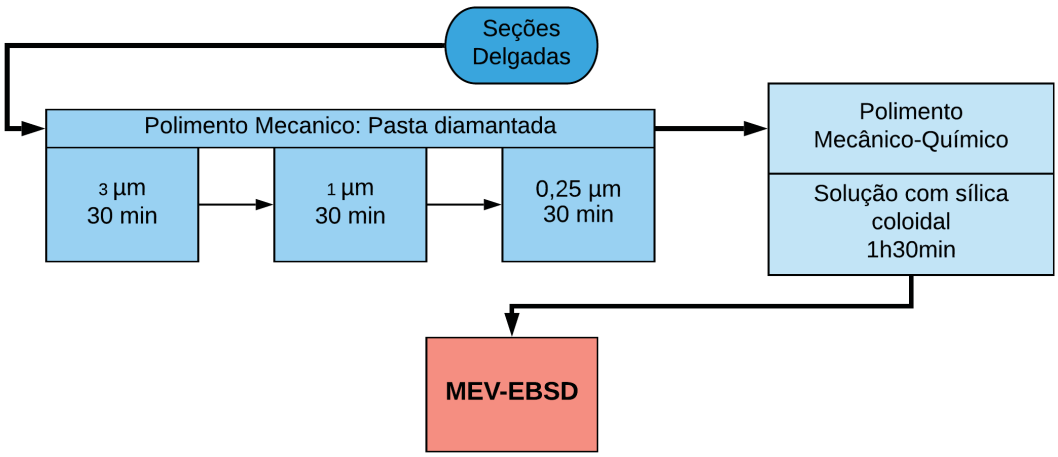

Para a realização das análises no microscópio eletrônico de varredura para a aquisição das imagens de retroespalhamento, as lâminas polidas foram cobertas com uma fina camada de carbono.

4.3 REPRESENTAÇÃO DAS TEXTURAS

Após a indexação dos padrões e as devidas correções cada ponto analisado é armazenado com informações sobre a fase, orientação cristalográfica (expressa em ângulos de Euler), coordenadas espaciais, índice de confidência, dente outros. Há diversos meios de expressar tais dados graficamente com o intuito de investigar a textura da amostra.

4.3.1 Ângulos de Euler (*Euler Angles*)

Por meio dos ângulos de Euler é possível realizar no software operações de rotação e transformação entre sistemas de coordenadas presente no EBSD. Este método se refere a três rotações que transformam um sistema de coordenada em outro. Existem diversas convenções para expressar os ângulos de Euler. A convenção mais utilizada, definida por Bunge (1965) (FIGURA 18), define que as três rotações são operadas sucessivamente na seguinte ordem:

ϕ_1 = Rotação em torno do eixo Z
φ = Rotação em torno do eixo X'
ϕ_2 = Rotação em torno do eixo Z''

Onde ϕ_1, φ, ϕ_2 são os ângulos de Euler.

FIGURA 18 - Operações que definem os três ângulos de Euler (ϕ_1, φ, ϕ_2).

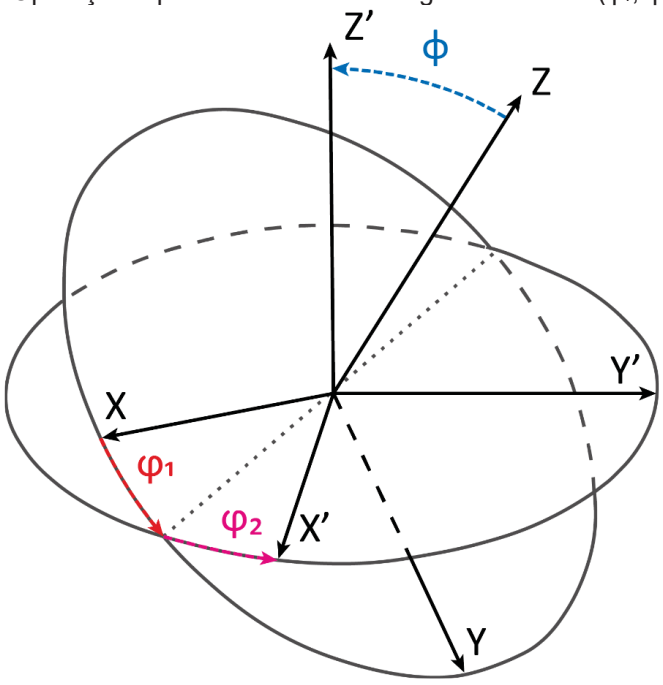

FONTE: Modificado de Bunge (1982).

4.3.2 Figura de polo e figura de polo inversa (*Pole figure and Inverse Pole figure*)

A figura de polo (FIGURA 19c) é um dos meios mais tradicionais de se representar as texturas devido a facilidade na visualização das orientações de certos planos e direções cristalográficas. A direção de qualquer vetor - seja normal a um plano cristalográfico ou representando uma direção cristalográfica - pode ser plotada

em uma esfera unitária atrelada a um referencial externo, no caso o sistema de coordenadas do espécime, que em amostras geológicas correspondem a orientação da foliação e lineação. A intersecção deste vetor com a esfera de referência origina um polo, que é projetado em um plano bidimensional horizontal no centro da esfera conforme ilustrado na FIGURA 19a. A posição deste polo no espaço é dada pelos ângulos α e β, que descrevem respectivamente os ângulos azimutais e de rotação ao redor do eixo polar.

FIGURA 19 - a) Esfera de referência e a projeção de um polo referente a um eixo de um objeto no plano de projeção equatorial. b) Representação da orientação de um objeto no espaço de Euler, princípio de construção de Funções de Distribuição de Orientações. c) Figura de Polo e (d) figura de Polo Inversa mostrando respectivamente a projeção de um polo corresponde ao plano basal (0001) do quartzo e de um polo correspondente ao eixo x do espécime.

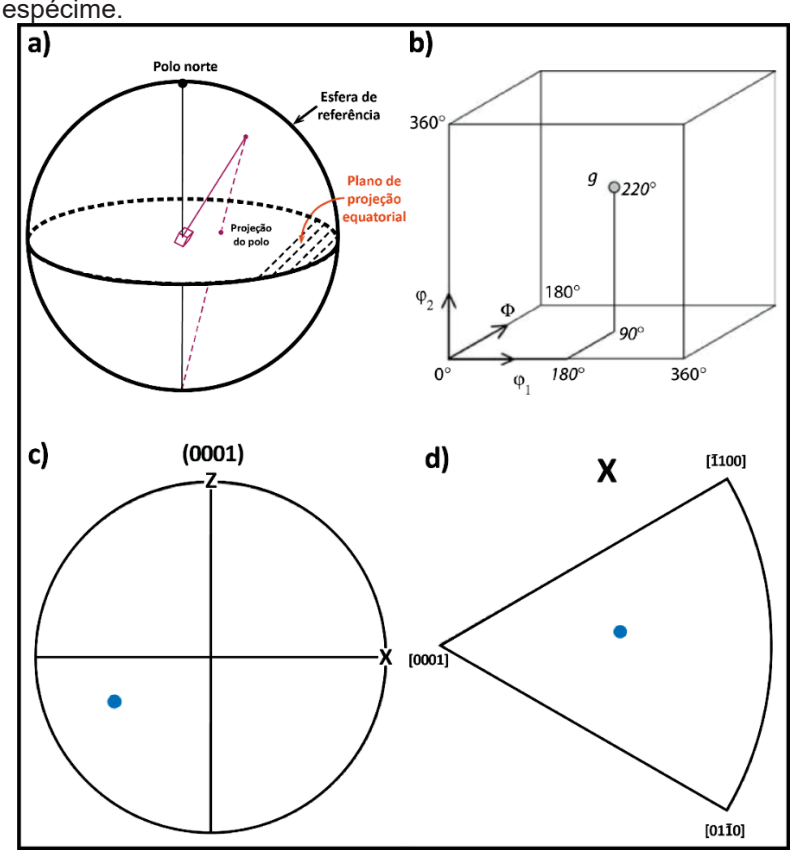

FONTE: a) Modificado de Randle (2010) e b) Passchier and Trouw (2005).

Ao invés de representar eixos cristalográficos usando o sistema de coordenadas do espécime como referência pode se fazer o inverso, ou seja, representar os eixos do espécime no sistema de coordenadas do cristal na chamada figura de polo inversa (FIGURA 19d). A projeção dos eixos do espécime é realizada de forma similar as feitas nas figuras de polo. Contudo, devido aos elementos de

simetria presentes nos cristais, não é necessário representar o estereograma em sua totalidade, mas partes equivalentes simétricas (exceto para cristais de simetria triclínica).

4.3.3 Funções de Distribuição de Orientações (*ODFs)*

A representação das orientações de planos e direções cristalográficas nas figuras de polo, um espaço bidimensional, resulta em orientações não totalmente definidas, pois contam com apenas duas das três variáveis necessárias para uma determinação inequívoca da orientação de um vetor em um espaço. Afim de superar a perda de informação, pode-se representar uma orientação por meio de ângulos de Euler em um espaço de Euler, tal como mostrado na FIGURA 19b.

Informações quantitativas relativas as orientações cristalográficas de uma população de cristais em um volume do espécime podem ser obtidas por meio das funções de distribuição de orientação (*orientation distribution function – ODF)*. Tais funções são funções densidade de probabilidade que descreve, por meio dos ângulos de Euler, uma fração de volume de elementos de um material com uma orientação cristalográfica particular dentro de um certo elemento infinitesimal de orientação (Wenk, 1985). Por meio dos ODFs é possível calcular o índice de textura de uma população de cristais conhecido como *J-index* (Bunge, 1982).

4.3.4 Mapas de orientação (*Orientation maps*)

FIGURA 20 - Típicos mapas produzidos a partir de dados de EBSD. a) Mapa de fases; b) mapa de contraste de banda; c) Mapa de orientação (sobre o contraste de banda) e d) mapa com as bordas entre os cristais.

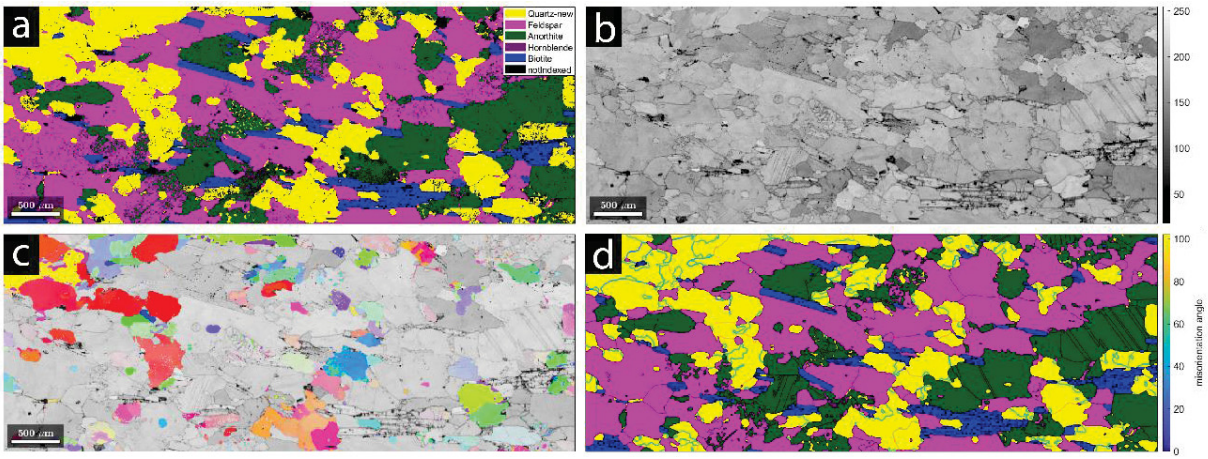

Uma outra forma de representar espacialmente os dados cristalográficos é por meio dos mapas de orientações. Tais mapas combinam informações sobre as orientações cristalográficas com a informação espacial da microestrutura (Randle, 2010). Estes mapas destacam visualmente diversas características morfológicas e físicas dos cristais, tais como a distribuição das fases (FIGURA 20a), orientação dos cristais (FIGURA 20c), textura, desorientações entre os cristais (bordas entre os cristais) (FIGURA 20d) além da intensidade de deformação interna (*strain*), observado principalmente via mapas de contraste de banda (FIGURA 20b), dentre outros.

4.3.5 Desorientação entre cristais (*Misorientations*)

Dentro de uma população de cristais em um espécime, é possível expressar a orientação de um cristal em relação ao sistema de coordenadas de outro cristal, podendo ser vizinho ou não. Desta forma, quando se trata da mesma fase, a orientação dos eixos de um cristal A expressa em relação ao cristal B define uma desorientação (FIGURA 8). A desorientação entre dois cristais A e B é dada por:

$$G = A^{-1}B \quad \text{(Eq. 2)}$$

Na qual *G* é a matriz que representa a desorientação entre o cristal A e B, em que o cristal A é o referencial. A notação é expressa pelo par eixo/ângulo de misorientação, cujo eixo de rotação é, por definição, representado por uma direção cristalográfica comum aos dois cristais (FIGURA 21) e, portanto, pode ser representada por um único ponto (Randle, 2010).

Os eixos e ângulos de misorientação geralmente são representados separadamente. Os eixos em geral são plotados em estereogramas cujo sistema de coordenadas pode ser o do espécime (FIGURA 22a) ou do cristal (FIGURA 22b). A distribuição dos ângulos de misorientação de uma população de cristais pode ser representada por meio da distribuição estatística em histogramas, na qual são comparadas as distribuições das misorientações entre pares de cristais vizinhos, entre pares não vizinhos e de uma população teórica cuja distribuição é randômica (cujo aspecto varia dependendo da simetria do material) (FIGURA 22c).

FIGURA 21 - Desorientação entre dois cristais hipotéticos definido pela rotação de 50° em torno do eixo [001] compartilhado por ambos os cristais.

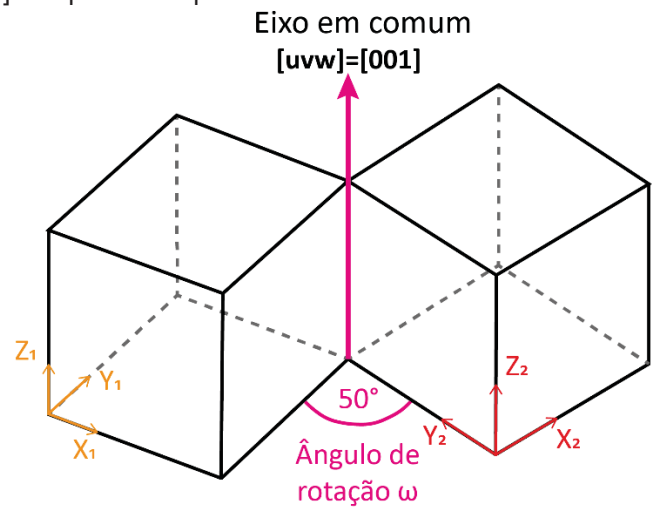

FONTE: Modificado de Randle (2010).

FIGURA 22 - Eixos de desorientação plotados em relação ao (a) sistema de coordenadas do espécime e ao (b) sistema de coordenadas do cristal. c) Histogramas mostrando a frequência de ângulos de desorientações entre pares correlatos (barras pretas) e não correlatos (barras cinzas), bem como a curva de distribuição randômica teórica.

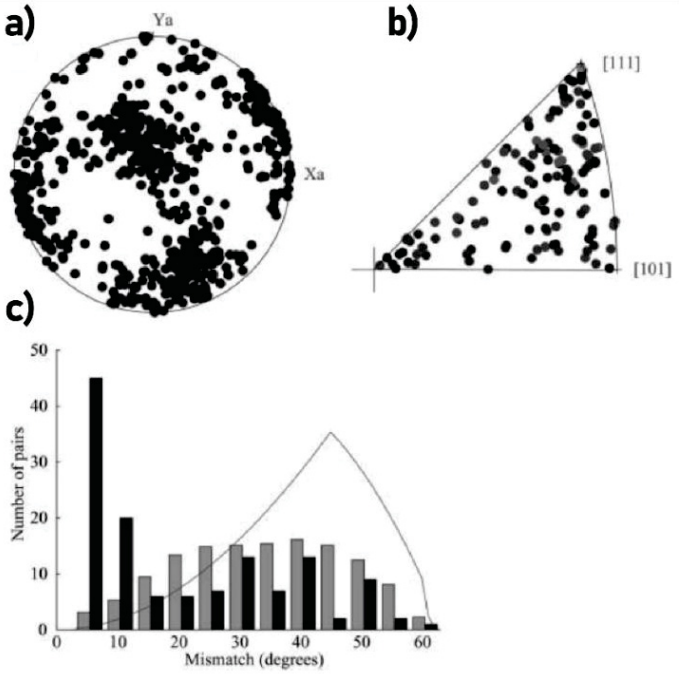

FONTE: Modificado de Wheeler et al. (2001).

Vale ressaltar que para cristais de alta simetria há mais de uma solução para o cálculo da misorientação devido ao problema das variantes simétricas. Devido a isto, normalmente se utiliza por convenção o par com menor ângulo de misorientação.

5 RESULTADOS – MICROSTRUCTURES, SLIP SYSTEMS AND STRAIN LOCALIZATION IN QUARTZO-FELDSPATHIC MYLONITES FROM PATOS SHEAR ZONE REVEALED BY EBSD DATA

5.1 INTRODUCTION

The ductile deformation of the lithosphere is commonly accommodated along localized ductile high-strain zones which register large amounts of kilometric displacement (Burlini and Bruhn, 2005; Fossen and Cavalcante, 2017). The localization and evolution of these structures in the micro-scale have been discussed in terms of the rheological contrast among the different phases and the processes which lead to strain weakening (Handy, 1990, Handy, 1994; Platt, 2015; Cross et al., 2020). At mid-crust conditions, due to the predominant granitic composition, the bulk rheology is generally taken as controlled by the quartz and feldspar rheology (Fitz Gerald and Stünitz, 1993; Schulmann et al., 1996) with both minerals undergoing intracrystalline plasticity (Simpson, 1985; Tullis, 2002; Behr and Platt, 2011). However, due to the polymineralic nature of rocks, the deformation during the shear zone evolution is far from being homogeneous.

Several mechanisms like softening reactions (e.g., Oliot et al., 2010; Ceccato et al., 2018), dynamic recrystallization (e.g., Shigematsu, 1999; Bestmann and Prior, 2003), solution-transfer mechanisms (e.g., Wintsch and Yi, 2002; Fukuda and Okudaira, 2013) and fracturing (e.g., Ree et al., 2005; Menegon et al., 2013) may act to reduce the grain size of minerals and/or produce weak minerals. Thus, the strain is localized by reducing the strength of the rock (Linckens et al., 2011; Platt and Behr, 2011). Grain-size reduction results in the switch to grain size sensitive (GSS) mechanisms like grain boundary sliding, diffusion creep or granular flow (e.g., Behrmann and Mainprice, 1987; Oliot et al., 2014) which allow the high strain zones to accommodate more strain at low stress (Platt, 2015). Nevertheless, most of the studies that investigated the role of grain-size reduction mechanisms during the mylonitization of quartzo-feldspathic rocks focus on small shear zones (e.g., Menegon et al., 2006; Kilian et al., 2011; Oliot et al., 2014; Czaplinska et al., 2015) with few studied in detail both quartz and feldspar to constrain the microstructural evolution and deformation partitioning on large scale shear zones (e.g., Dong et al., 2019). Therefore, the study of deformation mechanisms and deformation partitioning

between quartz and feldspar in large zones of high strain is one more key for understanding how these structures produce crustal weakening in the middle crust.

The Patos shear zone (PSZ) is a large syn-magmatic shear zone nucleated and developed during the last stages of Brasiliano orogeny (ca. 565 Ma, Viegas et al., 2014). PSZ consists mostly of quartzo-feldspathic basement rocks mylonitized under low- to high-temperature conditions that allowed a record of the deformation under several conditions during the uplifting (Corsini et al., 1991). It is well known that the PSZ was nucleated during the widespread partial melting. However, the microstructural evolution during the solid-state partitioning is still poorly understood since previous studies have been concentrated on structural, geochronological and geochemical investigations (e.g., Corsini et al., 1991; Hackspacher et al., 1997; Monié et al., 1997; Corsini, 1998). Recent studies by Viegas et al., (2013) and Viegas et al., (2014) addressed aspects of the microstructures and crystallographic textures of the PSZ and pointed out the heterogenous nature of deformation. Nevertheless, those studies concentrated in parts of the shear zone and a broader investigation in other parts of the PSZ are still lacking.

In this contribution, we investigate in different scales the microstructures and the texture of quartz and feldspar in mylonites deformed under different conditions along the Western and Central segments of PSZ in order to comprehend the solid-state deformation partitioning and the processes which led to the strain localization and crustal weakening during the PSZ uplifting.

5.2 GEOLOGICAL CONTEXT

The Patos Shear Zone (PSZ) consists of a ~600 km long and up to 30 km wide E-trending strike-slip ductile shear zone (Viegas et al., 2013) which constitute a tectonic boundary that separates the Archean/Paleoproterozoic basement of the Rio Grande do Norte Domain (RGND) to the north from the Meso- to Neoproterozoic rocks of the Transversal Zone (ZT) to the south (Van Schmus et al., 2008; Van Schmus et al., 2011) and has been interpreted as an ancient continental transform fault (Brito Neves et al., 2016). It is part of the western domain of the Borborema Shear Zone system (Fig. 1a), a continental network of large-scale shear zone developed due to the convergence between the Congo-São Francisco, Amazon and West-African/São Luís cratons during the Neoproterozoic Pan-African/Brasiliano

orogeny (Vauchez et al., 1995; Arthaud et al., 2008). The PSZ is composed of an anastomosed network of high-temperature shear zones characterized by medium- to high-grade mylonites and less deformed lens where crops out migmatitic granites and anatexites (Archanjo and Fetter, 2004). The southern border of the PSZ is limited by a ~1-2 km wide discontinuous low-grade mylonites and ultramylonites belt (dashed black lines in Figure 1a) which rework the high-grade rocks and separates its northern part from the low-grade Cachoeirinha-Salgueiro belt (Corsini et al., 1991; Vauchez et al., 1995).

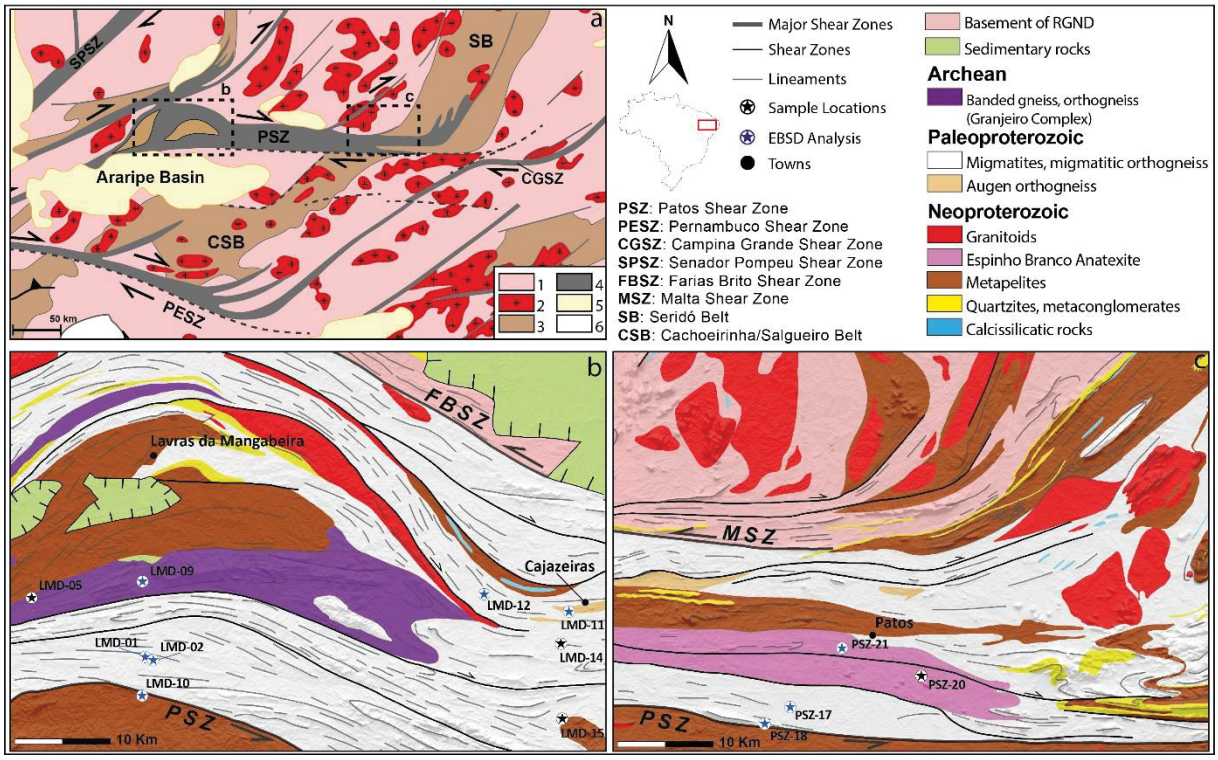

FIGURE 1 - (a) Schematic map of Borborema Shear Zone System showing the major shear zones, tectonic domains and the two studied areas (adapted from Neves, 2000 after Vauchez et al., 1995). The numbers indicate Basement rocks (1); Brasiliano granitoids (2); Schist belts (3); High-Temperature Shear Zones (4); Basins (5); São Francisco Craton (6). The low-temperature shear zones are represented by the dashed black lines. (b) and (c) are simplified geological maps of the studied areas showing the main rocks and trend of structures present in the Western and Central Domain of the PSZ, respectively. The stars indicate the outcrops visited and the blue stars mark the sites where samples were collected for EBSD analysis. The Geological map of the studied area was compiled from Angelim et al., (2004); Medeiros et al., (2005); Viegas et al., (2013); Hollanda et al., (2015); Costa et al., (2018); Palheta et al., (2019).

The PSZ is divided into three structural domains: Western, Central and Eastern domain (Viegas et al., 2013; Cavalcante et al., 2016). The Western domain (Fig. 1b) is characterized by a strike-slip duplex structure referred to as Lavras da Mangabeira Duplex (LMD; Corsini, 1996; Hollanda et al., 2015). The duplex connects

the PSZ with the Potengi and Tatajuba Shear Zones. It juxtaposes basement rocks as Archean gneiss of Granjeiro Complex and Paleoproterozoic orthogneisses of Caicó Complex with supracrustal units such as Neoproterozoic metapelites of Lavras da Mangabeira formation and syn-kinematic granitoids through a network of anastomosed shear zones and thrusts slices (Corsini, 1996). In the eastern part of LMD, the trend of the shear zone-related structures converges into the central domain of PSZ. The Central domain (Fig. 1c) of PSZ is mainly composed of high-grade mylonites, migmatitic orthogneisses and migmatitic granites of Caicó Complex and minor metapelites and quartzites of the Seridó and Equador formation respectively. The domain is characterized by an E-W trending ductile high strain zones which converge progressively into NE-SW structures at the connection with the Seridó belt to the east (Corsini et al., 1991; Vauchez et al., 1995). Toward eastern there is an increase in the melt volume, with migmatitic gneiss grading to anatectic migmatites near the PSZ-Seridó belt transition, mainly represented by Espinho Branco and Santa Luiza anatexites (Archanjo et al., 2012; Viegas et al., 2013). In the Eastern domain, the trend of the structures acquires a NE-SW strike as a consequence of the convergence of the PSZ with the Campina Grande Shear Zone (Fig. 1a) in an en-echelon array.

Previous studies suggest that nucleation and initial development of PSZ occurred during high-temperature/low-pressure metamorphism accompanied by extensive partial melting with initial strain accommodated by a melt-presence mylonitization (Corsini, 1991; vauchez et al., 1995; Neves et al., 1996; Viegas et al., 2013; Viegas et al., 2014; Cavalcante et al., 2016). U-Pb zircon dating of granites and anatexites emplaced during syntectonic magmatism suggested that the PSZ nucleated at 565 Ma (Viegas et al., 2014). The subsequent mylonitic activity of the PSZ is marked by a widespread solid-state deformation during diachronic evolution with domains recording different exhumation rates and cooling histories. Ar-Ar analysis of the amphibole, muscovite and biotite from deformed rocks of PSZ revealed that the Central domain undergoes a later and slow cooling rate (3-4°C/Myr) and slow uplift rate than the recorded in the Western domain (12°/Ma to 17°/Ma) (Monié et al., 1997; Corsini et al., 1998; Archanjo et al., 2021) between 565 and 500 Ma. This cooling rate contrast is probably due to the greater degree of partial melting and larger volume of hot rocks present in the Central domain (Monié et al., 1997). The later stages of the PSZ are marked by localized shear zones which reworked the

high-grade older units and high-grade mylonites under greenschist-facies, possibly associated to a regional uplift that took place between 545 and 500 Ma in the Borborema Province according to published ^{40}Ar-^{39}Ar and U-PB zircon ages (Monié et al., 1997; Corsini et al., 1998; Hollanda et al., 2010).

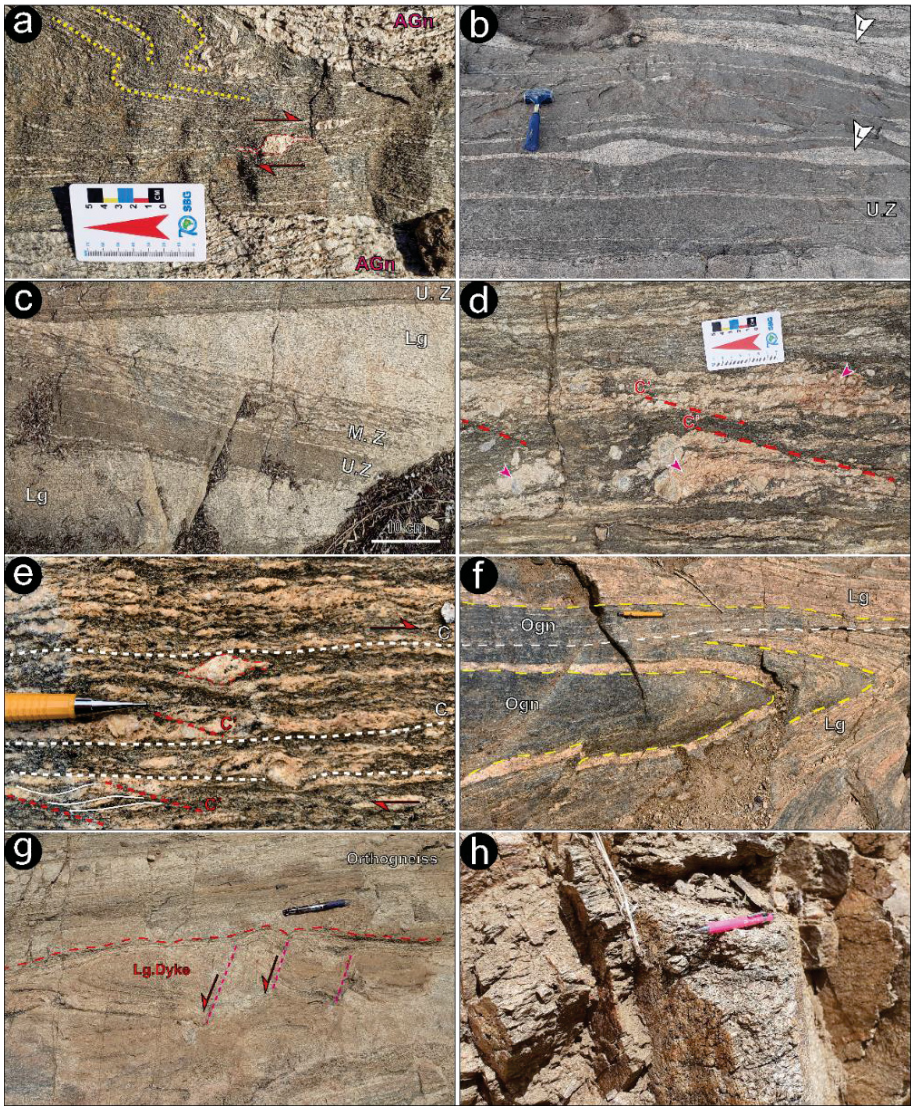

FIGURE 2 - Examples of mesoscale structures of Caicó complex mylonites observed in the Western domain outcrops of PSZ. LMD-12: (a) Folded high-temperature ultramylonite between augen gneiss layers (AGn), with the recrystallized K-feldspar porphyroclasts indicating the dextral sense of shear. The magmatic foliation in the augen gneiss is commonly parallel to the mylonitic foliation; (b) isolated boudins and pinch-and-swell structures of leucosome veins (L) surrounded by a mylonitized Hbl and Bt-rich layer, indicating the rheological contrast between the melt products and the paleosome. LMD-11: (c) Ultramylonitized porphyritic granite dyke cross-cutting leucogranite (Lg) layers (M.Z - mylonite zone; U.Z - ultramylonite zone). LMD-01: (d) Disrupted pegmatitic pods and layers (pink arrow) truncated by C'-type shear bands. The orthogneiss (paleosome) is shown in the upper part of the picture; (e) close picture of mylonitized orthogneiss showing the typical S-C-C' fabric. The highlighted σ-object, defined by a recrystallized K-feldspar porphyroclast indicates a dextral sense of shear. LMD-02: (f) Localized, cm-thick, high-strain zone (highlighted by the dashed white line) truncating the limb of an isoclinal plunging upright fold and transposing the previous contact between the leucogranitic layer (Lg) and the migmatitic orthogneiss (Ogn) (dashed yellow lines); (g) 3 cm thick shear zone localized in the contact between the orthogneiss and the domino-type fragmented leucogranitic dyke (Lg. Dyke). LMD-10: (h) Aspect of L-Tectonite present in the low-temperature mylonitic belt located at the south of the LMD.

5.2.1 Field observations

Seven outcrops studied in the Western domain are constituted of mylonitized diatexites and metatexites of Caicó Complex while four outcrops of the Central domain comprise mylonitized migmatites and orthogneiss, and syn-kinematic anatexites (Espinho Branco anatexite). Asymmetric boudins, sigmoidal structures, σ- and δ-objects (Fig. 2a, e) and asymmetry of intrafolial folds in the outcrops are consistent with the regional dextral shear sense.

5.2.1.1 Western domains lithologies

The outcrops of the Caicó complex in the LMD, near Cajazeiras (outcrops LMD-11, LMD-12, LMD-14 and LMD-15), comprises a few to tens of meters high-strain zones of augen gneiss and diatexites mylonitized at high-temperature. Commonly, less deformed augen gneiss or leucosomes veins of leucogranitic composition occur as boudinaged layers within ultramylonitized dark-grey hornblende-biotite-rich layers (Fig. 2b). Less deformed domains or boudins show evidence of magmatic flow like the presence of preferred alignment of up to a few cm long, elliptical and tabular crystals of K-feldspar (Fig. 2a). In general, the magmatic foliation is parallel to the steeply NNE-dipping mylonitic foliation and the compositional banding of migmatites (Fig. 2a, b). Both sheared leucogranite and leucosome veins and undeformed leucosome cross-cutting the mylonitic foliation and filling shear bands indicate partial melting concomitant to the mylonitization. Some dykes of porphyritic granite cross-cutting less deformed leucogranite layers transition into banded ultramylonites in high-strain zones as indicated by the presence of very coarse-grained recrystallized K-feldspar porphyroclasts (Fig. 2c).

Southward of LMD, near Aurora (outcrops LMD-01 and LMD-02), the melt volume decreases considerably. The outcrops are mainly composed of migmatitic orthogneiss and leucogranitic dykes mylonitized at medium temperatures. The Steeply N- to S-dipping compositional banding comprise leucosome veins and layer-parallel intrusions of leucogranite dykes interlayered with the gneissic banding of paleosome defined by alternating hornblende-biotite-rich and quartzo-feldspathic bands (Fig. 2d-f). Leucogranites or pegmatites dykes also occur occasionally

boudinaged between layers of mylonitized gneiss (Fig. 2g). Furthermore, lens-shaped pods of coarse-grained granites or pegmatites within mylonitic corridors sporadically are found disrupted by C' shear bands (Fig. 2d). The strained orthogneiss is marked by a smooth mylonitic foliation parallel to the gneissic and compositional banding. The mylonitic foliation is characterized by an S-C-C' fabric defined by the alignment of elongated medium-grained biotite flakes and recrystallized feldspar porphyroclasts (Fig. 2e). Biotite flakes and stretched quartz ribbons and porphyroclasts define a lineation that plunges gently to the west. In less deformed zones localized between high strain zones, the migmatitic orthogneiss shows a sub-horizontal compositional banding.

5.2.1.2 Central domains lithologies and the Low-temperature mylonites

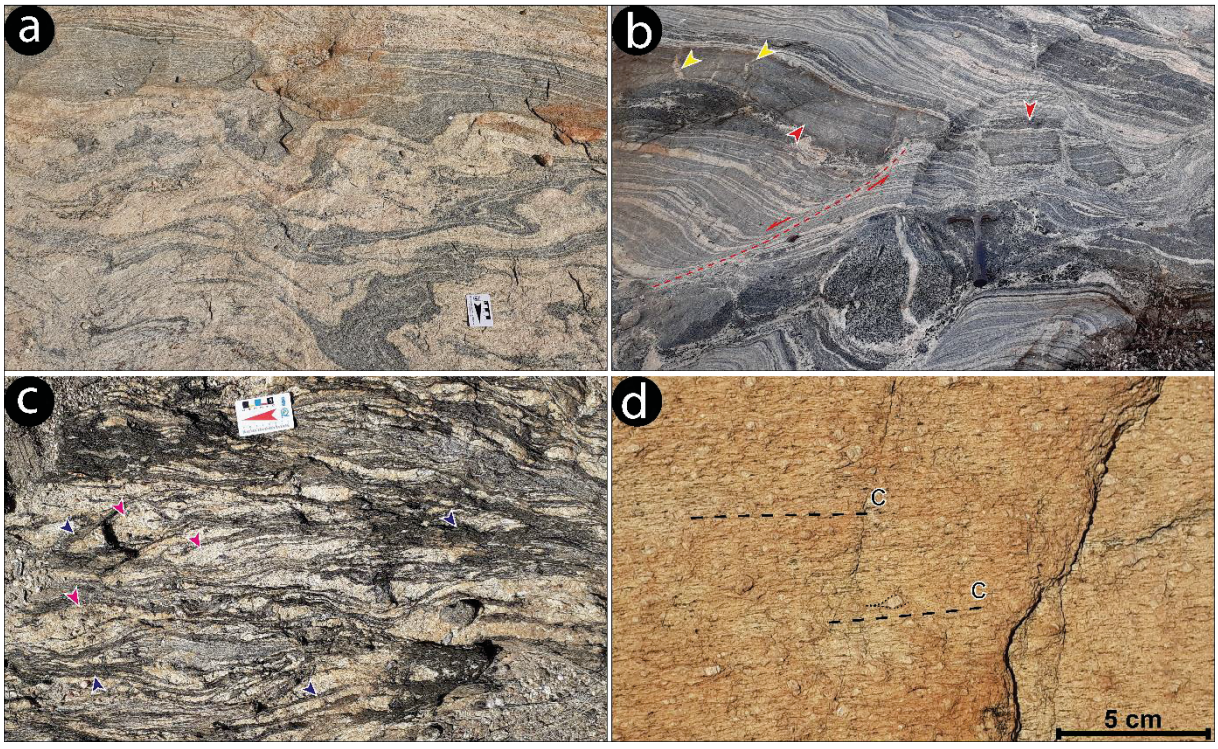

FIGURE 3 - Outcrops structures observed in the Central domain of the PSZ. Espinho Branco outcrops (PSZ-20 and PSZ-21: (a) Schollen diatexite exhibiting complex folding patterns. The preserved paleosome (grey orthogneiss) is shown in the upper part of the photo. (b) Stromatic metatexite characterized by intercalated leucocratic, melanocratic layers as well as bands with intermediate compositions. The yellow arrow indicates the presence of leucosomes in dilational sites in the paleosome (red arrow). The migmatitic banding is found displaced by a mesoscale syn-magmatic shear zone at the left of the photo. PSZ-17: (c) typical coarse-grained S-C mylonite characterized by sheared leucosomes (Q domains, pink arrows) wrapped by the mylonitic foliation (M domains, dark blue arrows) with high content of medium-grained flakes of biotite (so-called transitional mylonites by Viegas et al., 2014). PSZ-18: (d) example of the fined-grained mylonite present in the low-temperature mylonitic belt located at the south of the outcrop PSZ-17. The feldspar porphyroclasts are affected by T-fractures and are found immersed in a quartz-feldspathic matrix.

In the Central domain, the melt volume in migmatites increases significantly compared to the Western domain. The Espinho Branco outcrops (PSZ-20 and PSZ-21) are mainly constituted by deformed stromatic metatexite and schlieren- and schollen-structured diatexites (Fig. 3a-b). The diatexites were mainly deformed under magmatic state and show complex geometries (Fig. 3a) with rare local solid-state overprint (Viegas et al., 2013). Southward from the Espinho Branco anatexite (PSZ-17), the solid-state mylonitization in stromatic metatexites is represented by an increase in mafic phases, an S-C fabric defined by medium-grained biotite flakes and Q-domains constituted by sheared coarse-grained leucosomes defining the so-called transitional mylonites by Viegas et al., (2014) (Fig. 3c).

The two outcrops were studied in the low-temperature shear zone, with one and the other located at the south of Western (LMD-10) and Central domains (PSZ-18), respectively. The Western outcrops comprise low-temperature L-tectonites and the Central outcrops consist of medium-temperature mylonites. Both are cut by several shear fractures. The L-tectonite is characterized by stretched quartz and feldspar grains with the stretching lineation plunging 10-15° to the west (Fig. 2h). The medium-temperature mylonite is characterized by fractured K-feldspar porphyroclasts surrounded by a very fine-grained felsic matrix with biotite films delineating a subvertical C-type shear band (Fig. 3d).

5.2.2 Small-scale Shear Zones

In several outcrops, few mm- to 20 cm-wide subvertical shear zones occur in discontinuities like contacts between layers (see the dashed white line in Figure 2f) or between dykes and the host rock (Fig. 2g). These high strain zones are characterized by an increase in phyllosilicate content and an extreme reduction of grain size in comparison to the surrounding host rock. The shearing material of these minor shear zones appears to fill gaps present in pressure shadows (Fig. 2g).

5.3 METHODS

We studied eight samples representing different temperatures and degrees of deformation (proto to ultramylonites) from two domains of PSZ. Four of these samples were collected in the Western domain and represent a high-temperature

ultramylonite (LMD-12), a boudinaged augen gneiss (LMD-11), and two transitional mylonites which comprise protomylonitized (LMD-01) and mylonitized (LMD-02) migmatitic orthogneisses. Two samples were collected in the Eastern domain, with one representing a deformed anatexite (PSZ-21) and other representing the transitional mylonite (PSZ-17). The samples LMD-10 (Western domain) and PSZ-18 (Central domain) were collected in the low-temperature belt located at the south of PSZ. Supplementary Table 1 summarizes the descriptions of the collected samples.

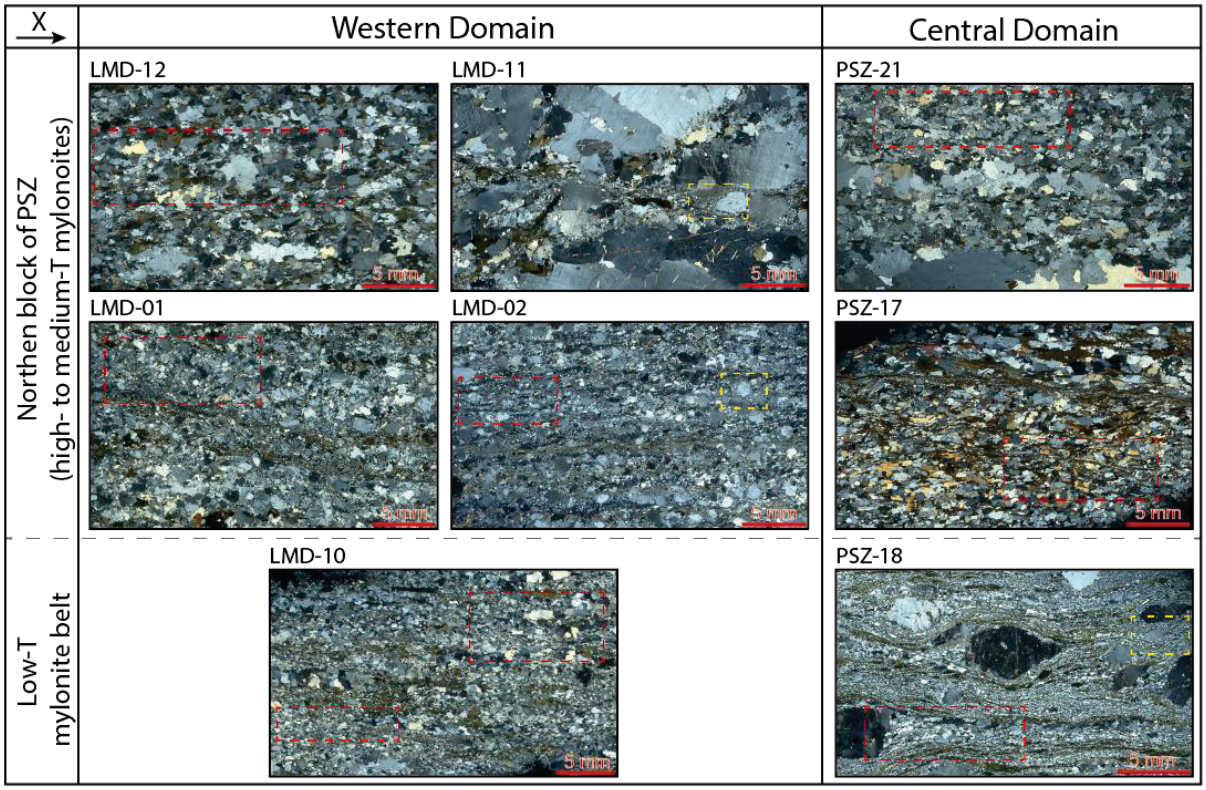

FIGURE 4 - Scanned thin sections (crossed polars) of collected Western and Central domain samples. Red boxes show the large areas analysed in this study. The yellow boxes indicate the regions of the detailed EBSD maps.

We cut the samples parallel to the stretching lineation (shear direction) and perpendicular to the foliation plane (XY plane of the finite strain ellipsoid). To remove the surface relief, the thin section was mechanically polished using diamond paste followed by mechano-chemical polishing using colloidal silica solution to eliminate the surface damage. To mitigate charge problems, the analysed area from all samples were surrounded by copper tape. Before the analysis, the thin sections were described using an optical microscope. Backscattered electron (BSE) images were collected to study morphology and spatial arrangement of mineral phases in the very fine-grained domains. The BSE images were acquired using a Thermo-FEI Quanta

FEGSEM 450 at the Federal University of Paraná using an accelerating voltage of 10 kV under high-vacuum conditions. EBSD analysis was carried out using a FEG-SEM Mira3 LM, equipped with an EBSD detector from Oxford instruments Nordlys, and Aztec EBSD acquisition software at the Structure and Material Laboratory at the LACTEC institute (Curitiba, Brazil). The analysis was performed using 20 kV accelerating voltage, 74 µA beam current and 25 mm of working distance. The large-area maps were obtained moving the beam on a grid with a fixed step size of 10 µm or greater (15-20 µm) for coarse-grained rocks while for detailed maps were used 2-4 µm of step size.

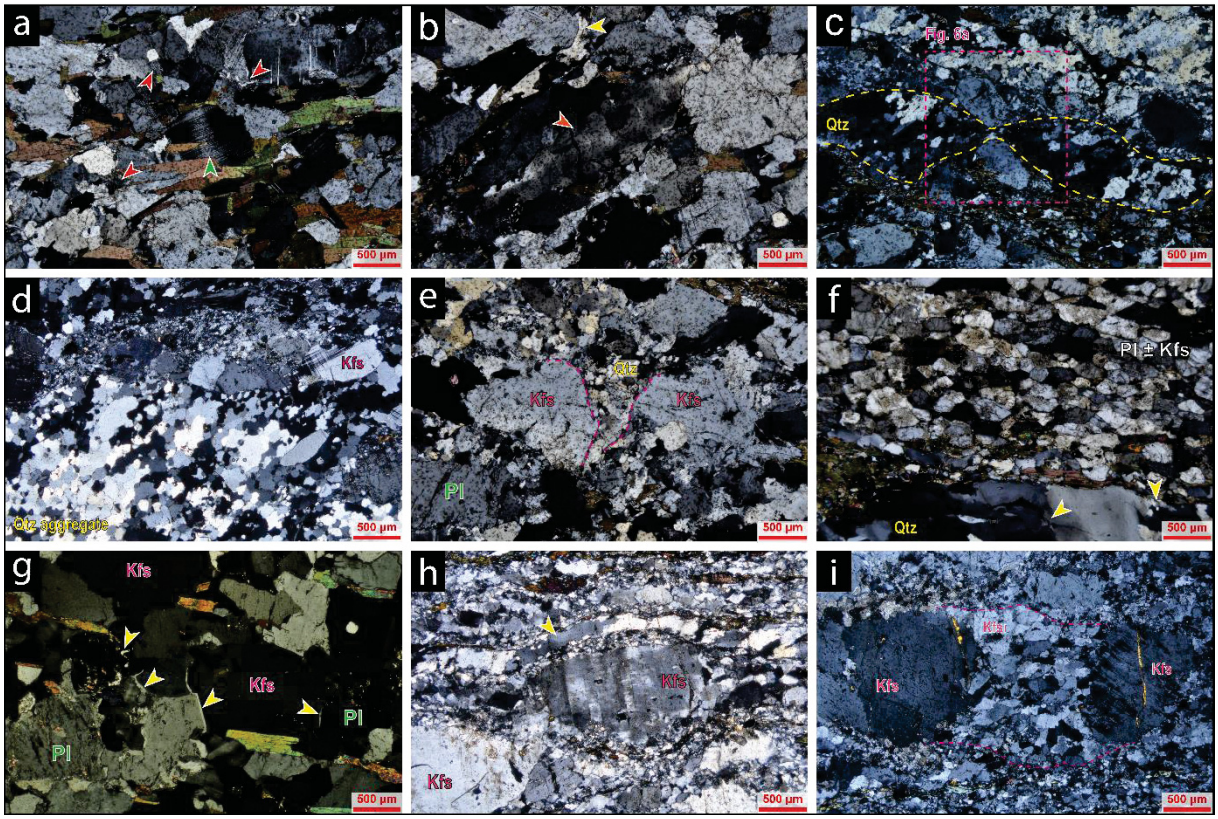

FIGURE 5 - Optical photomicrographs of the typical microstructures and fabrics observed in the Western (a-f) and Central (g-i) domains. High-temperature mylonite fabric (LMD-12): (a) plagioclase with bent twins (green arrow) and myrmekite structure in the framework interstices (red arrow); (b) quartz grain with chessboard extinction (red arrow) and quartz filling the framework interstices (yellow arrow). Transitional mylonites (LMD-11, LMD-01 and LMD-02): (c) Boudinaged ribbon (highlighted by the yellow dashed line) with oblique foliation. The BSE image of the orange box area is shown in Fig. 7a; (d) quartz aggregate with ameboid-shaped grains and (e) quartz grains filling an open fracture between K-feldspar porphyroclasts. (f) Aspect of the two microstructural domains (feldspar aggregate and quartz ribbon) which characterized the low-temperature sample (LMD-10). Note the presence of very fine recrystallized quartz grains indicated by the yellow arrow. (g) Quartz films (yellow arrows) between feldspar grains in the deformed anatexite (PSZ-21). Microstructures observed in the PSZ-18 sample: (h) K-feldspar porphyroclasts with tensile fractures wrapped by quartz ribbons (yellow arrow) and a fine-grained feldspathic matrix; (i) extension fracture filled by precipitated K-feldspar grains with the long axis perpendicular to the fracture walls.

The EBSD data were processed using MTEX toolbox 5.7.0 for MATLAB (Bachman et al., 2010) which was used to generate the orientation maps, pole figures (PF), inverse pole figures (IPF) and the misorientation profiles. The denoising routine of the EBSD raw data comprised the elimination of wild pikes, inaccurate orientation measurements (pixels with a high mean angular deviation) and grains with size ≤ 2 or 3 indexed pixels which were interpreted as grains constructed from points with a wrong solution (Cross et al., 2017). During grain reconstruction, we state misorientation angles ≥ 10° as grains boundaries and from 2 to 10° as subgrain boundaries. The one point per grain pole figures and inverse pole figures were plotted in the upper hemisphere equal-area projection. The structural coordinate of the pole figures is established with X-axis being parallel to the stretching lineation and Z-axis normal to the foliation plane. Misorientation angle distributions (M.A.D) for quartz and feldspar was represented in frequency histograms for correlated (blue bars) and uncorrelated (red bars) point pairs with a curve (orange line) representing the theoretically random distributions. Also, to evaluate quantitatively the fabric strength for quartz and feldspar in the microdomains we used M-index (Random 0 to single crystal fabric 1; Skemer et al., 2005) using a computational method implemented in MTEX (Mainprince et al., 2015). The mineral abbreviations of this study follow Whitney and Evans (2010).

5.4 RESULTS

5.4.1 Sample microstructures

5.4.1.1 Western domain mylonites

The mylonites in the Western domain are composed of variable amounts of quartz (13-39%), K-feldspar (6-48%), plagioclase (28-57%), biotite (1-18%) and hornblende (0-5%). The high-temperature mylonite sample (LMD-12) consists of alternating medium-grained polyphase matrix and coarse-grained quartzo-feldspathic bands (Fig. 4) with elongated perthitic K-feldspar and plagioclase grains. The grains boundaries are generally sutured, diffuse or lobated. The quartz and feldspar show microstructures indicative of crystal-plastic deformation (Fig. 5a, supplementary Table 1). Quartz grains are not significantly affected by dynamic recrystallization, but

exhibit chessboard extinction (Fig. 5b). Flame perthite and myrmekite are commonly observed (Fig. 5a, b), but the myrmekite does not show any preferred site of nucleation. Aligned biotite flakes define the foliation and pinning the framework grains. Melt-related microstructures like quartz films (Fig. 5b) or as small drop-like inclusions in feldspar grains are present. Similar microstructures were observed in less deformed areas of the protomylonitized augen gneiss (LMD-11).

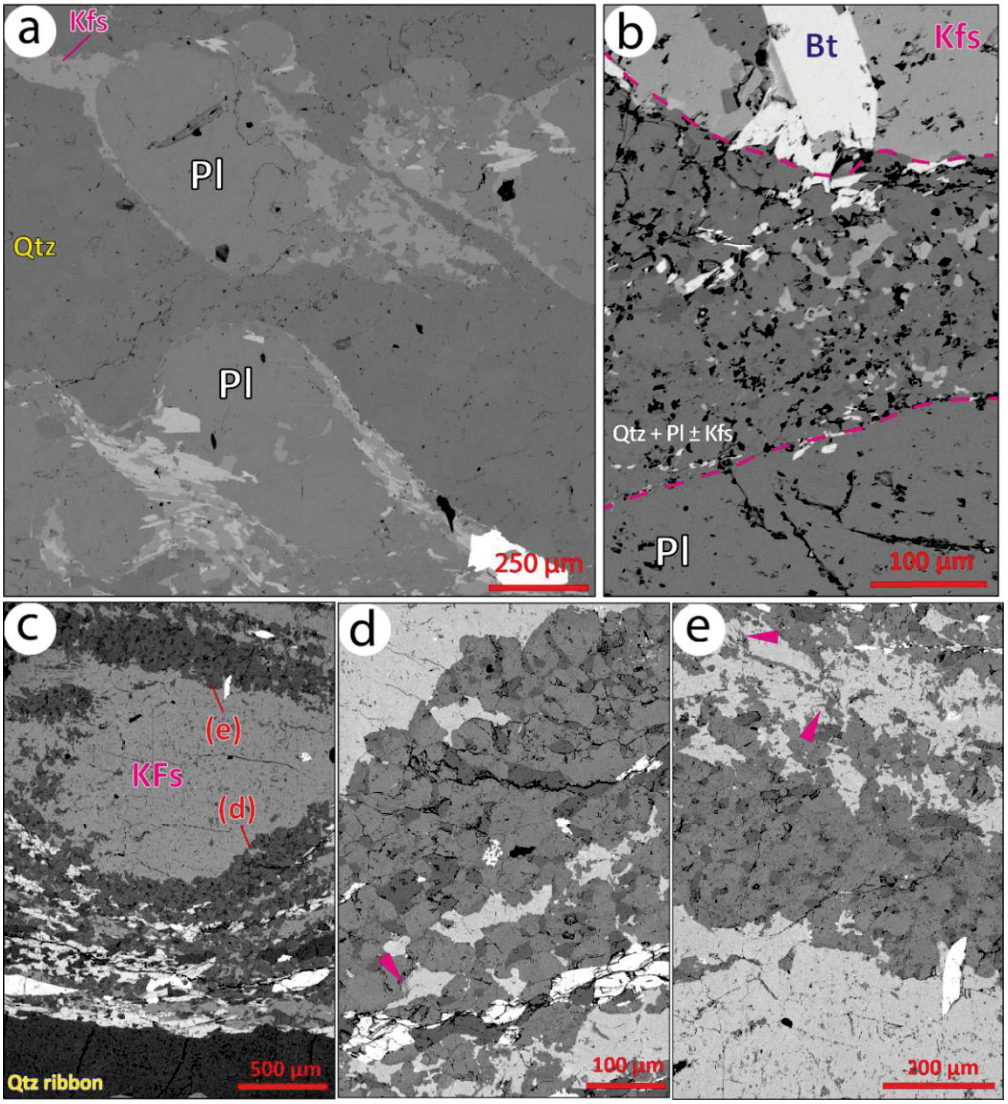

FIGURE 6 - BSE images of the transitional mylonites. (a) Tails and rims of recrystallized K-feldspar (light grey) around elliptical plagioclase porphyroclasts (grey). Quartz ribbons (dark grey) impinged by Pl porphyroclasts define a boudin-like structure (LMD-01). (b) Recrystallized aggregate between K-feldspar (top) and plagioclase (bottom) porphyroclasts. Note the presence of diamond-shaped quartz and irregular Kfs between triple junctions and filling the interstices (LMD-11). c) Kfs porphyroclasts surrounded by a rim of myrmekite immersed in a polyphase (Pl + Qtz + Kfs + Hbl) matrix (PSZ-18). (d) and (e) are the detailed regions indicated in (c) showing the transition of the myrmekite structure to the polyphase matrix. Note the presence of non-oriented flame perthites (pink arrows) in K-feldspar grains with a dissected aspect and the interstices and triple points filled by K-feldspar and quartz in the matrix.

The quartz in the samples LMD-01 and LMD-02, and along S-C surfaces of the sample LMD-11 occurs as polymineralic ribbons and/or as irregular aggregates. Figure 9 show that the size of quartz grains decreases from the samples with relict quartz grains (LMD-12) or quartz aggregates (LMD-01) to samples dominated by quartz ribbons (LMD-02 and LMD-11). The quartz in aggregates have ameboid shapes with lobated boundaries (Fig. 5d), display widespread polygonal subgrains and microstructures like left-over grains and dissected grains. In contrast, the quartz ribbons display equigranular moderately elongated grains defining oblique foliations and occasionally occur as boudin-like structures (Fig. 5c). The feldspar porphyroclasts are elliptical or square-shaped and display low aspect ratios (Fig. 5a and 15c). They occur commonly fragmented and exhibit intracrystalline deformation microstructures (see supplementary Table 1). The size of porphyroclasts is variable depending on the protolith, ranging from centimetric clasts in the case of augen gneiss (LMD-11) to millimetric porphyroclasts (~0.25-0.28 mm of average) in the mylonitic orthogneiss (LMD-01 and LMD-02). In all samples, the K-feldspar porphyroclasts display flame perthites and are surrounded by myrmekite rims along the high normal stress borders (e.g., normal to the instantaneous shortening axis, Figures 14c-f). High normal stress sites in plagioclase porphyroclasts instead show concentrations of very fine recrystallized plagioclase grains (Fig. 14c, d). Sites of low-stress concentration like strain shadows or pull-apart structures are preferentially filled either by K-feldspar or rarely by quartz (Fig. 5e). The fine-grained polyphase matrix increases in proportion from LMD-11, LMD-01 to LMD-02. Detailed descriptions of the matrix are given in section 5.4.3.4. Biotite away from shear bands occurs as preferred aligned medium-grained flakes.

The low-temperature L-tectonite (LMD-10) display quartz ribbons with grains coarser than the transitional mylonites (Fig. 9). The grain boundaries are serrated and very fine-grained quartz occur between the contacts of the larger crystals (Fig. 5h). Intracrystalline plastic features like undulose extinction and deformation bands are common and indicate an opposite shear sense regarding the regional dextral shear sense. Transgranular and intragranular fractures are often observed in ribbons. The feldspar occurs as aggregates characterized by strain-free grains with a preferential alignment of their long axis. Preferred elongation of feldspar grains constitutes an oblique foliation consistent with a sinistral shear sense (Fig. 5h). Rare K-feldspar grains are elongated and extensively cut by fractures.

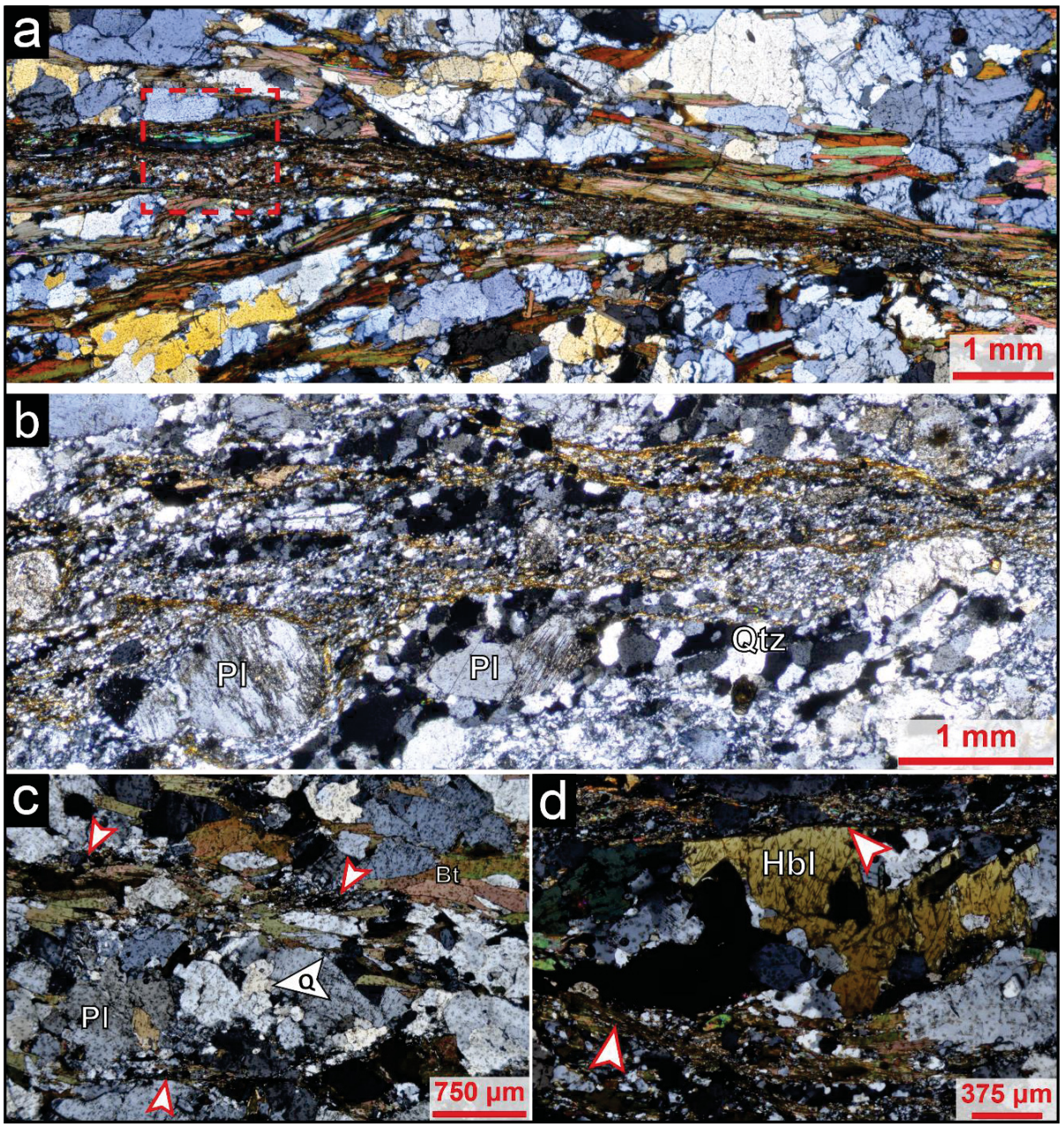

Figure 7 - Photomicrographs of micro-shear zones present in the samples PSZ-17 (a), LMD-02 (b) and the shear bands (white arrows) in the samples LMD-12 (c) and LMD-01 (d). The BSE image indicated by the red box in (a) is shown in Fig. 8a. Note the anastomosing character of the interconnected phyllosilicate-rich layers wrapping quartz-feldspar domains, the further grain size reduction and the increase in the content of very fine-grained phyllosilicate in comparison to the surrounding rock.

5.4.1.2 Central domain mylonites

The deformed anatexite (PSZ-21) comprises coarse-grained quartz-feldspar bands and equigranular medium-grained biotite-bearing bands (Fig. 4). The quartz occurs as anhedral larger grains with straight to slightly lobate boundaries and occasionally show intracrystalline microstructures. The quartz also occurs as rounded

grains, filling the interstices or triple junctions in the feldspar framework and as drop-like inclusions in feldspar (Fig. 5g). In general feldspar grains are strain free, but occasionally some K-feldspar grains show flame perthites. Myrmekite are widespread in the sample and do not show any preferred sites of nucleation.

The transitional mylonite (PSZ-17) is characterized by equigranular, moderately-elongated medium-grained anhedral plagioclase and quartz grains with relatively high aspect ratios (2.28 and 1.85 of average respectively) (Fig. 4). The grains display straight to lobate boundaries and are extensively cut by intragranular fractures, mainly in the crystal corners and both show intracrystalline plasticity features. The feldspar grains show little intracrystalline plastic features. Preferred aligned medium-grained biotite flakes define the S-C' fabric of the sample.

The low-temperature mylonite PSZ-18 is characterized by subelliptical and tabular K-feldspar porphyroclasts with tails of recrystallized Kfs immersed in a banded matrix composed of continuous quartz ribbons and polymineralic aggregates with variable amounts of quartz, K-feldspar, plagioclase, hornblende and subordinate biotite. High normal stress borders of porphyroclasts display myrmekite rims (Fig. 6c) which transition into quartzo-plagioclase aggregates (Figs. 6d and e). In these aggregates, in general, the framework is defined by equant grains of plagioclase with rounded quartz present in triple junctions and K-feldspar occurring either as very irregular relict grains which show flame perthites with albitic lamellae (see pink arrows in Figs. 6d and e) or as rare grains filling the interstices. The dissected-shaped Kfs are derived from the desegregation of recrystallized tails. The Kfs porphyroclasts occasionally exhibit intracrystalline microstructures like deformation bands and subgrains, and are commonly cut by fractures (Fig. 5h). Open fractures are filled by K-feldspar (Fig. 5i) and rarely by quartz. Very fine-grained hornblende and subordinate biotite forms interconnected narrow layers which envelopes the porphyroclasts and delineate the C-C'-type shear bands of the sample. The descriptions of the samples are also summarized in the supplementary Table 1.

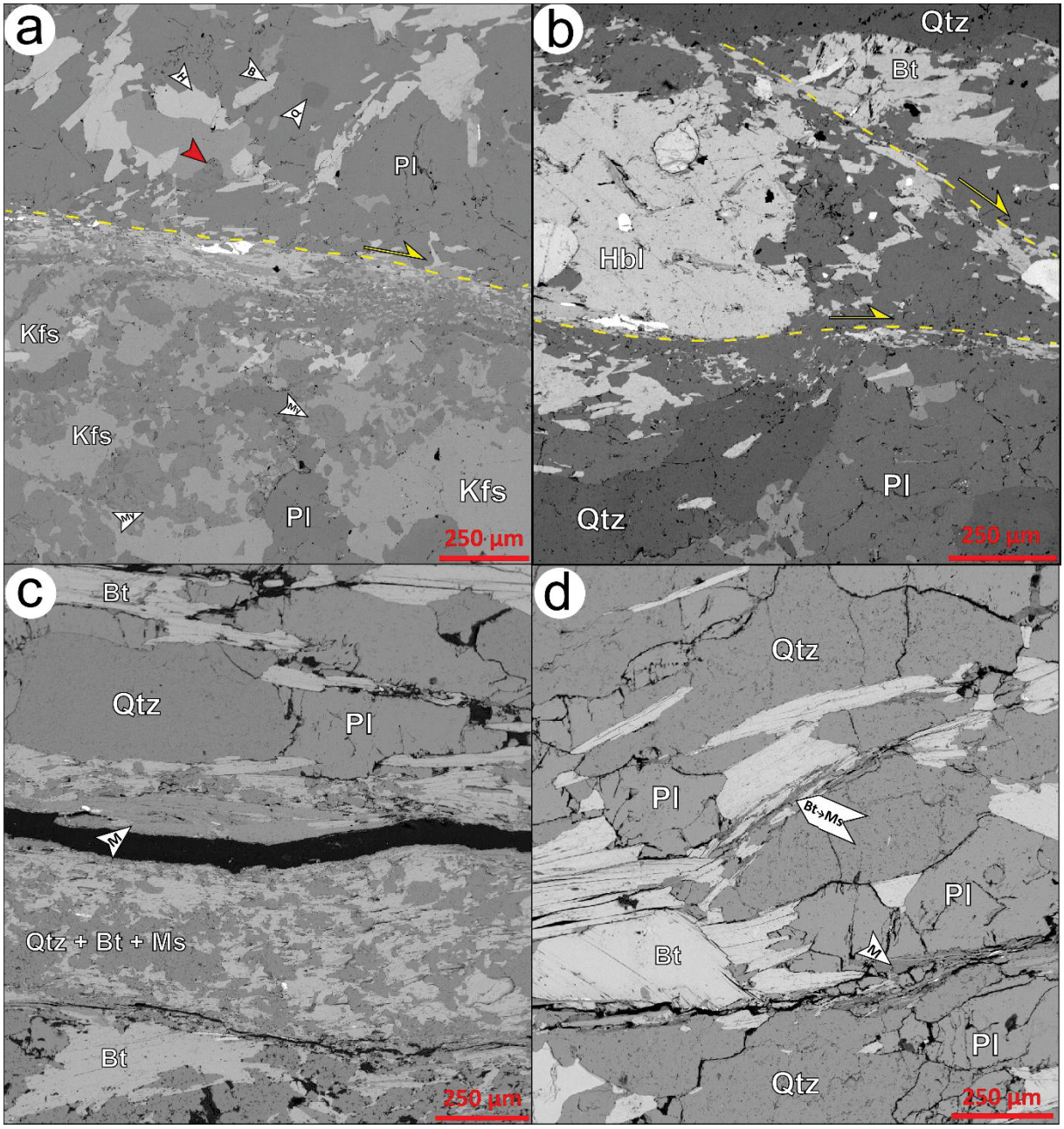

FIGURE 8 - BSE images of the micro-shear zones and shear bands. LMD-01: (a) and (b) show shear bands cross-cutting the protomylonitic fabric. Note the further grain-size reduction, phase mixing and the lack of alteration of biotite. Myrmekite structure is indicated by the red arrow. c) Mature low-temperature shear zone characterized by grain size-reduction and phase mixing between the new (muscovite - Ms) and old phases (Bt + Qtz). d) Alteration of biotite to muscovite (M) in an immature micro shear zone developed along the transgranular fractures. Note the preferential trace of fracture and minor cataclasis throughout the interphase boundaries.

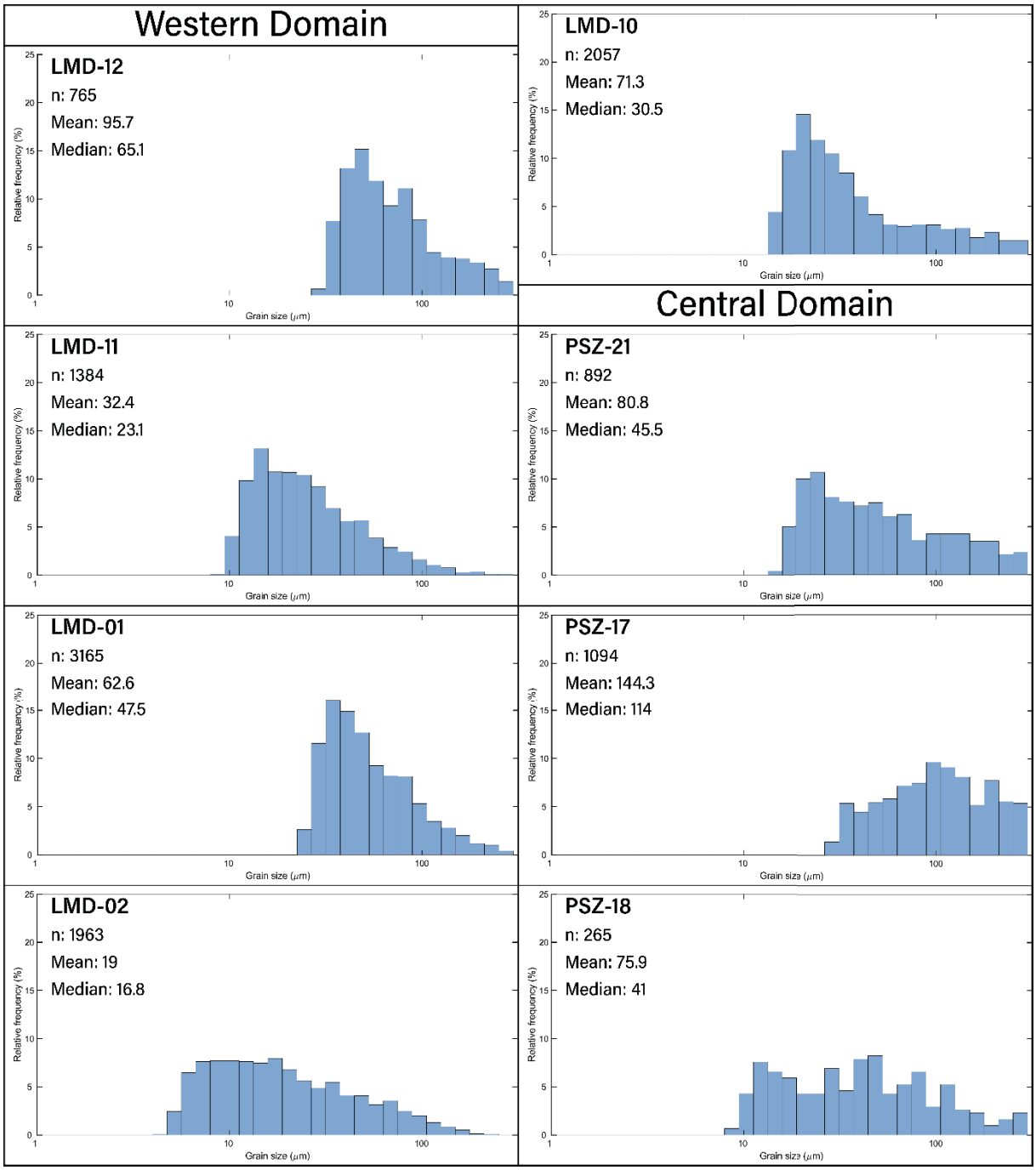

FIGURE 9 - Grain size distribution for quartz in the studied samples.

5.4.2 Micro-scale shear zones and shear bands

The mylonitic fabric of some medium- to high-temperature mylonites are cut by micro-scale shear zones or shear bands characterized by an anastomosed network of interconnected layers of phyllosilicates wrapping around fine-grained quartzo-feldspathic domains or porphyroclasts (Fig. 7a-d) and occur preferentially along rock discontinuities like contacts between (Fig. 7b) layers of different

compositions or grain sizes (Fig.7a and b). The sizes of grains in these high strain zones are smaller than the surrounding rock (Fig. 8a and c) and BSE images show that there is considerable mixing of phases (Fig. 8c). Figures 7c and 8d show that possible precursors of these micro shear zones are transgranular fractures preferentially localized along interphase boundaries. Local microcracking in the grain corners and alteration of minerals like biotite and feldspar to low-temperature minerals like muscovite (Fig. 8d) or white mica are commonly observed along these fractures. Phyllosilicates also align to form interconnected layers. On the other hand, significant mineral alteration is not observed in the shear bands. Kinematic indicators as σ-objects and deflection of mylonitic fabric suggest that these micro-shear zones maintain the same shear sense as the host rock (Fig. 8a and d).

5.4.3 Textural Analysis

5.4.3.1 Quartz CPO

The quartz pole figures and inverse pole figures for the Western and Central domains samples are shown in Figures 10a and 10b.

5.4.3.1.1 Western domain samples

The sample LMD-12 display a weak poorly defined [c]-axis pattern similar to an asymmetric type-I cross-girdle consistent with dextral shear sense. The Inverse pole figure (IPF) reveals the clustering of negative {z} rhombs around the Z-axis, which suggests the activation of the easy slip system negative rhomb<a>. [c]-maximum near lineation also is consistent with the activation of prism-[c] easy slip system. On the other hand, the quartz pole figure for the sample LMD-01 displays a stronger CPO with c-axis maximum spreading from near Y-axis to normal to the foliation and <a>-axes maximum parallel to the stretching lineation which is indicative of the activation of easy slip on the planes basal, prism and rhomb on the direction <a>. The CPO of LMD-11 and LMD-02 display a quite similar strong CPO, characterized by [c]-axis maximum centred on the Y-axis, with a slight spread into intermediates positions. The <a>-axes form maxima near or gently inclined clockwise ~10° from the lineation. The pattern is also clear in the IPFs, with Z-axis and X-axis

clustering around directions which corresponds to the {m}(0001) and <a><-12-10>axes respectively. This pattern is indicative of dominant easy slip system prism<a> and minor rhomb<a>. The asymmetry is consistent with the regional and local dextral shear sense. The m-index show a strengthening of CPO from the sample LMD-12 (0.008) to LMD-11 (0.16) and from the sample LMD-01 (0.14) to LMD-02 (0.2) consistent with the development of high-strained quartz ribbons from quartz aggregates or relict grains. In contrast, the sample LMD-10 (Low-temperature mylonite) show a strong (M-index = 0.099) asymmetric incomplete crossed-girdle with [c]-axis maximum localized near the centre and in the upper half of the pole figure and two <a>-axes maximum inclined counter-clockwise at ~30° with respect to the lineation. This indicates the activation of the dominant slip system rhomb-<a>, prism-<a> and minor basal-<a>. The asymmetry of the pattern indicates a local sinistral shear sense, consistent with the sense observed in deformation bands.

5.4.3.1.2 Central domain samples

The quartz CPO for the Central domain samples show a clear strengthening of fabric from the deformed anatexite (PSZ-21) to the low-temperature mylonite (PSZ-18). While the deformed anatexite (PSZ-21) show no clear CPO pattern and a weak fabric (m-index = 0.0058) the transitional mylonite shows a relatively stronger CPO (m-index = 0.0344) with a pattern similar to a slightly asymmetric type-I crossed girdle with [c]-axis maxima around Y-axis indicating dominant easy slip on the dominant prism-<a> and minor rhomb- and basal-<a> systems. The CPO strength of the sample PSZ-18 increased considerably compared to the other samples (m-index = 0.2). The c-axis display maxima centred on the y-axis and at intermediate positions. The Inverse pole figure shows that the poles to negative rhombs have a maximum normal to the foliation. This pattern is consistent with slip on the dominant prism-<a> and minor rhomb-<a> systems.

5.4.3.2 Quartz misorientation and slip system analysis

To evaluate the slip system responsible for the development of subgrains and the new recrystallized grains, we plot the misorientation axis that corresponds to low-angle boundaries relative to the crystal and specimen coordinate system

(Figures 11a). For the subgrain analysis, we considered only low misorientation angles ranging between 2-9° and 9-15°, since the first interval comprising “true subgrain boundaries” prior to the transition to grain boundaries which is suggested to occur in the second-mentioned interval (Kilian et al., 2017; Shigematsu et al., 2006).

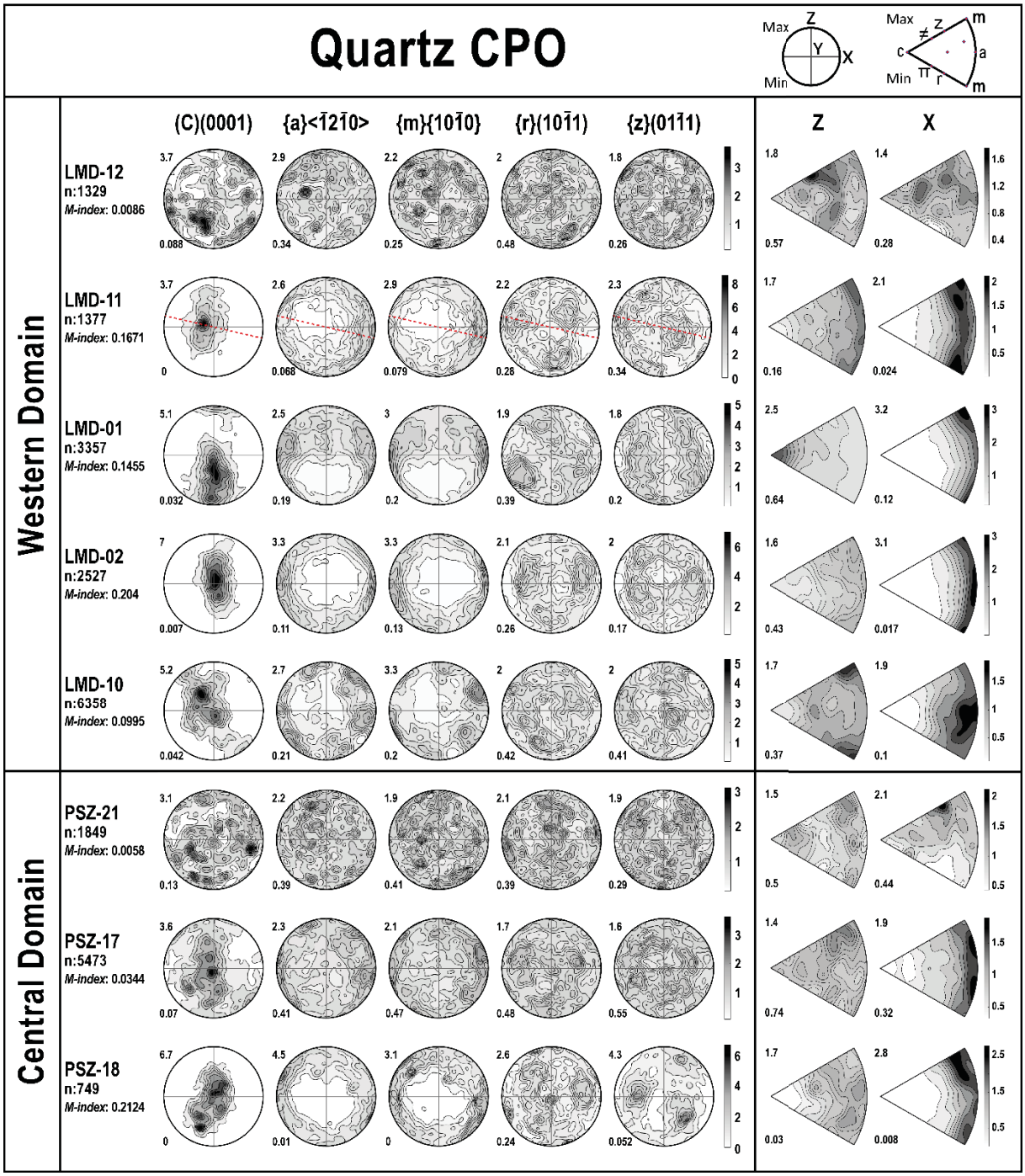

FIGURE 10 - Quartz texture of Patos mylonites displayed as (a) contoured pole figures for (c)(0001), <a><10-10>, {m}{01-10}, {r}{10-11} and {z}{01-11} axes and as (b) inverse pole figures. The pole figures are plotted with respect to the directions normal to the shear plane (Z-axis) and parallel to the stretching lineation (X-axis). For the sample LMD-11, we plotted the trace of the local shear plane (red dashed line). Fabric strength is indicated by the M-index. The number of grains is referred to as n.

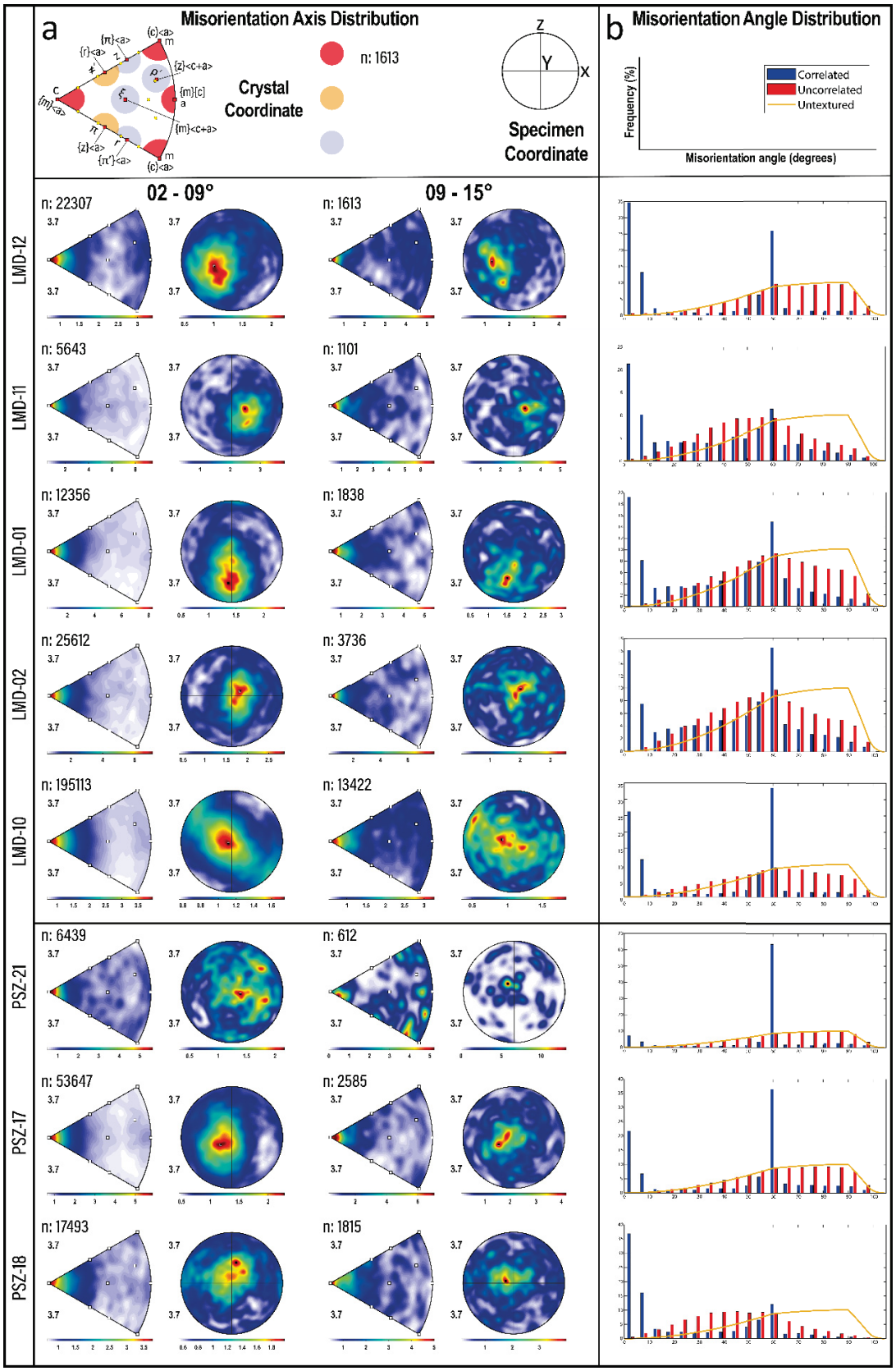

FIGURE 11 - Misorientation analysis of the quartz in the studied samples: (a) Misorientation axes plotted in crystal and specimen coordinates for angles comprising subgrains boundaries (2-9°) and the transition to grain boundaries (9-15°). The inverse pole figure at the top shows the crystallographic directions and the rotation axes associated with the quartz slip systems (modified from Neuman et al., 2000). b) Misorientation angle distribution (MAD) histograms for quartz showing the correlated (blue bars) and uncorrelated (red bars) pairs and the theoretical random distribution (orange line).

All samples display misorientation axis clustering close to the [c]-axis in crystal coordinates which indicate a great contribution of {m}<a> slip system to subgrain formation. The maximum is stronger for the samples with [c]-maximum centred on the Y-axis. The samples LMD-12 and PSZ-21 also show a minor concentration around the <a>-axis which corresponds to the {m}[c] slip system and is consistent with the high-temperature deformation undergone by the samples. Significative clustering around other directions that are equivalent to basal- and rhomb-<a> slip systems was not observed. The misorientation axis plotted with respect to the specimen coordinate system show that most of the axes are located at or near the Y-axis, indicating the predominance of tilt boundaries. The IPFs for the misorientation axis of boundaries with 9-15° of misorientation angle still show a maximum centred on the [c]-axis but also display several minor clustering around other axes like <z>, <m>, <π> and <r> axes which indicate a contribution of other slip systems (see legend in Fig. 11) during the subgrain-grain transition.

The misorientation angles distribution (MAD) for quartz grains illustrated in Figure 11b show a high frequency of correlated low-angle boundaries (<10°) in all samples, except for PSZ-21. A peak at 60° corresponding to the dauphiné twin is also observed in all histograms and is remarkably high in the sample PSZ-21. The samples LMD-11, LMD-02, LMD-01 and PSZ-18 also show a high frequency of correlated and uncorrelated misorientation angles ranging from 2° to 35-60°. The histograms for central domain samples show that there is an increase in the frequency of low-angle boundaries from the highest-temperature sample (PSZ-21) to the lowest (PSZ18).

5.4.3.3 Feldspar CPO

Figure 12 and 13 shows the poles figures for feldspar of Western and Central domain mylonites respectively. The Kfs pole figures for samples with negligible amounts of K-feldspar grains (<5%) in the analysed areas were not represented. For the feldspar pole figures of samples LMD-01, LMD-02 and LMD-11 we plotted the uncountored poles of porphyroclasts color-coded according to the grain orientation spread (GOS) and the contoured bulk poles figures for comparison. For these samples, pole figures with other axes are shown in Supplementary figure S1.

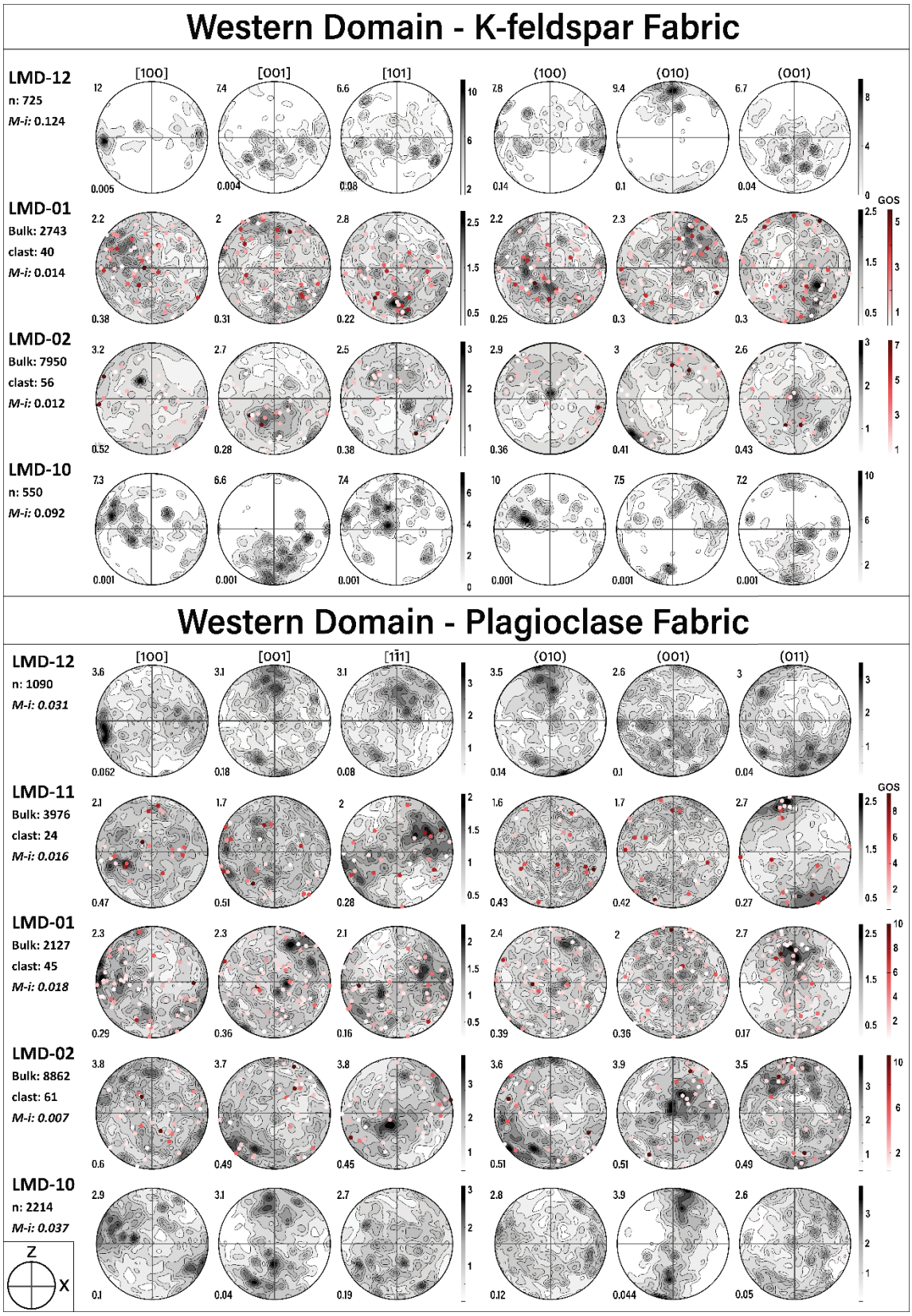

FIGURE 12 - Crystallographic preferred orientation of feldspar from Western domain samples displayed as countered, equal area, upper hemisphere, pole figures. The common planes and directions associated with the slip system for monoclinic K-feldspar (2/m) and triclinic plagioclase (C-1) are plotted. For the samples LMD-11, LMD-01 and LMD-02 were plotted the matrix grains (contoured) and the poles of feldspar porphyroclast coloured according to the grain orientation spread (GOS). Fabric strength is indicated by the M-index. The symbol n is the number of grains.

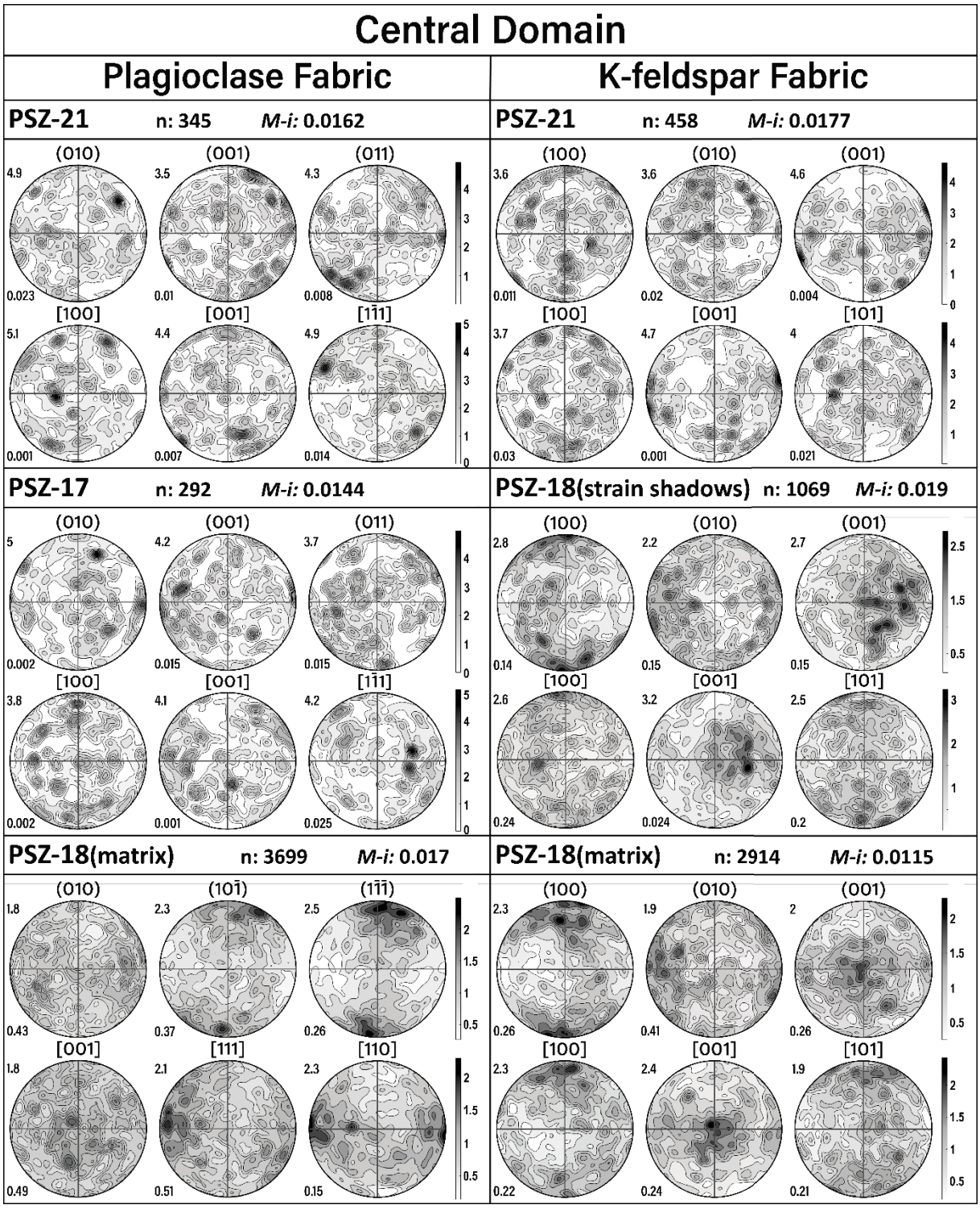

FIGURE 13 - Crystallographic preferred orientation of feldspar from Central domain samples displayed as countered, equal area, upper hemisphere, pole figures. For the sample PSZ-18, we show the poles figures for K-feldspar present in a very high aspect ratio (15:1) strain shadow (ribbons, see the red dashed box of sample PSZ-18 in Fig. 4) and in the matrix.

5.4.3.3.1 Western domain

The K-feldspar CPO of high-temperature mylonite displays a strong peripheric single maximum (m-index = 0.12) of (010) plane normal to the foliation and [100] axis maxima parallel to stretching lineation, consistent with the easy slip system (010)[100]. The transitional mylonites show a weakening of the bulk CPO as the recrystallized matrix increases in proportion (M-index of 0.014 and 0.012). Both samples display a poorly defined concentration of poles to (010) planes of porphyroclasts near the periphery, rotated 30° from the Z-axis and a poor concentration of [100] axis in the left periphery of pole figure which argues for the activation of the easy slip system (010)[100]. The asymmetry is also consistent with the dextral shear sense. The lighter colours of the poles indicate that most of the porphyroclasts display low internal lattice distortion. The similarity between the bulk and porphyroclasts CPO indicates some degree of porphyroclast control on the orientation of the new recrystallized grains. A similar CPO pattern is observed in the sample LMD-10 with (001) plane peripheral maximum near Z-axis and the (010) and [010] axes showing peripheral maxima rotated clockwise (~20°) relative to the Z- and X-axis respectively. This may indicate slip on the (001) and (010) planes in the direction [100], however, the CPO asymmetry is inconsistent with the local shear sense of the sample indicated by the quartz CPO and microstructures.

The plagioclase pole figure for the sample LMD-12 display a relatively strong CPO (M-index = 0.031) with a (010) plane maximum normal to the foliation and [010] direction maximum parallel to the lineation consistent with the easy slip system (010)[100]. A weakening in CPO strength is also observed as the proportion of recrystallized grains increase (See M-index in Fig. 12). The plagioclase CPO for the bulk rock and porphyroclasts of the samples LMD-11, LMD-01 and LMD-02 display (011) and (021) planes with maxima nearly normal to the foliation with the [1-11] and [1-12] axis widely distributed along a great circle rotated ~20° counter-clockwise from the X-axis which suggests the activation of the easy slip systems (011)[1-11] and (021)[1-12]. The asymmetry shown by the CPO argue for a sinistral shear sense, however, the IPF show the Z- and X-axis clustering around the (011) and (021) planes and [1-11] and [1-12] directions which indicate that most of the grains are in “soft” orientations for easy slip on these systems. The bulk CPO for the samples LMD-01 band LMD-02 also show [100] axis maxima nearly parallel to the lineation

and peripheral concentrations of poles to (010) plane rotated ~30° from Z-axis occur in the sample LMD-02, which is consistent with the easy slip on the systems (011)[100] and possibly (010)[100]. In contrast, the porphyroclasts in these samples are in “hard” orientations for slip on the (010)[100] system. The low-temperature mylonite (LMD-10) show a slightly strengthening of CPO (m-index = 0.03) which is characterized by a well-defined (001) plane single girdle rotated ~13° from the Z-axis and perpendicular to the orientation of the long axis of grains. (010) and [100] axes show peripheral maxima inclined ~14-20° from X-axis, parallel to the grains long axis. This could indicate the slip on the (001) plane in the [010] and [100] directions but this is inconsistent with the shear sense of the sample.

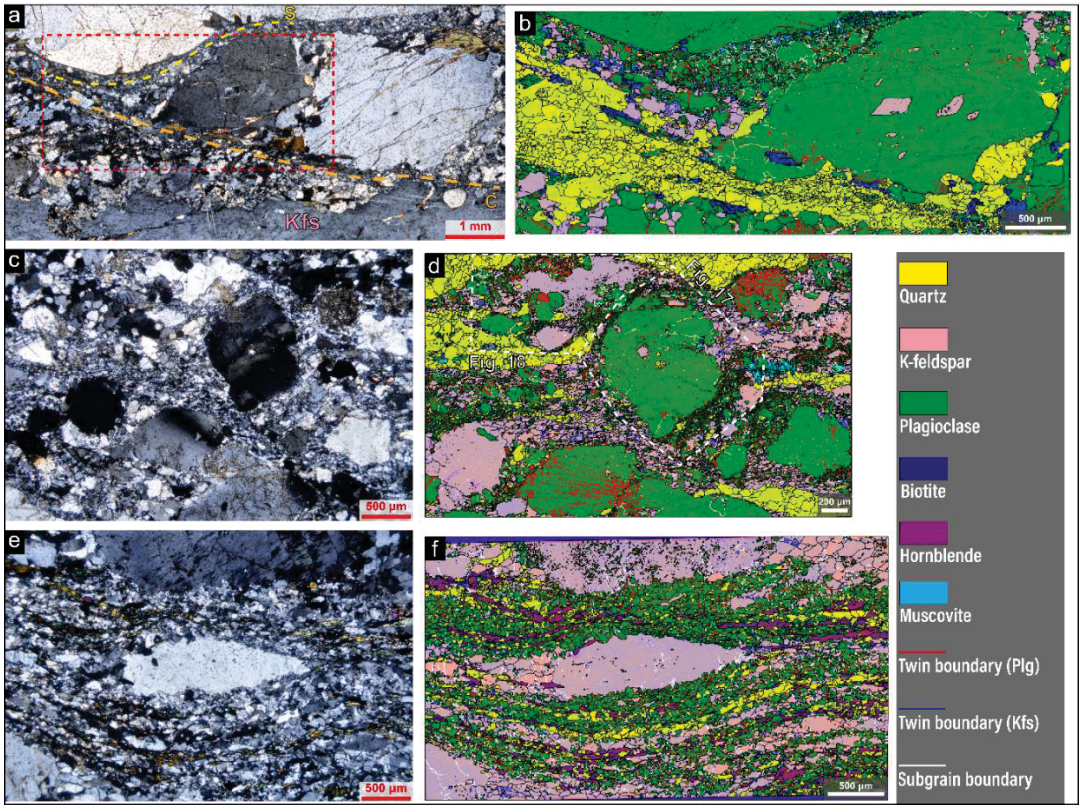

Figure 14 - Optical photomicrographs and the correspondent EBSD maps of the areas of the samples LMD-11 (a-b), LMD-02 (c-d) and PSZ-18 (e-f) analysed in detail (see the yellow dashed boxes in Fig. 4). The grain boundaries (black lines), subgrains boundaries (white lines) and twin boundaries for K-feldspar (blue lines) and plagioclase (red lines) are indicated.

5.4.3.3.2 Central domain

The deformed anatexite (PSZ-21) displays a very weak CPO (M-Index = 0.017) with a very poor clustering of (010) roughly normal to the foliation and a peripheral clustering of [001] directions parallel to the lineation, which may indicate

the slip system (010)[001]. The Kfs CPO of ribbons and matrix of sample PSZ-18 are similar, characterized by the (100) and [010] axes maxima normal and parallel to the mylonitic foliation respectively, consistent with the easy slip system (100)[010]. The CPO is stronger for the Kfs precipitated in strain shadows (M-index = 0.019) than the present in the matrix (M-index = 0.011).

Both sample PSZ-21 and PSZ-17 display very weak CPO (M-index = 0.014-0.016) with no clear pattern. On the other hand, the pole figure for the Qtz-Pl aggregate of the sample PSZ-18 shows a slightly strengthening of CPO (m-index = 0.017 with the (10-1) and (1-1-1) planes maxima normal to the mylonitic foliation and the [111] and [110] directions maxima parallel to the lineation, consistent with the easy slip system (10-1)[111] and (1-1-1)[110].

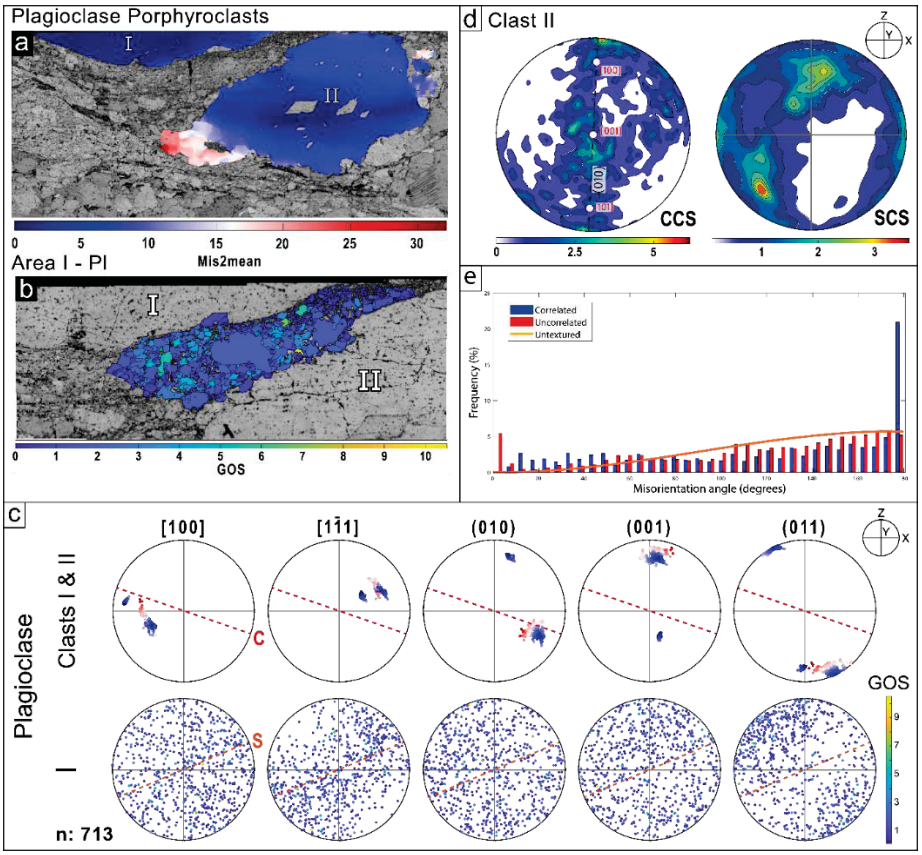

Figure 15 - EBSD data of plagioclase porphyroclasts and the recrystallized fine-grained matrix in protomylonite sample LMD-11. (a) Mis2mean map of the plagioclase porphyroclasts I and II and grain orientation spread (GOS) maps of the (b) recrystallized plagioclase grains (area I) over band contrast map. (d) Pole figure of the crystallographic orientation data of Pl porphyroclast color-coded according to the mis2mean and one point per grain pole figure of the fine-grained plagioclase grains in the area indicated in (b) coloured according to the GOS of the correspondent grain. The pole figures are plotted with respect to an external reference frame (structural XYZ coordinate system) and the local reference frame (S-C foliation). (e) Misorientation axis orientation of the inner subgrain boundaries (2-9°) of Pl porphyroclast plotted in crystal and sample coordinate. (f) Misorientation angle distribution for plagioclase with the correlated and uncorrelated pairs and the theoretical curve for random distributions of the analysed area.

5.4.3.4 Porphyroclast-Matrix relationship

To understand the mechanisms responsible for the grain-size reduction of porphyroclasts and the consequent development of a very fine-grained recrystallized matrix, we performed detailed EBSD analysis to investigate the crystallographic relationship between the feldspar porphyroclasts and the adjacent recrystallized matrix from two Western domain samples (LMD-02 and LMD-11) and one from the Central domain (PSZ-18). Additional analyses are in the Supplementary figures S1 and S2.

5.4.3.4.1 Plagioclase

LMD-11

The studied area of the sample LMD-11 consists of two plagioclase porphyroclasts cut by an S-C surfaces (Fig. 14a, b). These surfaces comprise fine-grained quartz-plagioclase aggregates (~22 μm of average, Fig. 6b). Kfs grains in the recrystallized matrix occur as rare irregular fine grains that fill the framework interstices (Fig. 6b). Figure 15a shows the porphyroclast I and II color-coded according to the internal misorientation angle (mis2mean). While the porphyroclast I display a low mis2mean value (~10°) the porphyroclast II has a high internal lattice distortion (~30° of mis2mean). The high distortion in the lower left part of the porphyroclast is accompanied by the increase in the subgrain boundary density (See Figure 14b). The pole figure show the porphyroclasts I and II (Fig. 15c) in a “soft” orientation for slip on the system (011)[100], with the poles to (011) and [100] axes spreading near the periphery toward the orientation normal and parallel with the c-surface respectively. On the other hand, misorientation axis of Porphyroclast II subgrains in crystal coordinate (Fig. 15d) displays a distribution of the axes along the trace of the plane (010), with two maxima located at the periphery and near the [101] axis, which is consistent with the activation of the systems (010)[100] and (010)[001]. The predominance of misorientation axes maxima away from the Y-axis in specimen coordinates indicates a predominance of twist or mixed boundaries. The presence of twist and mixed boundaries are supported by the boundary trace analysis (Fig. 19a)

in which the dispersion of the axes define a poor rotation axis at the upper right periphery of the pole figure and not fit well with the subgrain trace.

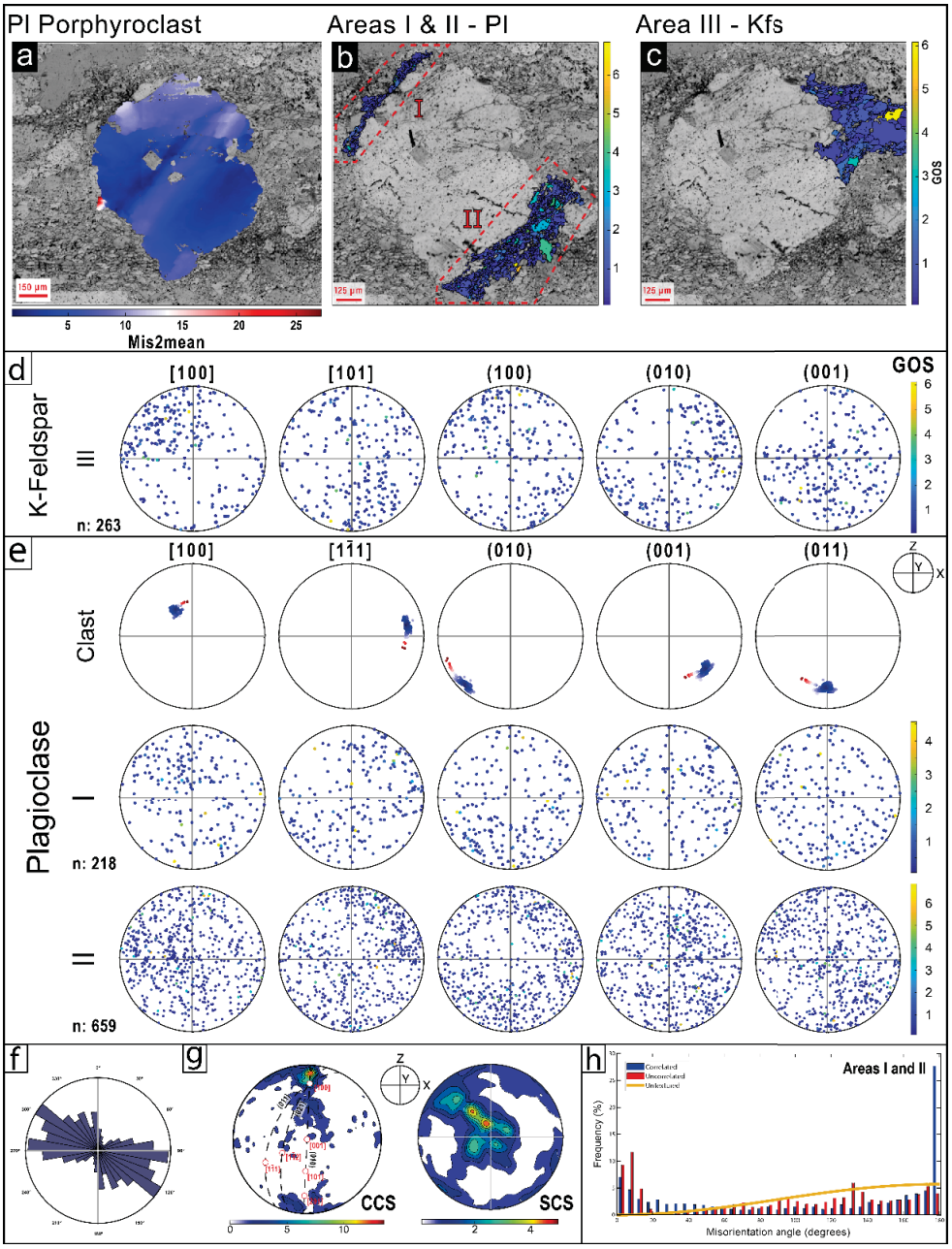

Figure 16 - EBSD data of plagioclase porphyroclast and the surrounding feldspathic matrix in mylonite sample LMD-02. (a) Mis2mean map over band contrast map of the plagioclase porphyroclast and the grain orientation spread (GOS) maps over band contrast map for (b) the adjacent recrystallized plagioclase grains in sites of high-stress (areas I and II) and for (c) precipitated fine-grained K-feldspar in a strain shadow. (e) and (d) are respectively the pole figures of the crystallographic orientation data of plagioclase porphyroclast colour coded according to the mis2mean and the one point per grain pole figures of the plagioclase and K-feldspar grains present in the surrounding recrystallized matrix (areas I, II and III) colored according to the grain orientation spread (GOS) of the correspondent grain. (f) Rose diagram showing the orientation of the long-axes of K-feldspar grains in area III. (g) Misorientation axis orientation of the inner subgrain boundaries (2-9°) of Kfs porphyroclast plotted in crystal and sample coordinate. (h) Misorientation angle distribution for plagioclase with the correlated and uncorrelated pairs and the theoretical curve for random distributions of the analysed area.

The recrystallized grains (Area I, Fig. 15b) have relatively moderate values of GOS, especially the larger grains. The correspondent pole figure shows a concentration of (011) planes normal to the s-surface and the [1-11] spreading out along this surface which is consistent with the (011)[1-11] easy slip system. The histogram (Fig. 15e) shows a relatively high frequency of the low-angle boundaries (for correlated and uncorrelated pairs) which suggest a crystallographic relationship between the new grains and the porphyroclasts.

LMD-02

Figure 16a shows the mis2mean map of a Pl porphyroclast and three areas that represent the fine-grained recrystallized plagioclase in sites of high-stress concentration (areas I and II, Fig. 16b) with an average grain size of ~11-12 μm and a tail (area III, Fig. 16c) of recrystallized K-feldspar (~19 μm of average). Both recrystallized plagioclase and K-feldspar grains show low values of GOS. The porphyroclast displays a high mis2mean (> 25°) and the correspondent pole figure (Fig. 16e) indicate a “soft” orientation for slip on the (011)[1-11] system. The other two Pl porphyroclasts analysed show similar characteristics (see Supplementary figure S2). On the other hand, the misorientation axes correspondent to the subgrain boundaries within the three Pl porphyroclasts analysed in crystal coordinate (Fig. 16g) display maxima at the periphery of the trace of (010) plane or near [100] which may indicate the activity of (010)[001] and (011)[1-11] slip systems. Concentration around [10-1], associated with the activity of the system (010)[001], is also observed. The misorientation axes in specimen coordinates show an equal contribution of low angle tilt, twist and mixed boundaries. The boundary trace analysis (Fig. 19b and Supplementary figure S2) show the rotation axis near the Y-axis and lie within the plane (010) which point out the system (010)[001] as the main responsible for the tilt boundary development.

The poles figure for recrystallized plagioclase in areas I and II (Fig. 16e) show a large scattering of crystal orientations. The pole figures show weak clustering in similar orientations to the parent grain, which argues for initial host control. This is supported by the relatively higher frequency of correlated and uncorrelated low-angle boundaries than the random curve (Fig. 16h) shown by the misorientation angle distribution. On the other hand, the recrystallized Kfs pole figure (Fig. 16d) show

concentrations of (010) planes and [100] directions roughly similar to the host. This show a crystallographic relationship between the Pl porphyroclast and the precipitated Kfs grains.

5.4.3.4.2 K-feldspar

LMD-02

The analysed K-feldspar porphyroclast of the sample LMD-02 (Fig. 17) show a moderate internal lattice distortion (~14° of mis2mean, Fig. 17a). The pole figures of porphyroclast (Fig. 17e) indicate a “soft” orientation for slip on the (010)[100] system, with the poles to (010) planes and [100] directions slightly inclined (~10°) from the Z- and X-axis, respectively. The Misorientation axes of low-angle inner boundaries in crystal (Fig. 17g) support the activation of this system, with a maximum just below the [001]. The boundary trace analysis (Fig. 19c) and misorientation axes in specimen coordinates (Fig. 17g) suggest that the tilt walls are associated with the activation of the system (010)[100].

The recrystallized K-feldspar grains analysed in areas I and II (Fig. 17b) show contrasting textures and shapes. While area 1 is marked by irregular grains with variable grain sizes (up to ~92 μm), high values of GOS and crystal orientations quite similar to the porphyroclast (Fig. 17e), the recrystallized K-feldspar in area 2 consist of small (~13 μm of average) slightly elongated grains with low values of GOS and marked by a weak CPO. The higher frequency of low-angle boundaries in area I than area II (Fig. 17h) point out the host control exerted by the porphyroclast in the new recrystallized grains of area I. The analysis of a well developed recrystallized tail shows a random CPO and the distribution of correlated and uncorrelated misorientation angles are near the random (Supplementary figure S3). The myrmekitic rim analysed in a high-stress site of Kfs porphyroclasts (area III, Fig. 17c) consist of relatively large plagioclase grains protruding into porphyroclast. The grains have low GOS values and similar grain orientations of (010) and [001] axes with the host, which indicate some crystallographic control.

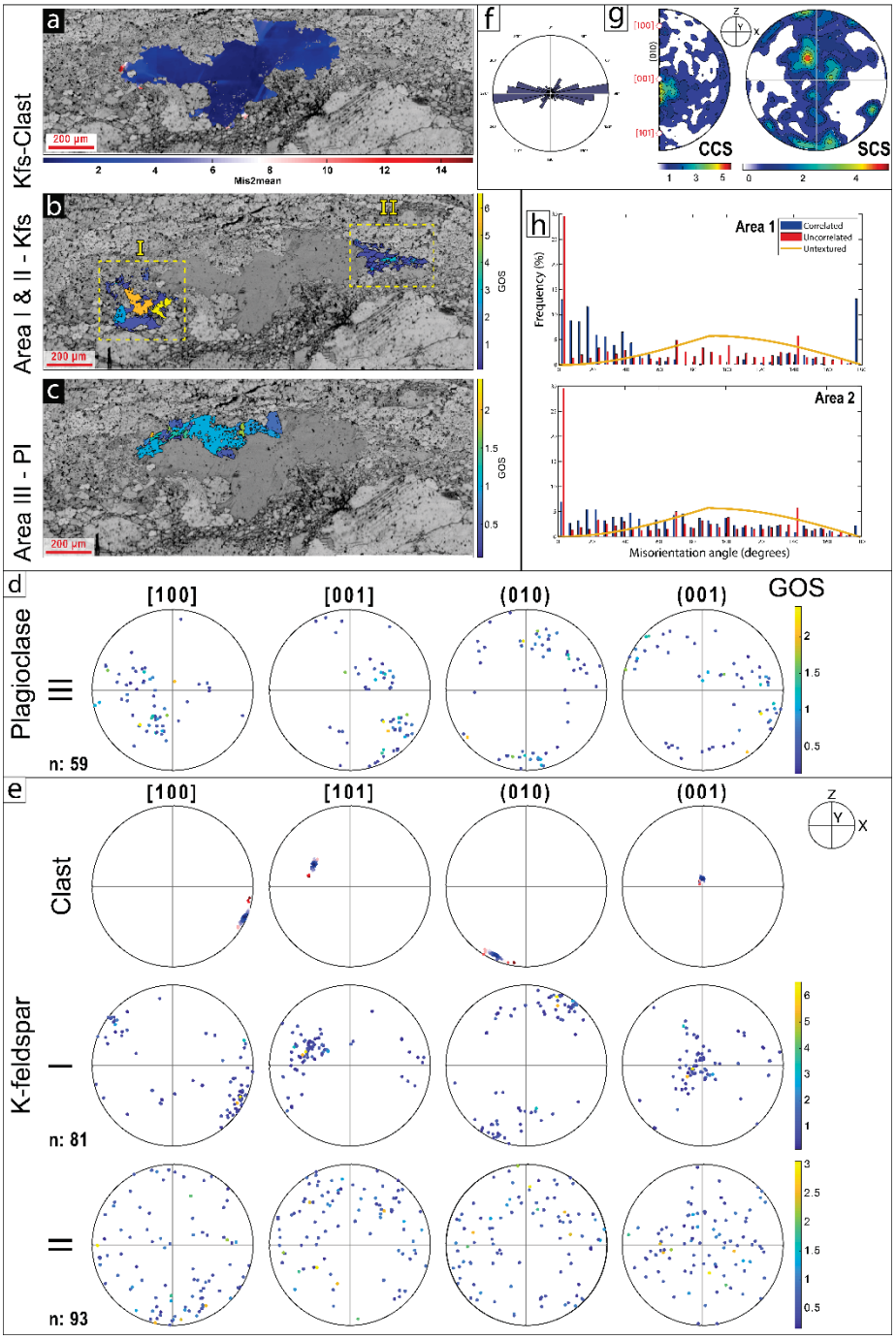

Figure 17 - EBSD data of K-feldspar porphyroclast and the adjacent recrystallized feldspathic matrix in the sample LMD-02. (a) Mis2mean map of the K-feldspar porphyroclast and grain orientation spread (GOS) maps of the (b) aggregates (area I) and tails (area II) of recrystallized K-feldspar and (c) plagioclase in myrmekitic rim (Area 3). (e) and (d) are respectively the pole figure of the crystallographic orientation data of K-feldspar porphyroclast colour coded according to the mis2mean and the one point per grain pole figures for recrystallized K-feldspar (area I and II) and myrmekitic plagioclase (area III) colored according to the grain orientation spread (GOS) of the correspondent grain. (f) Rose diagram showing the orientation of the long-axes of K-feldspar grains in the recrystallized tail (area III). (g) Misorientation axis orientation of the inner subgrain boundaries (2-9°) of Kfs porphyroclast plotted in crystal and sample coordinate. (h) Misorientation angle distribution for plagioclase with the correlated and uncorrelated pairs and the theoretical curve for random distributions of the analysed area.

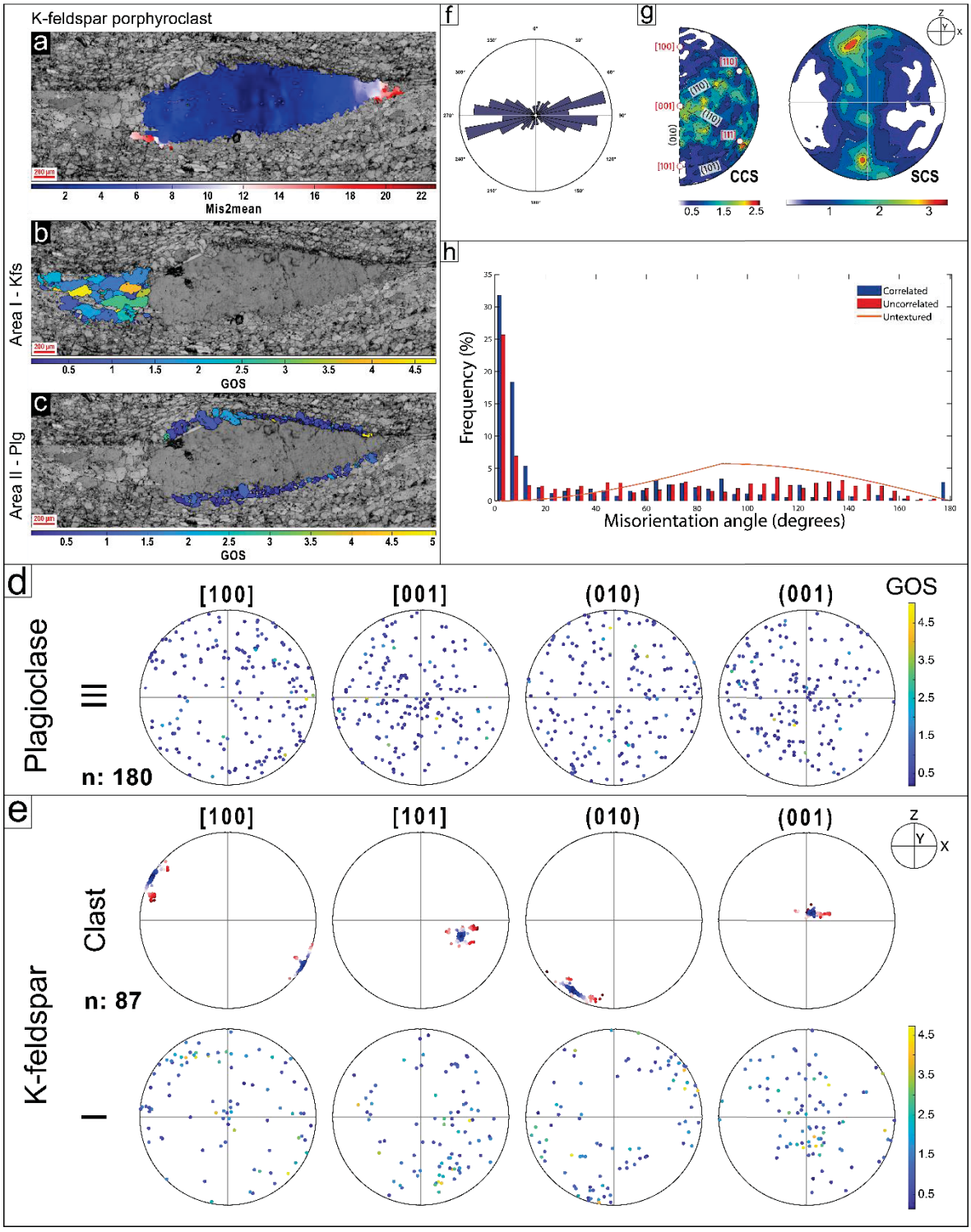

Figure 18 - EBSD data of K-feldspar porphyroclast and the adjacent recrystallized feldspathic matrix in the sample PSZ-18. (a) Mis2mean map of the Kfs porphyroclast and grain orientation spread (GOS) maps of the (b) tails of recrystallized K-feldspar (areas I and II) and (c) plagioclase in myrmekitic rims (Area 3). (e) and (d) are respectively the pole figure of the crystallographic orientation data of Kfs porphyroclast colour coded according to the mis2mean and the one point per grain pole figures for recrystallized K-feldspar (areas I and II) and myrmekitic plagioclase (area III) colored according to the grain orientation spread (GOS) of the correspondent grain. (f) Rose diagram showing the orientation of the long-axes of K-feldspar grains in the recrystallized tail (area III). (g) Misorientation axis orientation of the inner subgrain boundaries (2-9°) of Kfs porphyroclast plotted in crystal and sample coordinate. (h) Misorientation angle distribution for plagioclase with the correlated and uncorrelated pairs and the theoretical curve for random distributions of the analysed area

PSZ-18

Figure 18 show the EBSD data for the elongated K-feldspar porphyroclast and the adjacent areas (Fig. 14e, f) which comprise a tail of recrystallized K-feldspar (area I) and myrmekite rims (area II). The mis2mean map (Fig. 18a) shows that the Kfs porphyroclast have a relatively high internal lattice distortion (~22°), but the distortion is higher at the extremities. The correspondent pole figure (Fig. 18e) shows the poles to (010) and [100] in the periphery of the pole figure rotated clockwise (~25°) from the respectively Z- and X-axis, consistent with a “soft” orientation for the slip on the (010)[100] system. The misorientation axes in crystal coordinates display a wide concentration just below the [001] axis and a maximum near [111] which corresponds to the activity of slip systems (010)[100] and the tentative (-110)[001]. The axes plotted in specimen coordinate indicate a greater contribution of twist subgrain boundaries compared to the tilt subgrain boundaries. The boundary trace analysis of the orientation dispersion (Fig. 19d) show the rotation axis lying within the plane (010) and away ~90° from the [100] axis which is consistent with tilt boundaries produced by the activation of the system (010)[100].

The recrystallized tail (area I) is composed of large and elongated K-feldspar grains (~36 μm of average) with a significant presence of subgrains boundaries perpendicular to the foliation (Fig. 14f) but low values of GOS (Fig. 18b). The recrystallized Kfs CPO (Fig. 18e) is characterized by some grains with orientations similar to the porphyroclasts which indicates an initial host control. The poles to (100) planes scatter toward orientations normal to the preferred orientation of the grains long axis (Fig. 18f) with some poles to [010] axis aligned parallel to it. The host control and the presence of subgrains are also supported by the misorientation angle distribution which shows a high frequency of low-angle boundaries. On the other hand, the CPO of the neighbour plagioclase grains (area II, Fig. 18c) is random and indicates no host control relationship between the myrmekitic plagioclase and the porphyroclast. The plagioclase grains also show low values of grain orientation spread and a random CPO pattern (Fig. 18d).

5.5 DISCUSSIONS

5.5.1 Deformation mechanisms and slip systems

5.5.1.1 Magmatic-state deformation

The outcrops of deformed anatexite of this rock typically exhibit structures formed during a magmatic-state deformation like leucosome filling shear bands (Fig. 3b), complex fold patterns (fig. 3a) and magmatic foliation. Field and microscope observations show that the rock displays little evidence of solid-state deformation. The fabric is characterized by a weak CPO and a limited degree of recrystallization. The quartz and feldspar grains are only affected by intracrystalline deformation, with features typically developed during the activity of recovery processes. These characteristics suggest deformation under an exclusively magmatic state (e.g., Vernon, 2000) which also was proposed by Viegas et al., (2014). Furthermore, Viegas et al., (2013) demonstrated that Espinho Branco anatexite displays magnetic fabrics compatible with the regional strain field.

5.5.1.2 Submagmatic-solid-state transition

The outcrops LMD-11 and LMD-12 display structures which indicate melt-assisted deformation. These structures, that include leucosome veins cutting mylonitic foliation and filling shear bands, are concomitant with the solid-state deformation. Leucosome veins and leucogranite dykes occurring as boudins or pinch-and-swell structures (Fig. 2b) suggest that the melt products were the competent domains during high-temperature shearing (e.g., Cacalvante et al., 2016).

Microscopically, the ultramylonite shows melt-related microstructures (Fig. 5a) and the feldspar consist of irregular- and elongate-shaped grains with intracrystalline microstructures and with a CPO pattern indicative of the activation of (010)[100] slip system. This slip system was observed in plagioclase-rich rocks deformed at temperatures higher than 700°C (Závada et al., 2007; Mehl and Hirth, 2008). Satsukawa (2013) commented that this CPO pattern may be developed by crystal-plastic deformation overprinting magmatic flow which supports melt-assisted crystal-plastic deformation. The quartz CPO displays a weak pattern that may

indicate the activity of rhomb-<a> and minor prism-[c]. However, the misorientation axis analysis shows that the subgrains are associated with the slip systems prism-<a> and minor prism-[c] (Fig. 11), which is consistent with the high-temperature deformation and the chessboard extinction present within quartz (e.g., Mainprice et al., 1986). In addition, the weak CPO pattern and preserved magmatic quartz suggest that the quartz undergone limited dislocation creep after melt crystallization. Finally, micro-scale observations allied with outcrop observations suggest that this sample was deformed during the transition from submagmatic to solid-state flow (e.g., Vernon, 2000).

5.5.1.3 Solid-state Deformation

5.5.1.3.1 Medium-temperature deformation (transitional mylonites)

The transitional mylonite from the Central domain (PSZ-17) shows sheared leucosome lens (Fig. 3c) but no melt-related structures, which indicate solid-state flow. The presence of equally elongated grains as well as quartz CPO defined by a type-I cross-girdle argues for a component of coaxial deformation. The crystal-plastic microstructures, CPO and misorientation analysis suggest deformation accommodated by dislocation creep with dominant slip on the system prism-<a> for quartz. The lack of CPO and crystal-plastic microstructures in the elongated plagioclase grains could indicate that the feldspar behaves as a rheological rigid object during the shearing, with quartz and biotite accommodating most of the bulk strain (clast-matrix structure of Handy, 1990).

Some transitional mylonites from the Western domain (LMD-01 and LMD-02) have quartz aggregates characterized by grains with very lobate boundaries and with microstructures typical of recrystallization by GBM like *left-over* grains or dissection grains (Jessel, 1987; Stipp et al., 2002). The quartz aggregate CPO consist of an incomplete single girdle (see pole figure for sample LMD-01). On the other hand, the samples dominated by quartz ribbons (LMD-02 and LMD-11) display [c]-axis CPOs with a strong single Y maximum and are constituted by slightly elongated grains defining oblique foliations, which suggest recrystallization during GBM-SGR transition (Passchier and Trouw, 2005), with the activation of the dominant slip system prism-<a>. The high frequency of low-angle boundaries (2-40°) of correlated and

uncorrelated pairs also argue for a high frequency of new grains generated by SGR. Heilbronner and Tullis (2006) suggest that the transition from an incomplete single girdle to a single maximum near Y-axis accompanied by an increase in fabric strength may occur with increasingly shear strain. The transition from GBM to SGR may also occur under decreasing temperatures at temperatures ~500°C (Stipp et al., 2002). Therefore, the local strengthening of CPO and in the single Y maximum may be attributed to a strain increase during GBM-SGR transition as the new “soft” are formed by SGR.

The feldspar porphyroclasts of the transitional mylonites and of the low-temperature sample PSZ-18 display microstructures like deformation bands, bent and deformation twins that suggest crystal-plastic deformation (e.g., Shaocheng and Mainprice, 1990; Kruse et al., 2001). The Kfs porphyroclasts CPO show that most of them are in “soft” orientations for slip on the (010)[100] system and exert a strong crystallographic control in the new recrystallized grains, which suggest deformation by dislocation creep. The clasts in “soft” orientations also have high-aspect ratios but lower GOS values than Pl porphyroclasts (Compare Figs. 17 and 18 with the Supplementary figure S2). The lower GOS values may be explained by the consumption of grains by myrmekitization. The boundary trace and misorientation axis analysis indicate that low-angle tilt boundaries are associated with the slip system (010)[100], whereas twilt and mixed boundaries are probably associated with the systems (010)[001]. The tentative (-110)[001] inferred by the misorientation axis is unlikely since the (-110) plane has never been observed by either TEM or EBSD analysis (Willaime et al., 1979; Sacerdoti et al., 1980; Scandale et al., 1983).

The Pl porphyroclasts CPOs show that most of them are in favourable orientations for slip on the (011)[1-11], (011)[100] and (021)[1-12] systems. However, the porphyroclast, in general, have low-aspect ratios, and the asymmetry shown by the CPO is the opposite of pointed out by the mylonitic foliation asymmetry (Fig. 12). In fact, only the Pl porphyroclasts of sample LMD-01 regarding the system (011)[100] and the new recrystallized grains are in favourable orientations for slip on the systems (011) in the directions [100] and [1-11], and (010)[100], as indicated by the IPFs (Supplementary figure S1). Furthermore, the dispersion of porphyroclast orientations is consistent with a dextral shear sense and the boundary trace and misorientation axis analysis of Pl porphyroclasts indicate a great contribution of the slip systems (010)[001] in plagioclase during the tilt and mixed boundary

development (Figs. 15d and 16g). Other slip systems like (010)[100] and possibly (011)[1-11] in plagioclase are possibly associated with the development of twist or mixed boundaries. Contrasting easy slip systems and subgrain-related slip systems were recently addressed by some studies (e.g., Kilian, 2015; Kilian, 2017; Jung et al .,2021), but whether this represents different conditions of deformation (e.g., Jung et al., 2021) or if this indicates that accommodation of homogenous deformation by dislocation glide operate different slip systems of those responsible by subgrain development (e.g., Kilian, 2015) is not well understood yet.

Our observations resulted in some interesting findings. Both (011)[1-11] and (021)[1-12] are slip systems that have been reported by previous studies. However, while the first was observed by TEM analysis (Montard and Mainprice, 1987), the second only was inferred by the use of the easy slip system method (e.g., Kruhl, 1987; Baratoux et al., 2005; Svahnberg and Piazolo, 2010), with no TEM study confirming its existence (e.g., Marshall and MacLaren, 1977a, b; Olsen and Kohlstedt, 1984; Stünitz et al., 2003). Some EBSD studies in Pl-rich rocks also advocate for (011) as a possible slip plane (Cross, 2015; Miranda et al., 2016) and [1-11] as a slip direction (Marshall and MacLaren, 1977a). Moreover, the papers that reported the (021)[1-12] system did not show the pole figures for (011) and [1-11] axes. Since the planes (011) and (021), as well as the directions [1-11] and [1-12], are very close to each other, both may define similar CPO patterns whether one or the other was active during easy slip as evidenced by this study. Thus, we suggest that the (021)[1-12] slip system is derived from a misinterpretation of the plagioclase CPO developed by the easy slip on the system (011)[1-11].

5.5.1.3.2 Low-temperature deformation

The mylonite sampled at the southern part of Central domain (PSZ-18) show microstructures indicative of higher temperatures than the sampled in the Western domain (LMD-10). The first exhibits continuous ribbons of elongated quartz grains recrystallized by SGR with local overprint by BLG and the [c]-axis display a strong Y maximum which is indicative of dominant prism-<a>. In contrast, the quartz ribbons of the second are discontinuous and show microstructures typical of recrystallization by strain-induced grain boundary migration (BLG) and a CPO pattern that indicates the activation of easy slip systems basal, rhomb and prism-<a>. However, the quartz

misorientation analysis of subgrains from the sample LMD-10 argues only for prism<a>. Clustering around axis associated with rhomb-<a> and basal-<a> are few and are only found when we analyse the misorientations angles that comprise the transition of subgrains to grains (9-15°). This inconsistency has been discussed by some recent studies (Kilian et al., 2017 and references therein) which argue that basal-<a> is not a significant slip system. In addition, Keller and Stipp (2011) suggest that peripheral single [c]-axis maximum can be achieved by other slip systems not suitable for easy slip. Therefore, we propose dominant prism<a> and minor rhomb-<a> as active during deformation of quartz ribbons in the sample LMD-10.

Despite the Kfs porphyroclasts of the sample PSZ-18 display microstructures that indicate recrystallized-accommoddation dislocation creep as discussed before, in the both LMD-10 and PSZ-18 the Kfs grains are extensively cut by several fractures oriented at high angles to foliation. Subgrains with the same orientation of fractures observed in feldspar grains may have been formed due to this microfracturing (e.g., Tullis and Yund, 1987) but its crystal-plastic origin is not unlikely. However, fine grains along fracture surface were not observed, which indicate that fracturing was more a support mechanism for solution-precipitation creep than a grain-size reduction mechanism (e.g., Fukuda et al., 2012). On the other hand, the feldspar aggregate in the sample LMD-10 shows evidence for dissolution-precipitation creep and anisotropic growth, which include: i) the presence of polygonal, moderately elongated free-strain grains defining SPO, with the long axis parallel to the extensional Instantaneous extensional axis and ii) Well developed CPO with the planes of fast and slow reaction rate parallel to the long and short axis respectively (Bons and Brok, 2000; Menegon et al., 2008). According to our observations, for plagioclase, the slow reaction rate axis is (001) and the fast reaction rate axes are the [010] and [100] directions which are similar to the axes proposed for albite (Heidelbach et al., 2000, Arvidson et al., 2004).

5.5.2 Grain-size reduction mechanisms

Our observations indicate three main mechanisms responsible for grain size reduction and polyphasic matrix formation: i) recrystallized-assisted dislocation creep; ii) reaction softening and iii) solution precipitation creep. In this section, we discuss the contribution of each mechanism.

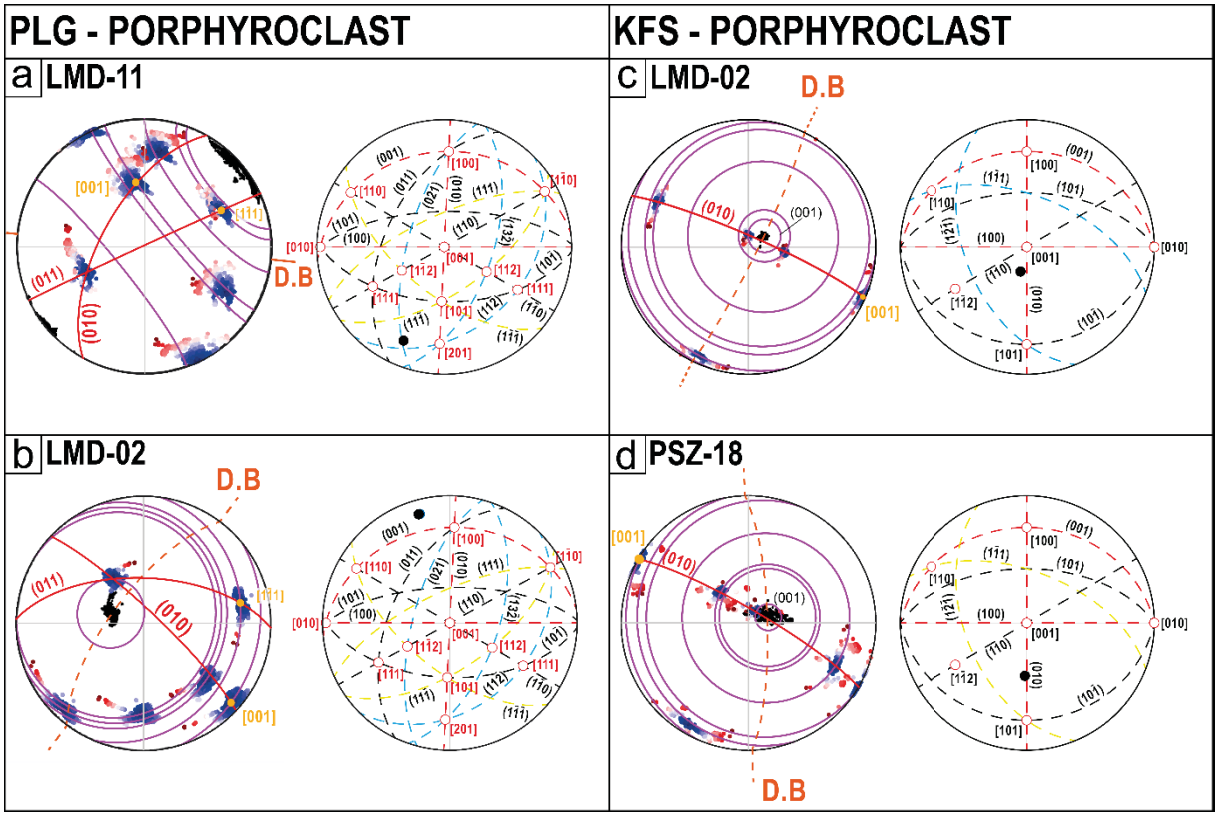

Figure 19 - Boundary trace analysis of the analysed porphyroclasts. (a) and (b) correspond to the Pl porphyroclasts of the samples LMD-11 (see Fig. 15a and c) and LMD-02 (see also Fig. 16a and e) analysed in detail. (c) and (d) are the analysed K-feldspar porphyroclasts of the samples LMD-02 (see Fig. 18a and e) and PSZ-18 (see also Fig. 19a and e) respectively. The direction which best fit with the most probable rotation axis is indicated as a blue point in the specimen coordinate.

5.5.2.1 Grain-size insensitive mechanisms

Recrystallized grains with relatively high GOS and strong host control are observed around Kfs clast, but they are few and relatively larger. On the other hand, the plagioclase porphyroclasts often show very fine recrystallized grains normally in sites of high normal stress (~45° from foliation) with some or no initial control from the host. Sites with high-stress concentrations may accumulate dislocations and strain energy (e.g., Simpson and Wintsch, 1989) which may favour the strain energy-driven nucleation of new grains (Kruse et al., 2001). Furthermore, the higher subgrain density and GOS values in the Pl porphyroclasts than K-feldspar porphyroclasts, indicate that strain-driven recrystallization was more active in plagioclase than alkaline feldspar, which is consistent with the observed in previous studies (e.g., Pryer, 1993; Schulmann et al., 1996). Therefore, we suggest that the high normal stress borders of plagioclase accumulate high strain energy during shearing which

favours the nucleation of new fine recrystallized grains by strain-driven recrystallization.

Table 1 - Summary of the deformation mechanisms and slip systems inferred for quartz and feldspar of Patos mylonites from this study

Samples	Deformation flow type	Quartz	K-feldspar	Plagioclase
LMD-12	Magmatic/ solid-state transition	Dislocation Creep Prism-<a> Prism-[c]	Dislocation creep (010)[100]	Dislocation creep (010)[100]
LMD-11	Solid-state	Dislocation Creep SGR Prism-<a>	Myrmekitization Sol-prep. Creep	Dislocation creep (010)[100][001] DisGBS (011)[1-11]
LMD-01	Solid-state	Dislocation Creep GBM-SGR Prism-<a>	Dislocation creep (010)[100] Myrmekitization Sol-prep. creep GBS	Dislocation creep (011)[100]?
LMD-02	Solid-state	Dislocation Creep SGR Prism-<a>	Dislocation creep (010)[100][001] Myrmekitization Sol-prep. Creep GBS	Dislocation creep (010)[001][100] DisGBS (010)[100]?
LMD10	Solid-state	Dislocation Creep BLG Prism-<a> minor Rhomb-<a>	Fracturing Diss-prep. creep	Diss-prep. creep
PSZ-21	Magmatic-state	Limited intracrystalline plasticity	Not determined	Not determined
PSZ-17	Solid-state	Dislocation Creep Prism-<a> Minor fracturing		Minor fracturing
PSZ-18	Solid-state	Dislocation Creep SGR Prism-<a>	Limited Dis. Creep (010)[100] Myrmekitization Sol-prep. Creep Fracturing;	DisGBS (10-1)[111] (1-1-1)[110]

5.5.2.2 Reaction softening and dissolution-precipitation creep

The Kfs porphyroclasts of transitional mylonites and from the sample PSZ-18 commonly have dissected habits and are surrounded by myrmekitic rims, especially in high normal stress sites (e.g., Simpson and Wintsch, 1989; Vernon, 1991). Subsequent disruption and shearing of myrmekite structure form the fine-grained Qtz-Pl aggregates (Fig. 6d-e), a process similar to that observed by Ceccato et al., (2018). The Potassium released tend to precipitate as smaller Kfs grains in sites of low normal stress (e.g., Simpson and Wintsch, 1989; Tsurumi et al., 2003). In our samples, these sites are strain shadows, dilational sites between porphyroclasts

fragments or between framework grains in fine aggregates (Fig. 5e, i). All this evidence, allied to limited dynamic recrystallization of Kfs porphyroclasts, suggest coupled myrmekitization and solution-precipitation creep as the main processes responsible for the grain-size reduction and formation of the fine-grained Kfs tails, which favour phase mixing and switch to grain-size sensitive mechanisms (e.g., Menegon et al., 2006; Ceccato et al., 2018). The presence of local flame perthites in the fine aggregates without preferred orientation also argue for Interface-coupled replacement of K-feldspar by albite during dissection of recrystallized tails due to chemical disequilibrium (e.g., Hentschel et al., 2019).

The K-feldspar grains in strain shadows show evidence of anisotropic growth characterized by a preferred elongation of strain-free grains. These grains display a CPO characterized by the poles to (100) planes orthogonal to the long axis and the [010] directions parallel to it. This pattern is stronger in the medium-grained K-feldspar ribbons (PSZ-18) but weaker or inexistent in the tails of fine recrystallized Kfs grains in the transitional mylonites. This CPO pattern suggests that the directions of slow and fast reaction rate are respectively (100) and [010] axes, the opposite of proposed by Menegon et al., (2008) and corroborated by Fukuda et al., (2012). A similar CPO pattern was found by Ishii et al., (2007) and was subsequently reported as a possible slip system by Menegon et al., 2008 and Viegas et al., (2014). However, TEM analysis in both experimental and natural deformed K-feldspar-rich rocks or single crystals never observed the presence of this slip system (Willaime and Gandais, 1977; Willaime et al., 1979; Sacerdoti et al. 1980; Scandale et al., 1983). Tullis (1983) argue that the direction [010] is a very large burger vector to be considered a suitable slip direction, and this vector must dissociate into ½[110] and ½[-110]. Furthermore, the EBSD data for precipitated K-feldspar in dilational sites indexed by using the structure of microcline display the same CPO pattern proposed by Menegon et al., (2008), but show wrong solutions when used to index the Kfs porphyroclasts (See the supplementary Figure 4). This contradiction may be explained by the preserved monoclinic structure in porphyroclasts. Some studies suggested that even temperatures below of considered for orthoclase-microcline inversion (~500°C, Deer et al., 1992), some regions of crystals can retain partially ordered orthoclase structure (MacKenzie, 1954, Eggleton and Buseck, 1980; Fitz Gerald and McLaren, 1982). On the other hand, a fully ordered microcline can be precipitated from the solution at temperatures below ~500°C (Waldron et al., 1993).

Therefore, the CPO pattern for precipitated Kfs may be a product of a misguided solution during the indexing of fully ordered microcline grains using the monoclinic K-feldspar structure. Finally, if our interpretation is true, the dissolution-precipitation creep must have occurred under temperatures lower than ~500°C in the sample PSZ-18.

In conclusion, we suggest that, at temperatures that comprise ~450 - 500°C, the coupled reaction softening and solution-precipitation transfer are the main mechanism responsible for the grain-size reduction of K-feldspar and the formation of the quartz-plagioclase aggregates in the transitional mylonites of PSZ.

5.5.2.3 Grain-size sensitive creep mechanisms

The shearing of myrmekite rims, fine-grained recrystallized Pl aggregates and fine-grained Kfs aggregates in recrystallized tails are all accompanied by the scattering of the orientations from the host, phase mixing and reduction of low-angle boundaries which suggest deformation by grain boundary sliding (Jiang et al., 2000; Bestmann and Prior, 2003). However, the presence of CPO, some grains with moderately internal lattice distortion and grains larger than 10 um argue that the GBS was rate-limited by dislocation glide with the activation of the easy slip systems (10-1)[111] and (1-1-1)[110] in the sample PSZ-18 (Fig. 13), (011)[1-11] in the sample LMD-11 and possibly (010)[100] in the sample LMD-02 (Fig. 12), which are notably distinct from those deduced by subgrain analysis. Deformation by both GBS and dislocation glide on the easy slip system is commonly attributed to DisGBS (warren and Hirth, 2006, Tokle et al., 2019) and have been documented in fine-grained quartzo-feldspathic aggregates (e.g., Svahnberg and Piazolo, 2010; Czaplinska et al., 2015). DisGBS may promote weakening by geometrical softening and phase mixing (Hansen et al., 2012) which turn the fine-grained aggregate rheologically weaker than the feldspar porphyroclasts, which behave as “rigid” objects rotating passively into “hard” orientations during shearing (e.g., Handy, 1990; Miranda et al., 2016). This may explain the incongruence between GOS, CPO and subgrain-related slip systems in the porphyroclasts. Furthermore, the voids typically created by the sliding of grains are compensated by the elongation of grains which explain the lack of K-feldspar precipitated in the interstices of some Qtz-Pl aggregates. The grain size

is maintained small mainly by the presence of mixed grains derived from myrmekite and precipitated by solution-precipitation creep, which avoids grain growth.

Based on these arguments, our results indicate that the GBS plays an initial role in the new recrystallized grains by rotating the grains into orientations favourably to dislocation glide in the easy slip systems limiting the rate of GBS.

5.5.3 Strain localization in micro-scale high strain zones

Many studies demonstrated that discontinuities like fractures, dykes or layer contacts serve as structural precursors that favour the nucleation and initial development of shear zones (e.g., Segall and Simpson, 1986; Oliot et al., 2014; Goncalves et al., 2016, Wehrens et al., 2017; Zibra et al., 2018). This is consistent with our field, optical and SEM observations which show high-strain zones localized in discontinuities between rheological domains like paleosome-leucosome, dykes-host rock contacts or domains of different composition or grain sizes at grain-scale (Fig. 2f, g). These ductile structures seem to nucleate from sites with local fracturing and develop as intergranular fractures reducing the framework grains and interconnecting the phyllosilicates. In our samples, sites with stress concentrations exhibiting flame perthites or local microcracking are located preferentially in interphase boundaries (Fig. 8d). This is consistent with experiments conducted by Holyoke and Tullis (2006a, b) in mica-quartz-feldspar aggregates, which show that cataclasis due to stress concentrations in biotite-framework grains boundaries promote the interconnection of the phyllosilicates (weak phases) by easy slipping. Once nucleated, the fracture propagates throughout the grain boundaries allowing fluid influx and hence promoting the alteration of both feldspar and biotite to low-temperature phyllosilicates (e.g., Ingles et al., 1999; Oliot et al., 2010; Oliot et al., 2014). On the other hand, the substantial lack of mineral alteration in the shear bands points out higher temperatures of formation than those attributed to micro-shear zone development. The interconnectivity of layers may cause significant weakening during initial shearing (Dell'Angelo and Tullis, 1986; Holyoke and Tullis, 2006a, b; Hunter et al., 2016) and enhance softening reactions which lead to further strain weakening and localization (e.g., Ingles et al., 1999; Chakraborty et al., 2020; Mansard et al., 2020). Subsequent coalescence and widening form the anastomosing network of interconnected layers observed in our samples (e.g., Oliot

et al., 2014). These localized high strain zones promote enhanced grain size reduction and phase mixing by GBS (see Fig. 8a and c) weaken further the rock strength by creating weak zones where the strain is localized.

5.5.4 Deformation conditions of Patos mylonites

The high-temperature mylonite from Western domain show quartz with chessboard extinction and microstructures that suggest melt-assisted deformation which indicate temperatures higher than 650°C for the high-temperature (e.g., Kruhl, 1996; Garlick and Gromet, 2004). Quartz c-axis fabric with opening angles of ~100° points out temperatures around 718°C using the calibration of Faleiros et al., (2016). This is consistent with temperatures higher than 700°C suggested by Corsini et al., (1996) using garnet-biotite rims in metapelites near Cajazeiras. Similar temperature was estimated by Caby et al., (1995) in the Central domain. Furthermore, Viegas et al., (2014) described microstructures and deformation mechanisms very similar to those observed in our samples. This show that both domains record similar thermal history during high-temperature deformation that occurs during concomitant partial melting at 565 Ma (Viegas et al., 2014, Archanjo et al., 2021).

The transitional mylonites from the Western domain exhibit microstructures and deformation mechanisms that are consistent with deformation at upper greenschist to lower amphibolite facies conditions (Pryer, 1993; Tullis, 2002) and suggest temperature higher than at least 500°C and lower than 550° for the medium-temperature mylonites (Stipp et al., 2002; Czaplińska et al., 2015). The opening angle of quartz c-axis fabric (~65°) of the transitional mylonite from the Central domain indicate a temperature around 500°C. Ar-Ar ages on hornblendes (Corsini et al., 1998; Monié et al., 1997) suggest that medium-temperature deformation occurred at 545 Ma, since the closure temperature for metamorphic amphibole range between 550-500°C (Harrison, 1981). Hollanda et al., (2010) attribute this age to a mylonitization at upper greenschist to lower amphibolite facies conditions concomitant to dyke intrusions in Coxixola Shear zone and suggest that this event may be related to late collisions during the Gondwana formation. The augen gneiss deformed at these medium temperatures indicates that the reactivation was not restrained in the southern borders of PSZ, but may occur distributed throughout the lineament as narrow high-strain zones.

The fracturing and dissolution-precipitation creep of feldspar porphyroclasts, lack of mineral alteration and recrystallization by BLG of quartz grains suggest that the low-temperature deformation occurred under lower greenschist facies conditions, at temperatures smaller than ~450°C (e.g., Stipp et a., 2002; Tullis, 2002). The medium-temperature microstructures observed in the sample PSZ-18 attribute a transitional character between the medium- to low-temperature deformation. The presence of limited dislocation creep observed in K-feldspar porphyroclasts and aggregates of the sample PSZ-18 argue for a transitional character between the medium- to low-temperature deformation (Viegas et al., 2014) and is consistent with the lower cooling rate during uplift recorded by the Central domain compared to the Western domain.

5.5.5 Solid-state flow and strain localization in the Patos Shear Zone

On the basis of our discussion and previous studies, we propose a simplified trajectory of microstructures during the evolution of PSZ. The main deformation mechanism for quartz and feldspar are summarized in Table 1.

During deformation concomitant with partial melt, at 565 Ma, the presence of biotite in biotite-rich layers prevent grain growth by pinning the grains and consequently keep the size of grains smaller than the biotite-absent layers (e.g., Hunter et al., 2016). Furthermore, the development of a feldspar CPO by dislocation creep promotes further weakening by geometric softening (e.g., Shaocheng and Mainprice, 1988; Burlini and Bruhn, 2005). The consequence is that, with the crystallization of the melt, the phyllosilicate-rich layers became the weaker domains, and accommodate most of the bulk strain.

During the later reactivation at 545 Ma, both feldspar and quartz initially accommodated strain by recrystallized-assisted dislocation creep. Sites of high normal stress favour the myrmekitization of Kfs porphyroclasts with precipitation in strain shadows and strain energy-driven recrystallization in Pl porphyroclasts which promote the grain-size reduction of large grains (e.g., Pryer, 1993). The new fine-grained recrystallized aggregates deform by either dislocation creep-accommodated or fluid-assisted GBS. As the strain is accumulated during the transition from GBM to SGR recrystallization, the quartz aggregates turn into quartz ribbons, marked by the dominant activation of dominant Prism-<a>. The late development of shear bands

promotes interconnection between biotite flakes, grain size reduction and phase mixing along narrow surfaces which promote further weakening (e.g., Stünitz and Tullis, 2001; Menegon et al., 2008; Papeschi and Musumeci, 2019). While the feldspar porphyroclasts and quartz ribbons behave as hard domains as evidenced by the boudinaged of ribbons, the weak layers are constituted by new fine-grained recrystallized aggregates and the grains along shear bands deforming via grain-size sensitive mechanisms (e.g., Menegon et al., 2008; Miranda et al., 2016). These fine-grained aggregates control the bulk rheology of the rock and reduce the viscosity contrast between layers of the compositional banding, resulting in an isoviscous flow at the outcrop-scale, as evidenced by the lack of significant boudinage and pinch-and-swell structures between the layers (e.g., Hunter et al., 2019).

During the last stages of PSZ, under greenschist facies conditions, fracturing and dissolution-precipitation creep are the dominant deformation mechanisms that affect the feldspar. High-temperature microstructures in quartz ribbons are overprinted by BLG recrystallization. Rocks deforming only by dislocation creep and dissolution-precipitation creep may have higher viscosity compared to the surrounding rocks deforming by GSS creep (e.g., Platt, 2015). The viscosity contrast during deformation partitioning may explain the local constrictional strain recorded by the L-tectonite as proposed by Yang et al., (2019). However, was not possible to determine if the observed opposite shear sense recorded by these L-tectonites is either a product of local vorticity contrast during the flow or an expression of a regional sinistral shearing that affect the Transversal zone (Vauchez et al., 1995). Discontinuities played an important role during the low-temperature deformation, especially in the northern block of PSZ. Layer contacts and transgranular fractures developed along interphase boundaries favour fluid influx and stress concentrations which lead to local cataclasis and reactions that generate weak phases at the expense of “hard” phases like feldspar. This leads to the nucleation and development of small-scale, localized shear zones along these discontinuities. These zones promote further grain-size reduction, phase mixing and softening by reactions that reduce the rock strength. The fact that these micro-shear zones are pervasively distributed throughout the PSZ indicates that the medium- to low-temperature deformation was not restrained to the southern zone of PSZ, although the expression of this deformation in the northern block was more localized than the southern block.

5.6 CONCLUSIONS

We study quartzo-feldspathic rocks of PSZ mylonitized under High, medium and low-temperature conditions. Our results demonstrated that PSZ record an inhomogeneous deformation with the strain being accommodated and localized in increasingly thinner high strain zones as the temperature decrease. A model was proposed, which shows as different processes acted to promote crustal weakening during the uplifting of PSZ. The model state that:

I: After melt crystallization and under high temperatures conditions (>700°C), biotite and geometric softening by CPO development was the main mechanisms responsible for initial strain weakening in biotite-rich layers in relatively thick high strain zones

II: During deformation under medium-temperature conditions (550-480°C), strain weakening is promoted by the formation of fine-grained recrystallized aggregates by couple myrmekitization and solution transfer of K-feldspar porphyroclasts and strain-driven recrystallization in plagioclase porphyroclasts. The matrix deforms via dislocation-accommodated or fluid-assisted GBS. Further weakening is promoted by localized shearing along shear bands and S-C surfaces.

II: In the last stages of PSZ, under low-temperature conditions (<450°C) the main mechanisms are fracturing and dissolution-precipitation creep. Strain is localized along micro-shear zones developed from discontinuities. These zones promote additional weakening by further grain-size reduction, softening reactions and phase mixing.

Our slip system analysis indicates that systems responsible for the subgrain formation in plagioclase are notably different from those attributed to accommodate strain by easy slip. The plagioclase porphyroclasts record the activation of (010)[100] and (010)[001] slip systems and the fine-grained aggregates record the activation of (011)[100], (011)[1-11], (10-1)[111] and (1-1-1)[110] easy slip systems. The K-feldspar porphyroclasts and recrystallized grains record the activation of (010)[100] slip systems. We also proposed that the (021)[1-12] slip system for plagioclase and (100)[010] for K-feldspar are products of misinterpretation. The first is derived from the proximity of the (021) planes and [1-12] directions to (011) and [1-11] axes, respectively that lead to similar CPO patterns in pole figures. The second is derived from an indexing problem related to the degree of triclinicity in the potassic feldspar.

This show that the easy slip method must be used carefully and supported by other methods like subgrain boundaries analysis or boundary trace analysis, especially if the easy slip system was never observed in TEM analysis.

5.7 REFERENCES

Angelim, L.A.A., Vasconcelos, A.M., Gomes, J.R.C., Wanderley, A. A., Forgiarini, L.L., Medeiros, M.F., 2004. Folha SB.24-Jaguaribe. In: Schobbenhaus, C., Gonçalves, J.H., Santos, J.O.S., Abram, M.B., Leão Neto, R., Matos, G.M.M., Vidotti, R.M., Ramos, M. A. B., Jesus J. D. A. (Ed.), Carta Geológica do Brasil ao Milionésimo, Sistema de Informações Geográficas-SIG, Programa Geologia do Brasil, Brazilian Geological Survey (CPRM), scale:1:1,000,000.

Archanjo, C.J., Fetter, A.H., 2004. Emplacement setting of the granite sheeted pluton of Esperança (Brasiliano orogen, Northeastern Brazil). 135, 193–215. https://doi.org/10.1016/j.precamres.2004.08.008

Archanjo, C.J., Viegas, L.G.F., Helena, M., Hollanda, B.M., Souza, L.C., Liu, D., 2013. Timing of the HT/LP transpression in the Neoproterozoic Seridó Belt (Borborema Province, Brazil): Constraints from U-Pb (SHRIMP) geochronology and implications for the connections between NE Brazil and West Africa. Gondwana Research 23, 701–714. https://doi.org/10.1016/j.gr.2012.05.005

Archanjo, C.J., Hollanda, M.H.B.M., Viegas, L.G.F., 2021. Late Ediacaran lateral-escape tectonics as recorded by the Patos shear zone (Borborema Province, NE Brazil). Brazilian Journal of Geology 51. https://doi.org/10.1590/2317-4889202120200132

Arthaud, M.H., Caby, R., Fuck, R.A., Dantas, E.L., Parente, C. V, 2008. Geology of the northern Borborema Province, NE Brazil and its correlation with Nigeria, NW Africa., West Gondwana: Pre-Cenozoic Correlations Across the South Atlantic Region. https://doi.org/10.1144/SP294.4

Arvidson, R.S., Beig, M.S., Luttge, A., 2004. Single-crystal plagioclase feldspar dissolution rates measured by vertical scanning interferometry. American Mineralogist 89, 51–56. https://doi.org/https://doi.org/10.2138/am-2004-0107

Behr, W.M., Platt, J.P., 2011. A naturally constrained stress profile through the middle crust in an extensional terrane. Earth and Planetary Science Letters 303, 181–192. https://doi.org/10.1016/j.epsl.2010.11.044

Baratoux, L., Schulmann, K., Ulrich, S., Lexa, O., 2005. Contrasting microstructures and deformation mechanisms in metagabbro mylonites contemporaneously

deformed under different temperatures (c. 650 °C and c. 750 °C). Geological Society Special Publication 243, 97–125. https://doi.org/10.1144/GSL.SP.2005.243.01.09

Behrmann, J.H., Mainprice, D., 1987. Deformation mechanisms in a high-temperature quartz-feldspar mylonite: evidence for superplastic flow in the lower continental crust. Tectonophysics 140, 297–305. https://doi.org/https://doi.org/10.1016/0040-1951(87)90236-8

Bestmann, M., Prior, D.J., 2003. Intragranular dynamic recrystallization in naturally deformed calcite marble: diffusion accommodated grain boundary sliding as a result of subgrain rotation recrystallization. 25, 1597–1613. https://doi.org/10.1016/S0191-8141(03)00006-3

Bons, P.D., Brok, B.D., 2000. Crystallographic preferred orientation development by dissolution-precipitation creep. Journal of Structural Geology 22, 1713–1722. https://doi.org/https://doi.org/10.1016/S0191-8141(00)00075-4

Burlini, L., Bruhn, D., 2005. High-strain zones: Laboratory perspectives on strain softening during ductile deformation. Geological Society Special Publication 245, 1–24. https://doi.org/10.1144/GSL.SP.2005.245.01.01

Caby, R., Arthaud, M.H., Archanjo, C.J., 1995. Lithostratigraphy and petrostructural characterization of supracrustal units in the Brasiliano Belt of Northeast Brazil: geodynamic implications. Journal of South American Earth Sciences 8, 235–246. https://doi.org/10.1016/0895-9811(95)00011-4

Cavalcante, G.C.G., Viegas, G., Archanjo, C.J., Egydio-Silva, M., 2016. The influence of partial melting and melt migration on the rheology of the continental crust. Journal of Geodynamics 101, 186–199. https://doi.org/10.1016/j.jog.2016.06.002

Ceccato, A., Menegon, L., Pennacchioni, G., Morales, L.F.G., 2018. Myrmekite and strain weakening in granitoid mylonites. Solid Earth 9, 1399–1419. https://doi.org/10.5194/se-9-1399-2018

Chakraborty, S., Majumdar, A.S., Shukla, A.D., 2020. Role of fluid in strain softening within the Main Central thrust in Sikkim: The origin of quartz-rich mylonites. Journal of Structural Geology 140, 104145. https://doi.org/10.1016/j.jsg.2020.104145

Corsini, M., Vauchez, A., Archanjo, C., de Sá, E.F.J., 1991. Strain transfer at continental scale from a transcurrent shear zone to a transpressional fold belt: The Patos-Seridó system, northeastern Brazil. Geology 19, 586–589. https://doi.org/https://doi.org/10.1130/0091-7613(1991)019<0586:STACSF>2.3.CO;2

Corsini, M., Vauchez, A., Caby, R., 1996. Ductile duplexing at a bend of a continental-scale strike-slip shear zone: Example from NE Brazil example from NE Brazil. Journal of Structural Geology 18, 385–394. https://doi.org/10.1016/0191-8141(95)00102-j

Corsini, M., Figueiredo, L.L., Caby, R., Féraud, G., Ruffet, G., Vauchez, A., 1998. Thermal history of the Pan-African / Brasiliano Borborema Province of northeast Brazil deduced from 40Ar / 39Ar analysis Thermal history of the Pan-African / Brasiliano Borborema Province of northeast Brazil deduced from 49Ar/39Ar analysis. 285, 103–117. https://doi.org/10.1016/S0040-1951(97)00192-3

Costa, A. P., Cavalcante, R., Dantas, A. R., Cunha, A. C., Bittencourt, R. C., Spisila, A. L., 2018. Mapa geológico Provincia Mineral do Seridó: estados da Paraíba e Rio Grande do Norte. Brazilian Geological Survey (CPRM), scale 1:350,000.

Cross, A.J., Kidder, S., Prior, D.J., 2015. Using microstructures and TitaniQ thermobarometry of quartz sheared around garnet porphyroclasts to evaluate microstructural evolution and constrain an Alpine Fault zone geotherm. Journal of Structural Geology. https://doi.org/10.1016/j.jsg.2015.02.012

Cross, A.J., Prior, D.J., Stipp, M., Kidder, S., 2017. The recrystallized grain size piezometer for quartz: An EBSD-based calibration. Geophysical Research Letters 44, 6667–6674. https://doi.org/10.1002/2017GL073836

Cross, A.J., Olree, E., Couvy, H., Skemer, P., 2020. How Does Viscosity Contrast Influence Phase Mixing and Strain Localization? Journal of Geophysical Research: Solid Earth 125. https://doi.org/10.1029/2020JB020323

Czaplińska, D., Piazolo, S., Zibra, I., 2015. The influence of phase and grain size distribution on the dynamics of strain localization in polymineralic rocks. Journal of Structural Geology 72, 15–32. https://doi.org/10.1016/j.jsg.2015.01.001

De Brito Neves, B.B., Dos Santos, E.J., Fuck, R.A., Santos, L.C.M.L., 2016. A preserved early Ediacaran magmatic arc at the northernmost portion of the Transversal Zone central subprovince of the Borborema Province, Northeastern South America. Brazilian Journal of Geology 46, 491–508. https://doi.org/10.1590/2317-4889201620160004

Deer, W.A., Howie, R.A., Zussman, J., 1992. An Introduction to the Rock-forming Minerals, second ed. Longman Scientific & Technical, Harlow, Essex, New York.

Dell' Angelo, L.N., Tullis, J., 1996. Textural and mechanical evolution with progressive strain in experimentally deformed aplite. Tectonophysics 256, 57–82. https://doi.org/https://doi.org/10.1016/0040-1951(95)00166-2

Dell'Angelo, L.N., Tullis, J., 1986. A comparison of quartz c-axis preferred orientations in experimentally deformed aplites and quartzites. Journal of Structural Geology 8, 683–692. https://doi.org/10.1016/0191-8141(86)90073-8

Dong, Y., Cao, S., Cheng, X., Liu, J., Cao, H., 2019. Grain-size reduction of feldspar and flow of deformed granites within the Gaoligong shear zone, southwestern Yunnan, China. Science China Earth Sciences 62. https://doi.org/https://doi.org/10.1007/s11430-018-9351-8

Eggleton, R.A., Buseck, P.R., 1980. The orthoclase-microcline inversion: A high-resolution transmission electron microscope study and strain analysis. Contributions to Mineralogy and Petrology 74, 123–133. https://doi.org/10.1007/BF01131998

Faghih, A., Soleimani, M., 2015. Quartz c-axis fabric development associated with shear deformation along an extensional detachment shear zone: Chapedony Metamorphic Core Complex, Central-East Iranian Microcontinent. Journal of Structural Geology 70, 1–11. https://doi.org/10.1016/j.jsg.2014.10.016

Faleiros, F.M., Moraes, R., Pavan, M., Campanha, G.A.C., 2016. Tectonophysics A new empirical calibration of the quartz c-axis fabric opening-angle deformation thermometer. Tectonophysics 671, 173–182. https://doi.org/10.1016/j.tecto.2016.01.014

Fitz Gerald, J.D., McLaren, A.C., 1982. The microstructures of microcline from some granitic rocks and pegmatites. Contributions to Mineralogy and Petrology 80, 219–229. https://doi.org/10.1007/BF00371351

Fitz Gerald, J.D., Stünitz, H., 1993. Deformation of granitoids at low metamorphic grade. I: Reactions and grain size reduction. 221, 269–297. https://doi.org/10.1016/0040-1951(93)90163-E

Fossen, H., Cavalcante, G.C.G., 2017. Shear zones – A review. Earth-Science Reviews 171, 434–455. https://doi.org/10.1016/j.earscirev.2017.05.002

Fukuda, J., Okudaira, T., Satsukawa, T., Michibayashi, K., 2012. Solution-precipitation of K-feldspar in deformed granitoids and its relationship to the distribution of water. Tectonophysics 532–535, 175–185. https://doi.org/10.1016/j.tecto.2012.01.033

Fukuda, J., Okudaira, T., 2013. Grain-size-sensitive creep of plagioclase accompanied by solution e precipitation and mass transfer under mid-crustal conditions. Journal of Structural Geology 51, 61–73. https://doi.org/10.1016/j.jsg.2013.03.006

Garlick, S.R., Gromet, L.P., 2004. Diffusion creep and partial melting in high temperature mylonitic gneisses, Hope Valley shear zone, New England Appalachians, USA. Journal of Metamorphic Geology 22, 45–62. https://doi.org/10.1111/j.1525-1314.2004.00496.x

Goncalves, P., Poilvet, J.C., Oliot, E., Trap, P., Didier, M., 2016. How does shear zone nucleate? An example from the Suretta nappe (Swiss Eastern Alps). Journal of Structural Geology 86, 166–180. https://doi.org/10.1016/j.jsg.2016.02.015

Hackspacher, P.C., Dantas, E.L., Brito Neves, B.B., Legrand, J.M., 1997. Northwestern Overthrusting and Related Lateral Escape During the Brasiliano Orogeny North of the Patos Lineament, Borborema Province, Northeast Brazil. International Geology Review 39, 609–620. https://doi.org/10.1080/00206819709465291

Handy, M.R., 1990. The solid-state flow of polymineralic rocks. Journal of Geophysical Research 95, 8647–8661. https://doi.org/10.1029/JB095iB06p08647

Handy, M.R., 1994. Flow laws for rocks containing two non-linear viscous phases: a phenomenological approach. Journal of Structural Geology 16, 287–301. https://doi.org/https://doi.org/10.1016/0191-8141(94)90035-3

Hansen, L.N., Zimmerman, M.E., Kohlstedt, D.L., 2012. The influence of microstructure on deformation of olivine in the grain-boundary sliding regime. Journal of Geophysical Research: Solid Earth 117. https://doi.org/10.1029/2012JB009305

Harrison, T.M., 1982. Diffusion of 40Ar in hornblende. Contributions to Mineralogy and Petrology 78, 324–331. https://doi.org/10.1007/BF00398927

Heidelbach, F., Post, A., Tullis, J., 2000. Crystallographic preferred orientation in albite samples deformed experimentally by dislocation and solution precipitation creep. Journal of Structural Geology 22, 1649–1661. https://doi.org/10.1016/S0191-8141(00)00072-9

Heilbronner, R., Tullis, J., 2006. Evolution of c axis pole figures and grain size during dynamic recrystallization: Results from experimentally sheared quartzite. Journal of Geophysical Research: Solid Earth 111, 1–19. https://doi.org/10.1029/2005JB004194

Hentschel, F., Trepmann, C.A., Janots, E., 2019. Deformation of feldspar at greenschist facies conditions-the record of mylonitic pegmatites from the Pfunderer Mountains, Eastern Alps. Solid Earth 10, 95–116. https://doi.org/10.5194/se-10-95-2019

Hirth, G., Tullis, J., 1992. Dislocation creep regimes in quartz aggregates. Journal of Structural Geology 14, 145–159. https://doi.org/10.1016/0191-8141(92)90053-Y

Hollanda, M.H.B.M., Archanjo, C.J., Laécio, C.S., Armstrong, R., Vasconcelos, P.M., 2010. Cambrian mafic to felsic magmatism and its connections with transcurrent shear zones of the Borborema Province (NE Brazil): Implications for the late assembly of the West Gondwana Precambrian Research Cambrian mafic to felsic magmatism and its connectio. Precambrian Research 178, 1–14. https://doi.org/10.1016/j.precamres.2009.12.004

Hollanda, M.H.B.M., Archanjo, C.J., Bautista, J.R., Souza, L.C., 2015. Detrital zircon ages and Nd isotope compositions of the Seridó and Lavras da Mangabeira basins (Borborema Province, NE Brazil): Evidence for exhumation and recycling associated with a major shift in sedimentary provenance. Precambrian Research 258, 186–207. https://doi.org/10.1016/j.precamres.2014.12.009

Holyoke, C.W., Tullis, J., 2006. Formation and maintenance of shear zones Formation and maintenance of shear zones. Geology 34, 105–108. https://doi.org/10.1130/G22116.1

Holyoke, C.W., Tullis, J., 2006. The interaction between reaction and deformation: An experimental study using a biotite + plagioclase + quartz gneiss. Journal of Metamorphic Geology 24, 743–762. https://doi.org/10.1111/j.1525-1314.2006.00666.x

Hunter, N.J.R., Hasalová, P., Weinberg, R.F., Wilson, C.J.L., 2016. Fabric controls on strain accommodation in naturally deformed mylonites: The influence of interconnected micaceous layers. Journal of Structural Geology 83, 180–193. https://doi.org/10.1016/j.jsg.2015.12.005

Ingles, J., Lamouroux, C., Soula, J.C., Guerrero, N., Debat, P., 1999. Nucleation of ductile shear zones in a granodiorite under greenschist facies conditions, Neouvielle massif, Pyrenees, France. Journal of Structural Geology 21, 555–576. https://doi.org/10.1016/S0191-8141(99)00042-5

Jessell, M.W., 1987. Grain-boundary migration microstructures in a naturally deformed quartzite. Journal of Structural Geology 9, 1007–1014. https://doi.org/https://doi.org/10.1016/0191-8141(87)90008-3

Jiang, Z., Prior, D.J., Wheeler, J., 2000. Albite crystallographic preferred orientation and grain misorientation distribution in a low-grade mylonite: Implications for granular flow. Journal of Structural Geology 22, 1663–1674. https://doi.org/10.1016/S0191-8141(00)00079-1

Jung, S., Yamamoto, T., Ando, J.I., Jung, H., 2021. Dislocation creep of olivine and amphibole in amphibole peridotites from Åheim, norway. Minerals 11. https://doi.org/10.3390/min11091018

Keller, L.M., Stipp, M., 2011. The single-slip hypothesis revisited: Crystal-preferred orientations of sheared quartz aggregates with increasing strain in nature and numerical simulation. Journal of Structural Geology 33, 1491–1500. https://doi.org/10.1016/j.jsg.2011.07.008

Kilian, R., Heilbronner, R., Stünitz, H., 2011. Quartz grain size reduction in a granitoid rock and the transition from dislocation to diffusion creep. Journal of Structural Geology 33, 1265–1284. https://doi.org/10.1016/j.jsg.2011.05.004

Kilian, R., 2015. Subgrain boundaries and slip systems in quartz. Geophysical Research Abstracts EGU General Assembly 17, 2015–12758.

Kilian, R., Heilbronner, R., 2017. Analysis of crystallographic preferred orientations of experimentally deformed Black Hills Quartzite. Solid Earth 8, 1095–1117.

Kruhl, J.H., 1996. Prism- and basal-plane parallel subgrain boundaries in quartz: a microstructural geothermobarometer. Journal of Metamorphic Geology 14, 581–589. https://doi.org/https://doi.org/10.1046/j.1525-1314.1996.00413.x

Kruse, R., Stünitz, H., Kunze, K., 2001. Dynamic recrystallization processes in plagioclase porphyroclasts. Journal of Structural Geology 23, 1781–1802. https://doi.org/https://doi.org/10.1016/S0191-8141(01)00030-X

Linckens, J., Herwegh, M., Mntener, O., Mercolli, I., 2011. Evolution of a polymineralic mantle shear zone and the role of second phases in the localization of deformation. Journal of Geophysical Research: Solid Earth 116, 1–21. https://doi.org/10.1029/2010JB008119

MacKenzie, W.S., 1954. The orthoclase-microcline inversion. Mineralogical Magazine and Journal of the Mineralogical Society 30, 354–366. https://doi.org/10.1180/minmag.1954.030.225.03

Mainprice, D., Bouchez, J., Blumenfeld, P., Tubià, J.M., 1986. Dominant c slip in naturally deformed quartz: Implications for dramatic plastic softening at high temperature. Geology 14, 819–822. https://doi.org/10.1130/0091-7613(1986)14<819:DCSIND>2.0.CO;2

Mainprice, D., Bachmann, F., Hielscher, R., Schaeben, H., 2015. Descriptive tools for the analysis of texture projects with large datasets using MTEX: Strength, symmetry and components. Geological Society Special Publication 409, 251–271. https://doi.org/10.1144/SP409.8

Mansard, N., Stünitz, H., Raimbourg, H., Précigout, J., 2020. The role of deformation-reaction interactions to localize strain in polymineralic rocks: Insights from experimentally deformed plagioclase-pyroxene assemblages. Journal of Structural Geology 134. https://doi.org/10.1016/j.jsg.2020.104008

Marshall, D.B., McLaren, A.C., 1977. Deformation Mechanisms in Experimentally Deformed Plagioclase Feldspars. Physics and Chemistry of Minerals 1, 351–370. https://doi.org/10.1002/pssa.2210410128

Marshall, D.B., McLaren, A.C., 1977. The direct observation and analysis of dislocations in experimentally deformed plagioclase feldspars. Journal of Materials Science 12, 893–903. https://doi.org/https://doi.org/10.1007/BF00540970

Medeiros, V. C., Amaral, C. A., Rocha, D. E. G. A., Santos, R. B., 2005. Programa Geologia do Brasil - PGB. Sousa. Folha SB.24-Z-A. Estados da Paraíba, Rio Grande do Norte e Ceará. Brazilian Geological Survey (CPRM), scale 1:250,000.

Mehl, L., Hirth, G., 2008. Plagioclase preferred orientation in layered mylonites: Evaluation of flow laws for the lower crust. Journal of Geophysical Research 113, 1–19. https://doi.org/10.1029/2007JB005075

Menegon, L., Pennacchioni, G., Stünitz, H., 2006. Nucleation and growth of myrmekite during ductile shear deformation in metagranites. Journal of Metamorphic Geology 24, 553–568. https://doi.org/10.1111/j.1525-1314.2006.00654.x

Menegon, L., Pennacchioni, G., Heilbronner, R., Pittarello, L., 2008. Evolution of quartz microstructure and c-axis crystallographic preferred orientation within ductilely deformed granitoids (Arolla unit, Western Alps). Journal of Structural Geology 30, 1332–1347. https://doi.org/10.1016/j.jsg.2008.07.007

Menegon, L., Pennacchioni, G., Spiess, R., 2008. Dissolution-precipitation creep of K-feldspar in mid-crustal granite mylonites. Journal of Structural Geology 30, 565–579. https://doi.org/10.1016/j.jsg.2008.02.001

Menegon, L., Stünitz, H., Nasipuri, P., Heilbronner, R., Svahnberg, H., 2013. Transition from fracturing to viscous flow in granulite facies perthitic feldspar (Lofoten, Norway). Journal of Structural Geology 48, 95–112. https://doi.org/10.1016/j.jsg.2012.12.004

Miranda, E.A., Hirth, G., John, B.E., 2016. Microstructural evidence for the transition from dislocation creep to dislocation-accommodated grain boundary sliding in naturally deformed plagioclase. Journal of Structural Geology 92, 30–45. https://doi.org/10.1016/j.jsg.2016.09.002

Monié, P., Caby, R., Arthaud, M.H., 1997. The Neoproterozoic Brasiliano orogeny in northeast Brazil: 40Ar/39Ar and petrostructural data from Ceará. Precambrian Research 81, 241–264. https://doi.org/https://doi.org/10.1016/S0301-9268(96)00037-X

Neves, S.P., Vauchez, A., Archanjo, C.J., 1996. Shear zone-controlled magma emplacement or magma-assisted nucleation of shear zones? Insights from northeast Brazil. Tectonophysics 262, 349–364. https://doi.org/https://doi.org/10.1016/0040-1951(96)00007-8

Oliot, E., Goncalves, P., Marquer, D., 2010. Role of plagioclase and reaction softening in a metagranite shear zone at mid-crustal conditions (Gotthard Massif, Swiss Central Alps). Journal of Metamorphic Geology 28, 849–871. https://doi.org/10.1111/j.1525-1314.2010.00897.x

Oliot, E., Goncalves, P., Schulmann, K., Marquer, D., Lexa, O., 2014. Mid-crustal shear zone formation in granitic rocks: Constraints from quantitative textural and crystallographic preferred orientations analyses. Tectonophysics 612–613, 63–80. https://doi.org/10.1016/j.tecto.2013.11.032

Palheta, E. S. M.; Gomes, I. P.; Braga, I. F.; Rocha, J. M. A.; Besser, M. L.; Freire, D. P. C.; Filho, D. V; Holanda, J. L. R., 2019. Mapa Geológico Granjeiro-Cococi. Estado do Ceará. Brazilian Geological Survey (CPRM), scale 1:250,000.

Papeschi, S., Musumeci, G., 2019. Fluid-Assisted Strain Localization in Quartz at the Brittle/Ductile Transition. Geochemistry, Geophysics, Geosystems 20, 3044–3064. https://doi.org/10.1029/2019GC008270

Passchier, C.W., Trouw, R.A.J., 2005. Microtectonics, second ed. Springer-verlag, Berlin, Heidelberg.

Platt, J.P., 2015. Rheology of two-phase systems: A microphysical and observational approach. Journal of Structural Geology 77, 213–227. https://doi.org/http://dx.doi.org/10.1016/j.jsg.2015.05.003

Platt, J.P., Behr, W.M., 2011. Grainsize evolution in ductile shear zones: Implications for strain localization and the strength of the lithosphere. Journal of Structural Geology 33, 537–550. https://doi.org/10.1016/j.jsg.2011.01.018

Pryer, L.L., 1993. Microstructures in feldspars from a major crustal thrust zone: the Grenville Front, Ontario, Canada. Journal of Structural Geology 15, 21–36.

Ree, J., Kim, H.S., Han, R., Jung, H., 2005. Grain-size reduction of feldspars by fracturing and neocrystallization in a low-grade granitic mylonite and its rheological effect. Tectonophysics 407, 227–237. https://doi.org/10.1016/j.tecto.2005.07.010

Sacerdoti, M., Labernadière, H., Gandais, M., 1980. Transmission electron microscope (TEM) study of geologically deformed potassic feldspars. Bulletin de Minéralogie 103, 148–155. https://doi.org/10.3406/bulmi.1980.7388

Satsukawa, T., Ildefonse, B., Mainprice, D., Morales, L.F.G., Michibayashi, K., Barou, F., 2013. A database of plagioclase crystal preferred orientations (CPO) and microstructures-implications for CPO origin, strength, symmetry and seismic anisotropy in gabbroic rocks. Solid Earth 4, 511–542. https://doi.org/10.5194/se-4-511-2013

Scandale, E., Gandais, M., Willaime, C., 1983. Transmission Electron Microscopic Study of Experimentally Deformed K-Feldspar Single Crystals. Physics and Chemistry of Minerals 9, 182–187. https://doi.org/https://doi.org/10.1007/BF00308376

Schulmann, K., Mlčoch, B., Melka, R., 1996. High-temperature microstructures and rheology of deformed granite, Erzgebirge, Bohemian Massif. Journal of Structural Geology 18, 719–733. https://doi.org/10.1016/S0191-8141(96)80007-1

Segall, P., Simpson, C., 1986. Nucleation of ductile shear zones on dilatant fractures. Geology 14, 56–59. https://doi.org/10.1130/0091-7613(1986)14<56:NODSZO>2.0.CO;2

Shaocheng, J, Mainprice, D., 1990. Recrystallization and fabric development in plagioclase. Journal of Geology 98, 65–79. https://doi.org/10.1086/629375

Shigematsu, N., 1999. Dynamic recrystallization in deformed plagioclase during progressive shear deformation. Tectonophysics 305, 437–452. https://doi.org/10.1016/S0040-1951(99)00039-6

Shigematsu, N., Prior, D.J., Wheeler, J., 2006. First combined electron backscatter diffraction and transmission electron microscopy study of grain boundary structure of deformed quartzite. Journal of Microscopy 224, 306–321. https://doi.org/10.1111/j.1365-2818.2006.01697.x

Simpson, C., 1985. Deformation of granitic rocks across the brittle-ductile transition. Journal of Structural Geology 7, 503–511. https://doi.org/https://doi.org/10.1016/0191-8141(85)90023-9

Simpson, C., Wintsch, R.P., 1989. Evidence for deformation-induced K-feldspar replacement by myrmekite. Journal of Metamorphic Geology 7, 261–275. https://doi.org/10.1111/j.1525-1314.1989.tb00588.x

Skemer, P., Katayama, I., Jiang, Z., Karato, S., 2005. The misorientation index: Development of a new method for calculating the strength of lattice-preferred

orientation. Tectonophysics 411, 157–167. https://doi.org/10.1016/j.tecto.2005.08.023

Stünitz, H., Tullis, J., 2001. Weakening and strain localization produced by syn-deformational reaction of plagioclase. International Journal of Earth Sciences 90, 136–148. https://doi.org/10.1007/s005310000148

Stünitz, H., Fitz Gerald, J.D., Tullis, J., 2003. Dislocation generation, slip systems, and dynamic recrystallization in experimentally deformed plagioclase single crystals. Tectonophysics 372, 215–233. https://doi.org/10.1016/S0040-1951(03)00241-5

Stipp, M., Stünitz, H., Heilbronner, R., Schmid, S.M., 2002. The eastern Tonale fault zone: A “natural laboratory” for crystal plastic deformation of quartz over a temperature range from 250 to 700 °C. Journal of Structural Geology 24, 1861–1884. https://doi.org/10.1016/S0191-8141(02)00035-4

Svahnberg, H., Piazolo, S., 2010. The initiation of strain localisation in plagioclase-rich rocks: Insights from detailed microstructural analyses. Journal of Structural Geology 32, 1404–1416. https://doi.org/10.1016/j.jsg.2010.06.011

Tokle, L., Hirth, G., Behr, W.M., 2019. Flow laws and fabric transitions in wet quartzite. Earth and Planetary Science Letters 505, 152–161. https://doi.org/10.1016/j.epsl.2018.10.017

Tsurumi, J., Hosonuma, H., Kanagawa, K., 2003. Strain localization due to a positive feedback of deformation and myrmekite-forming reaction in granite and aplite mylonites along the Hatagawa Shear Zone of NE Japan. Journal of Structural Geology 25, 557–574. https://doi.org/10.1016/S0191-8141(02)00048-2

Tullis, J., 1983. Deformation of Feldspars. In: Ribbe, P.H. (Ed.), Feldspar Mineralogy (Reviews in Mineralogy & Geochemistry). De Gruyter, Berlin, Boston, 297–324. https://doi.org/https://doi.org/10.1515/9781501508547-018

Tullis, J., 2002. Deformation of Granitic Rocks: Experimental Studies and Natural Examples. Reviews in Mineralogy and Geochemistry 51, 51–95. https://doi.org/https://doi.org/10.2138/gsrmg.51.1.51

Tullis, J., Yund, R.A., 1987. Transition from cataclastic flow to dislocation creep of feldspar: mechanisms and microstructures. Geology 15, 606–609. https://doi.org/10.1130/0091-7613(1987)15<606:TFCFTD>2.0.CO;2

Van Schmus, W.R., Oliveira, E.P., Da Silva Filho, A.F., Toteu, S.F., Penaye, J., Guimarães, I.P., 2008. Proterozoic links between the Borborema Province, NE Brazil, and the Central African Fold Belt. In: Pankhurst, R.J., Trouw, R.A.J., Brito Neves, B.B., De Wit, M.J. (Eds.), West Gondwana: Pre-Cenozoic Correlations Across the

South Atlantic Region (Special Publications). Geological Society of London, London, 69–99. https://doi.org/https://doi.org/10.1144/SP294.5

Van Schmus, W.R., Kozuch, M., Brito Neves, B.B., 2011. Precambrian history of the Zona Transversal of the Borborema Province, NE Brazil: Insights from Sm-Nd and U-Pb geochronology. Journal of South American Earth Sciences 31, 227–252. https://doi.org/10.1016/j.jsames.2011.02.010

Vauchez, A., Neves, S., Caby, R., Corsini, M., Egydio-Silva, M., Arthaud, M., Amaro, V., 1995. The Borborema shear zone system, NE Brazil. Journal of South American Earth Sciences 8, 247–266. https://doi.org/https://doi.org/10.1016/0895-9811(95)00012-5

Vernon, R.H., 1991. Questions about myrmekite in deformed rocks. Journal of Structural Geology 13, 979–985. https://doi.org/10.1016/0191-8141(91)90050-S

Vernon, R., Johnson, S., 2000. Transition from gneiss to migmatite and the relationship of leucosome to peraluminous granodiorite, Cooma Complex. Journal of the Virtual Explorer 2. https://doi.org/10.3809/jvirtex.2000.00021

Viegas, L.G.F., Archanjo, C.J., Vauchez, A., 2013. Fabrics of migmatites and the relationships between partial melting and deformation in high-grade transpressional shear zones: The Espinho Branco anatexite (Borborema Province, NE Brazil). Journal of Structural Geology 48, 45–56. https://doi.org/10.1016/j.jsg.2012.12.008

Viegas, L.G.F., Archanjo, C.J., Hollanda, M.H.B.M., Vauchez, A., 2014. Microfabrics and zircon U-Pb (SHRIMP) chronology of mylonites from the Patos shear zone (Borborema Province, NE Brazil). Precambrian Research 243, 1–17. https://doi.org/10.1016/j.precamres.2013.12.020

Yang, R., Jiang, D., Lu, L.X., 2019. Constrictional Strain and Linear Fabrics as a Result of Deformation Partitioning: A Multiscale Modeling Investigation and Tectonic Significance. Tectonics 38, 2829–2849. https://doi.org/10.1029/2019TC005490

Waldron, K., Parsons, I., Brown, W.L., 1993. Solution-redeposition and the orthoclase-microcline transformation: evidence from granulites and relevance to 18 O exchange. Mineralogical Magazine 57, 687–695. https://doi.org/10.1180/minmag.1993.057.389.13

Warren, J.M., Hirth, G., 2006. Grain size sensitive deformation mechanisms in naturally deformed peridotites. Earth and Planetary Science Letters 248, 438–450. https://doi.org/10.1016/j.epsl.2006.06.006

Wehrens, P., Baumberger, R., Berger, A., Herwegh, M., 2017. How is strain localized in a meta-granitoid, mid-crustal basement section? Spatial distribution of deformation

in the central Aar massif (Switzerland). Journal of Structural Geology 94, 47–67. https://doi.org/10.1016/j.jsg.2016.11.004

Whitney, D.L., Evans, B.W., 2010. Abbreviations for names of rock-forming minerals. American Mineralogist 95, 185–187. https://doi.org/10.2138/am.2010.3371

Willaime, C., Gandais, M., 1977. Electron microscope study of plastic defects in experimentally deformed alkali feldspars. Bulletin de La Société Française de Minéralogie et de Cristallographie 100, 263–271. https://doi.org/10.3406/bulmi.1977.7147

Willaime, C., Christie, J.M., Kovacs, M.P., 1979. Experimental deformation of K-feldspar single crystals. Bulletin de Minéralogie 102, 168–177. https://doi.org/10.1130/0016-7606(1959)70[245:EDODSC]2.0.CO;2

Wintsch, R.P., Yi, K., 2002. Dissolution and replacement creep: a significant deformation mechanism in mid-crustal rocks. Journal of Structural Geology 24, 1179–1193. https://doi.org/https://doi.org/10.1016/S0191-8141(01)00100-6

Závada, P., Schulmann, K., Konopásek, J., Ulrich, S., Lexa, O., 2007. Extreme ductility of feldspar aggregates - Melt-enhanced grain boundary sliding and creep failure: Rheological implications for felsic lower crust. Journal of Geophysical Research: Solid Earth 112, 1–15. https://doi.org/10.1029/2006JB004820

Zibra, I., White, J.C., Menegon, L., Dering, G., Gessner, K., 2018. The ultimate fate of a synmagmatic shear zone. Interplay between rupturing and ductile flow in a cooling granite pluton. Journal of Structural Geology 110, 1–23. https://doi.org/10.1016/j.jsg.2018.02.001

6 CONSIDERAÇÕES FINAIS E RECOMENDAÇÕES

Os resultados apresentados neste trabalho se somam àqueles apresentados por trabalhos préviso no que diz respeito a compreensão dos processos que levaram a acomodação e a localização da deformação na zona de cisalhamento Patos. As conclusões chegadas neste estudo apontam uma deformação heterogênea, dinamicante particionada e acomodada nos domínios reólogicos menos competentes devido ao contraste de viscosidade entre as camadas dos metatexitos na macroescala e entre as fases na microescala. Os agentes de tal enfraquecimento variam conforme as condições de temperatura da deformação, sendo filossilicatos e a criação de OCPs durante a deformação em altas temperaturas e na presença de material fundido (>700°C), interconeccção de filossilicatos e formação de agregados

recristalizados finos durante deformações sob temperaturas medianas (450-550°C), ocasionando uma mudança de mecanismos insensíveis para mecanismos sensíveis ao tamanho do grão que acomodam grande parte da deformação em zonas localizadas, e descontinuidades mecânicas na micro e na macroescala e influxo de fluidos durante deformações em baixas temperaturas (<400°C).

Como consequência deste trabalho, também foi encontrado algumas inconsistências na literatura com relação a alguns sistemas de deslizamentos reportados tais como (100)[010] no feldspato alcalino e (021)[1-12] no plagioclásio. Isto mostra que as interpretações obtidas pela aplicação da técnica EBSD em minerais de baixa simetria ou que ocorrem como polimorfos, como o feldspato, deve ser feita com cautela, e corroboradas com auxílio de mais de um método analítico além do método de "orientação favorável ao sistema de deslizamento" (*easy slip system*) e utilizando como base os sistemas de deslizamento determinados a partir do microscópio eletrônico de transmissão em trabalhos prévios.

Ademais, é recomendado que os futuros trabalhos na ZCPa envolvam estudos paleo(geo)termobarométricos dos milonitos de alta a baixa temperatura, afim de determinar as condições de deformação (temperatura, pressão e fluidos) na qual atuaram os mecanismos de deformação observados, e assim correlacionar com as idades $^{40}Ar/^{39}Ar$ previamente reportadas da literatura de modo a construir modelos evolutivos mais robustos.

Para finalizar, a zona de cisalhamento Patos é uma estrutura fascinante e um verdadeiro laboratório natural que expõe belos afloramentos que compreendem milonitos formados sob diversas condições de deformação e preservados do intemperismo. Espera-se que este trabalho tenha contribuído de algum modo para o seu entendimento e também para colaborar com o e geral sobre a acomodação da deformação em zonas de cisalhamento.

7 REFERÊNCIAS BIBLIOGRÁFICAS

ALMEIDA, F. F. M.; HASUI, Y.; BRITO NEVES, B. B.; FUCK, R. A. Brazilian structural provinces. An introduction. **Earth Science Reviews**, v. 17, n. 1-2, P. 1-29, 1981.

ANGELIM, L. A. A.; VASCONCELOS, A. M.; GOMES, J. R. C.; WANDERLEY, A. A.; FORGIARINI, L. L.; MEDEIROS, M. F. 2004. Folha SB.24-Jaguaribe. In: C. Schobbenhaus; J. H. Gonçalves; J. O. S. Santos; M. B. Abram, R. Leão Neto; G. M.

M. Matos; R. M. Vidotti; M. A. B. Ramos; J. D. A. Jesus (Orgs.); **Carta Geológica do Brasil ao Milionésimo**, Sistema de Informações Geográficas-SIG, Programa Geologia do Brasil, CPRM, Brasília, CD-ROM.

ANGELIM, L. A. A.; VASCONCELOS, A. M.; GOMES, J. R. C.; WANDERLEY, A. A.; FORGIARINI, L. L.; MEDEIROS, M. F. 2004. Folha SB.24-Jaguaribe. In: C. Schobbenhaus; J. H. Gonçalves; J. O. S. Santos; M. B. Abram, R. Leão Neto; G. M. M. Matos; R. M. Vidotti; M. A. B. Ramos; J. D. A. Jesus (Orgs.); **Carta Geológica do Brasil ao Milionésimo**, Sistema de Informações Geográficas-SIG, Programa Geologia do Brasil, CPRM, Brasília, CD-ROM.

ASHBY, M. F.; VERRALL, R. A. Diffusion-accommodated flow and superplasticity. **Acta Metallurgica**, v. 21, n. 2, p. 149–163, 1973.

BARTH, N. C.; HACKER, B. R.; SEWARD, G. G. E. Strain within the ultrahigh-pressure Western Gneiss region of Norway recorded by quartz CPOs. In: R. D. Law; R. W. H. Butler; R. E. Holdsworth; M. Krabbendam; R. A. Strachan (Orgs.); **Continental Tectonics and Mountain Building: The Legacy of Peach and Horne**. v. 335, p. 663–685, 2010. London: The Geological Society of London.

BEHRMANN, J. H.; MAINPRICE, D. Deformation mechanisms in a high-temperature quartz-feldspar mylonite: evidence for superplastic flow in the lower continental crust. **Tectonophysics**, v. 140, n. 2–4, p. 297–305, 1987.

BONS, P. D.; BROK, B. D. Crystallographic preferred orientation development by dissolution-precipitation creep. **Journal of Structural Geology**, v. 22, n. 11–12, p. 1713–1722, 2000.

BRITO NEVES, B. B., SANTOS, E. J., VAN SCHMUS, W. R. Tectonic History of the Borborema Province, Northeastern Brazil. In: U.G. Cordani; E. J. Milani; A. Thomaz Filho; D. A. Campos (Orgs.); **Tectonic Evolution of South America**. p. 151-182, 2000. Rio de Janeiro: Sociedade Brasileira de Geologia.

BRITO NEVES, B. B.; VAN SCHMUS, W. R.; SANTOS, E. J.; CAMPOS NETO, M. C.; KOZUCH. M. O. Evento Cariris Velhos na Província Borborema: integração de dados, implicações e perspectivas. **Revista Brasileira de Geociências**, v.25, p. 279–296, 1995.

BUNGE, H. J. **Texture Analysis in Materials Science: Mathematical Methods**. 1º ed. London: Butterworth, 1982.

BUNGE, H. J. Zur Darstellung allgemeiner Texturen. ***Zeitschrift für Metallkunde**, v. 56, p. 872-874, 1965.*

BURLINI, L.; BRUHN, D. High-strain zones: Laboratory perspectives on strain softening during ductile deformation. In: D. Bruhn; L. Burlini (Orgs.); **Geological Society Special Publication**. v. 245, p. 1–24, 2005. London: Geological Society of London.

BURLINI, L.; BRUHN, D. High-strain zones: Laboratory perspectives on strain softening during ductile deformation. In: D. Bruhn; L. Burlini (Orgs.); **Geological Society Special Publication**. v. 245, p. 1–24, 2005. London: Geological Society of London.

CAVALCANTE, G. C. G.; VIEGAS, G.; ARCHANJO, C. J.; EGYDIO-SILVA, M. The influence of partial melting and melt migration on the rheology of the continental crust. **Journal of Geodynamics**, v. 101, p. 186–199, 2016.

CORSINI, M.; FIGUEIREDO, L. L.; CABY, R. Thermal history of the Pan-African / Brasiliano Borborema Province of northeast Brazil deduced from 40Ar / 39Ar analysis Thermal history of the Pan-African/Brasiliano, Borborema Province of northeast Brazil deduced from ^{40}Ar / ^{39}Ar analysis. **Tectonophysics**, v. 285, n. 1–2, p. 103–117, 1998.

CORSINI, M.; VAUCHEZ, A.; ARCHANJO, C.; DE SÁ, E. F. J. Strain transfer at continental scale from a transcurrent shear zone to a transpressional fold belt: The Patos-Seridó system, northeastern Brazil. **Geology**, v. 19, n. 6, p. 586–589, 1991.

CORSINI, M.; VAUCHEZ, A.; CABY, R. Ductile duplexing at a bend of a continental-scale strike-slip shear zone: Example from NE Brazil example from NE Brazil. **Journal of Structural Geology**, v. 18, n. 4, p. 385–394, 1996.

COSTA, A. P.; CAVALCANTE, R.; DANTAS, A. R.; CUNHA, A. C.; BITTENCOURT, R. C.; SPISILA, A. L. **Mapa geológico Provincia Mineral do Seridó: estados da Paraíba e Rio Grande do Norte.** Recife: CPRM – Serviço, Geológico do Brasil, 2018. 1 mapa color. 133 cm X 90 cm. Escala 1:350.000. Programa Geologia, Mineração e Transformação Mineral. Ação: Avaliação dos Recursos Minerais do Brasil.

CZAPLIŃSKA, D.; PIAZOLO, S.; ZIBRA, I. The influence of phase and grain size distribution on the dynamics of strain localization in polymineralic rocks. **Journal of Structural Geology**, v. 72, p. 15–32, 2015.

DANTAS, E. L. **Evolução tectono-magmática do maciço polidiapírico São Vicente/Florânia-RN**, 1992. Universidade Estadual de São Paulo - UNESP.

DANTAS, E. L. **Geocronologia U-Pb e Sm-Nd de terrenos arqueanos e paleoproterozóicos do Maciço Caldas Brandão, NE do Brasil**, 1996. Universidade Federal do Rio Grande do Norte - UFRN.

DE WIT, M. J.; STANKIEWICZ, J.; REEVES, C. Restoring Pan-African-Brasiliano connections: more Gondwana control, less Trans-Atlantic corruption. In: R. J. Pankhurst; R. A. J. Trouw; B. B. Brito Neves; M. J. De Wit (Orgs.); **West Gondwana: Pre-Cenozoic Correlations Across the South Atlantic Region**. 1º ed, v. 294, p. 399–412, 2008. London: Geological Society of London.

DELL'ANGELO, L. N.; TULLIS, J. Fabric development in experimentally sheared quartzites. **Tectonophysics**, v. 169, n. 1–3, p. 1–21, 1989.

DUNLAP, W. J. Neocrystallization or cooling? 40Ar/39Ar ages of white micas from low-grade mylonites. **Chemical Geology**, v. 143, n. 3–4, p. 181–203, 1997.

ETHERIDGE, M. A.; WILKIE, J. C. Grainsize reduction, grain boundary sliding and the flow strength of mylonites. **Tectonophysics**, v. 58, n. 1–2, p. 159–178, 1979.

EZZAHMOULY, M.; ELMOUTAOUAKKIL, A.; ED-DHAHRAOUY, M.; et al. Micro-computed tomographic and SEM study of porous bioceramics using an adaptive method based on the mathematical morphological operations. **Heliyon**, v. 5, n. 12, p. E02557, 2019.

FITZ GERALD, J. D.; STÜNITZ, H. Deformation of granitoids at low metamorphic grade. I: Reactions and grain size reduction. **Tectonophysics**, v. 221, n. 3–4, p. 269–297, 1993.

FOSSEN, H.; CAVALCANTE, G. C. G. Shear zones – A review. **Earth-Science Reviews**, v. 171, n. October, p. 434–455, 2017.

FRANĚK, J.; SCHULMAN, K.; LEXA, O. Kinematic and rheological model of exhumation of high pressure granulites in the Variscan orogenic root: Example of the Blanský les granulite, Bohemian Massif, Czech Republic. **Mineralogy and Petrology**, v. 86, n. 3–4, p. 253–276, 2006.

FUKUDA, J.; OKUDAIRA, T.; SATSUKAWA, T.; MICHIBAYASHI, K. Solution-precipitation of K-feldspar in deformed granitoids and its relationship to the distribution of water. **Tectonophysics**, v. 532–535, p. 175–185, 2012.

GOLDSTEIN, J. I.; NEWBURY, D. E.; MICHAEL, J. R. **Scanning Electron Microscopy and X-ray Microanalysis**. 4º ed. New York: Springer, 2018.

HACKSPACHER, P. C.; VAN SCHMUS, W. R.; DANTAS, E. L. Um embasamento transamazônico na Província Borborema. 36 Congresso Brasileiro de Geologia. **Anais**. V. 6, P. 2683-2696, 1990. Natal, Brasil.

HANDY, M. R. Flow laws for rocks containing two non-linear viscous phases: a phenomenological approach. **Journal of Structural Geology**, v. 16, n. 3, p. 287–301, 1994.

HANDY, M. R. The Solid-State Flow of Polymineralic Rocks. **Journal of Geophysical Research**, v. 95, n. B6, p. 8647–8661, 1990.

HASUI, Y.; CARNEIRO, C. D. R.; ALMEIDA, F. F. M.; BARTORELLI, A. **Geologia do brasil**. São Paulo: Beca, 2012.

HEIDELBACH, F.; POST, A.; TULLIS, J. Crystallographic preferred orientation in albite samples deformed experimentally by dislocation and solution precipitation creep. **Journal of Structural Geology**, v. 22, n. 11–12, p. 1649–1661, 2000.

HEILBRONNER, R.; TULLIS, J. Evolution of c axis pole figures and grain size during dynamic recrystallization: Results from experimentally sheared quartzite. **Journal of Geophysical Research: Solid Earth**, v. 111, n. 10, p. 1–19, 2006.

HENTSCHEL, F.; TREPMANN, C. A.; JANOTS, E. Deformation of feldspar at greenschist facies conditions-the record of mylonitic pegmatites from the Pfunderer Mountains, Eastern Alps. **Solid Earth**, v. 10, p. 95–116, 2019.

HIRTH, G.; TULLIS, J. Dislocation creep regimes in quartz aggregates. **Journal of Structural Geology**, v. 14, n. 2, p. 145–159, 1992.

HOBBS, B. E.; MEANS, W. D.; WILLIAMS, P. F. **An Outline of Structural Geology**. New York: John Wiley, 1976.

HULL, D.; BACON, D. J. **Introduction to dislocations**. fifth ed. Oxford: Elsevier Ltd, 2011.

ISHII, K.; KANAGAWA, K.; SHIGEMATSU, N.; OKUDAIRA, T. High ductility of K-feldspar and development of granitic banded ultramylonite in the Ryoke metamorphic belt, SW Japan. **Journal of Structural Geology**, v. 29, n. 6, p. 1083–1098, 2007.

JESSELL, M. W. Grain-boundary migration microstructures in a naturally deformed quartzite. **Journal of Structural Geology**, v. 9, n. 8, p. 1007–1014, 1987.

KELLER, L. M.; STIPP, M. The single-slip hypothesis revisited: Crystal-preferred orientations of sheared quartz aggregates with increasing strain in nature and numerical simulation. **Journal of Structural Geology**, v. 33, n. 10, p. 1491–1500, 2011.

KENIS, I.; URAI, J. L.; VAN DER ZEE, W.; HILGERS, C.; SINTUBIN, M. Rheology of fine-grained siliciclastic rocks in the middle crust - Evidence from structural and numerical analysis. **Earth and Planetary Science Letters**, v. 233, n. 3–4, p. 351–360, 2005.

KILIAN, R.; HEILBRONNER, R.; STÜNITZ, H. Quartz grain size reduction in a granitoid rock and the transition from dislocation to diffusion creep. **Journal of Structural Geology**, v. 33, n. 8, p. 1265–1284, 2011.

KRUHL, J. H. Preferred lattice orientations of plagioclase from amphibolite and greenschist facies rocks near the Insubric Line (Western Alps). **Tectonophysics**, v. 135, n. 1–3, p. 233–242, 1987.

KRUHL, J. H. Prism- and basal-plane parallel subgrain boundaries in quartz: a microstructural geothermobarometer. **Journal of Metamorphic Geology**, v. 14, n. 5, p. 581–589, 1996.

KRUHL, J. H. Prism- and basal-plane parallel subgrain boundaries in quartz: a microstructural geothermobarometer. **Journal of Metamorphic Geology**, v. 14, n. 5, p. 581–589, 1996.

LAW, R. D. Crystallographic fabrics: A selective review of their applications to research in structural geology. In: R. J. Knipe; E. H. Rutter (Orgs.); **Deformation Mechanisms, Rheology and Tectonics**. v. 54, p.335–352, 1990. London: Geological Society of London.

LEGRAND, J. M., LIEGEOIS, J. P.; DEUTSCH, S. Datações U/Pb e Rb/Sr das rochas precambrianas da região de Caicó. Reavaliação da definição de um embasamento arqueano, in 14 Simp. Geol. Nordeste: Fortaleza, Soc. Bras. Geol., p. 276-279, 1991.

LISTER, G. S.; HOBBS, B. E. The simulation of fabric development during plastic deformation and its application to quartzite: the influence of detormation history. **Journal of Structural Geology**, v. 2, n. 3, p. 355–370, 1980.

LISTER, G. S.; PATERSON, M. S.; HOBBS, B. E. The simulation of fabric development in plastic deformation and its application to quartzite: The model. **Tectonophysics**, v. 45, n. 2–3, p. 107–158, 1978.

LOPEZ-SANCHEZ, M. A.; LLANA-FÚNEZ, S. An evaluation of different measures of dynamically recrystallized grain size for paleopiezometry or paleowattometry studies. **Solid Earth**, v. 6, n. 2, p. 475–495, 2015.

MARIANI, E., PRIOR, D.J., MCNAMARA, D., PEARCE, M.A., SEATON, N., SEWARD, G.G.E., TATHAM, D.J., WHEELER, J. Electron back-scattered diffraction

(EBSD) in the SEM: applications to microstructures in minerals and rocks and recent technological advancements. In: Subias, I., Bauluz, B. (Orgs.), Instrumental Techniques Applied to Mineralogy and Geochemistry, Seminarios SEM 5, 7-19, 2009.

MARSHALL, D. B.; MCLAREN, A. C. Deformation Mechanisms in Experimentally Deformed Plagioclase Feldspars. **Physics and Chemistry of Minerals**, v. 1, p. 351–370, 1977.

MARSHALL, D. B.; MCLAREN, A. C. The direct observation and analysis of dislocations in experimentally deformed plagioclase feldspars. **Journal of Materials Science**, v. 12, p. 893–903, 1977b.

MARTELAT, J. E.; SCHULMANN, K.; LARDEAUX, J. M.; NICOLLET, C.; CARDON, H. Granulite microfabrics and deformation mechanisms in southern Madagascar. **Journal of Structural Geology**, v. 21, n. 6, p. 671–687, 1999.

MCCLAY, K. R. Pressure solution and Coble creep in rocks and minerals: A review. **Journal of the Geological Society**, v. 134, n. 1, p. 57–70, 1977.

MEDEIROS, V. C., AMARAL, C. A., ROCHA, D. E. G. A., SANTOS, R. B. 2005. Programa Geologia do Brasil - PGB. Sousa. Folha SB.24-Z-A. Estados da Paraíba, Rio Grande do Norte e Ceará. Mapa Geológico. Recife: CPRM, 2005, 1 mapa, color., 66cm x 108cm. Escala 1:250.000.

MEHL, L.; HIRTH, G. Plagioclase preferred orientation in layered mylonites: Evaluation of flow laws for the lower crust. **Journal of Geophysical Research**, v. 113, n. B5, p. 1–19, 2008.

MENEGON, L.; PENNACCHIONI, G.; HEILBRONNER, R.; PITTARELLO, L. Evolution of quartz microstructure and c-axis crystallographic preferred orientation within ductilely deformed granitoids (Arolla unit, Western Alps). **Journal of Structural Geology**, v. 30, n. 11, p. 1332–1347, 2008.

MENEGON, L.; PENNACCHIONI, G.; SPIESS, R. Dissolution-precipitation creep of K-feldspar in mid-crustal granite mylonites. **Journal of Structural Geology**, v. 30, n. 5, p. 565–579, 2008.

MENEGON, L.; STÜNITZ, H.; NASIPURI, P.; HEILBRONNER, R.; SVAHNBERG, H. Transition from fracturing to viscous flow in granulite facies perthitic feldspar (Lofoten, Norway). **Journal of Structural Geology**, v. 48, p. 95–112, 2013.

MIRANDA, E. A.; HIRTH, G.; JOHN, B. E. Microstructural evidence for the transition from dislocation creep to dislocation-accommodated grain boundary sliding in

naturally deformed plagioclase. **Journal of Structural Geology**, v. 92, p. 30–45, 2016.

MONIÉ, P.; CABY, R.; ARTHAUD, M. H. The Neoproterozoic Brasiliano orogeny in northeast Brazil: $^{40}Ar/^{39}Ar$ and petrostructural data from Ceará. **Precambrian Research**, v. 81, n. 3–4, p. 241–264, 1997.

MUKAI, H.; AUSTRHEIM, H.; PUTNIS, C. V.; PUTNIS, A. Textural evolution of plagioclase feldspar across a shear zone: Implications for deformation mechanism and rock strength. **Journal of Petrology**, v. 55, n. 8, p. 1457–1477, 2014.

NEVES, S. P. Proterozoic history of the Borborema province (NE Brazil): Correlations with neighboring cratons and Pan-African belts and implications for the evolution of western Gondwana. **Tectonics**, v. 22, n. 4, p. 1031, 2003.

NEVES, S. P.; VAUCHEZ, A.; FERAUD, G. Tectono-thermal evolution, magma emplacement, and shear zone development in the Caruaru area (Borborema Province, NE Brazil)., v. 99, p. 1–32, 2000.

OLAF, E.; RANDLE, V. **Introduction to TEXTURE ANALYSIS: Macroexture, Microtexture, and Orientation Mapping**. 2º ed. Boca Raton: CRC Press, 2010.

OLIOT, E.; GONCALVES, P.; SCHULMANN, K.; MARQUER, D.; LEXA, O. Mid-crustal shear zone formation in granitic rocks: Constraints from quantitative textural and crystallographic preferred orientations analyses. **Tectonophysics**, v. 612–613, p. 63–80, 2014.

OLSEN, T. S.; KOHLSTEDT, D. L. Analysis of dislocations in some naturally deformed plagioclase feldspars. **Physics and Chemistry of Minerals**, v. 11, n. 4, p. 153–160, 1984.

OLSEN, T. S.; KOHLSTEDT, D. L. Analysis of dislocations in some naturally deformed plagioclase feldspars. **Physics and Chemistry of Minerals**, v. 11, n. 4, p. 153–160, 1984.

PALHETA, E. S. M.; GOMES, I. P.; BRAGA, I. F.; ROCHA, J. M. A.; BESSER, M. L.; FREIRE, D. P. C.; FILHO, D. V; HOLANDA, J. L. R. Mapa Geológico Granjeiro-Cococi. Estado do Ceará. Fortaleza: CPRM, 2019. 1 mapa color., 150 x 90 cm. Escala 1:250.000. Projeto Granjeiro Cococi.

PASSCHIER, C. W.; TROUW, R. A. J. **Microtectonics**. 2º ed. Berlin, Heidelberg: Springer, 2005.

PETTA, A. R. Estudo geoquímico e relações petrogenéticas do batólito múltiplo composto São Vicente/Caicó (RNBrasil). 1995. 304 p. Tese (Doutorado) - Instituto de Geociências e Ciências Exatas, Universidade Estadual Paulista, Rio Claro, 1995.

PLATT, J. P. Rheology of two-phase systems: A microphysical and observational approach. **Journal of Structural Geology**, v. 77, p. 213–227, 2015.

POIRIER, J. P. **Creep of crystals: High-temperature deformation processes in metals, ceramics and minerals (Cambridge Earth Science Series)**. Cambridge: Cambridge University Press, 1985.

POIRIER, J. P.; GUILLOPÉ, M. Deformation induced recrystallization of minerals. **Bulletin de Minéralogie**, v. 102, n. 2–3, p. 67–74, 1979.

PRIOR, D. J.; BOYLE, A. P.; BRENKER, F. The application of electron backscatter diffraction and orientation contrast imaging in the SEM to textural problems in rocks. **American Mineralogist**, v. 84, n. 11–12, p. 1741–1759, 1999.

RAMSAY, J. G. Shear zone geometry: A review. **Journal of Structural Geology**, v. 2, n. 1–2, p. 83–99, 1980.

RANDLE, V. **MICROTEXTURE DETERMINATION and its applications**. 2º ed. London: Institute of Materials, Minerals and Mining, 2008.

RUTTER, E. H.; BRODIE, K. H. The role of tectonic grain size reduction in the rheological stratification of the lithosphere. **Geologische Rundschau**, v. 77, n. 1, p. 295–308, 1988.

SACERDOTI, M.; LABERNADIÈRE, H.; GANDAIS, M. Transmission electron microscope (TEM) study of geologically deformed potassic feldspars. **Bulletin de Minéralogie**, v. 103, n. 1, p. 148–155, 1980.

SATSUKAWA, T.; ILDEFONSE, B.; MAINPRICE, D. A database of plagioclase crystal preferred orientations (CPO) and microstructures-implications for CPO origin, strength, symmetry and seismic anisotropy in gabbroic rocks. **Solid Earth**, v. 4, n. 2, p. 511–542, 2013.

SCANDALE, E.; GANDAIS, M.; WILLAIME, C. Transmission Electron Microscopic Study of Experimentally Deformed K-feldspar Single Crystals. **Physics and Chemistry of Minerals**, v. 9, p. 182–187, 1983.

SCHULMANN, K.; MLČOCH, B.; MELKA, R. High-temperature microstructures and rheology of deformed granite, Erzgebirge, Bohemian Massif. **Journal of Structural Geology**, v. 18, n. 6, p. 719–733, 1996.

SCHWARZER, R.A.; FIELD, D.P.; ADAMS, B.L.; KUMAR, M.; SCHWARTZ, A.J. Present state of electron backscatter diffraction and prospective developments. In: A. J. Schwartz; M. Kumar; B. L. Adams; D. P. Field (Orgs.); **Electron Backscatter Diffraction in Materials Science**. p. 1–20, 2009. Berlin: Springer.

SHAOCHENG, J.; DAVID, M. Natural deformation fabrics of plagioclase: implications for slip systems and seismic anisotropy. **Tectonophysics**, v. 147, n. 1–2, p. 145–163, 1988.

SIBSON, R. H. Fault rocks and fault mechanisms. **Journal of the Geological Society**, v. 133, n. 3, p. 191–213, 1977.

SOUZA, Z. S.; MARTIN, H.; MACEDO, M. H. F.; PEUCAT, J. J.; JARDIM DE SÁ, E. F. Um segment de **croûte continentale juvenile** d'***âge protérozoïque inférieur: le Complexe de Caicó (Rio Grande do Norte, NE-Brésil). Comptes Rendus de l'Académie des Sciences, v. 316, n. 3, p. 201-208, 1993.***

STIPP, M.; STÜNITZ, H.; HEILBRONNER, R.; SCHMID, S. M. The eastern Tonale fault zone: A "natural laboratory" for crystal plastic deformation of quartz over a temperature range from 250 to 700 °C. **Journal of Structural Geology**, v. 24, n. 12, p. 1861–1884, 2002.

STIPP, M.; STÜNITZ, H.; HEILBRONNER, R.; SCHMID, S. M. The eastern Tonale fault zone: A "natural laboratory" for crystal plastic deformation of quartz over a temperature range from 250 to 700 °C. **Journal of Structural Geology**, v. 24, n. 12, p. 1861–1884, 2002.

STÜNITZ, H.; FITZ GERALD, J. D.; TULLIS, J. Dislocation generation, slip systems, and dynamic recrystallization in experimentally deformed plagioclase single crystals. **Tectonophysics**, v. 372, n. 3–4, p. 215–233, 2003.

SVAHNBERG, H.; PIAZOLO, S. The initiation of strain localisation in plagioclase-rich rocks: Insights from detailed microstructural analyses. **Journal of Structural Geology**, v. 32, n. 10, p. 1404–1416, 2010.

TRIMBY, P. W.; PRIOR, D. J.; WHEELER, J. Grain boundary hierarchy development in a quartz mylonite. **Journal of Structural Geology**, v. 20, n. 7, p. 917–935, 1998.

TULLIS, J. Deformation of Feldspars. In: P. H. Ribbe (Org.); **Feldspar Mineralogy (reviews in Mineralogy & Geochemistry)**. v. 2, p. 297–324, 1983. Berlin, Boston: De Gruyter.

TULLIS, J. Deformation of Granitic Rocks: Experimental Studies and Natural Examples. In: S. I. Karato; H. R. Wenk (Orgs.); **Plastic Deformation of Minerals**

and Rocks (Reviews in Mineralogy and Geochemistry). v. 51, p. 51–95, 2002. Berlin, Boston: De Gruyter.

TULLIS, J.; YUND, R. A. Transition from cataclastic flow to dislocation creep of feldspar: mechanisms and microstructures. **Geology**, v. 15, n. 7, p. 606–609, 1987.

TWISS, R. J.; MOORES, E. M. **Structural Geology**. 2º ed. New York: W. H. Freeman, 2007.

URAI, J. L.; MEANS, W. D.; LISTER, G. S. Dynamic recrystallization of minerals. In: B. E. Hobbs; H. C. Heard (Orgs.); **Mineral and Rock Deformation: Laboratory Studies (Geophysical Monograph Series)**. v. 36, p. 161–199, 1986. Washington DC: American Geophysical Union.

VAN DER PLUIJM, B. A.; MARSHAK, S. **Earth Structure: An Introduction to Structural Geology and Tectonics**. 2º ed. New York: W. W. Norton, 2004.

VAN SCHMUS, W. R.; OLIVEIRA, E. P.; DA SILVA FILHO, A. F. Proterozoic links between the Borborema Province, NE Brazil, and the Central African Fold Belt. In: R. J. Pankhurst; R. A. J. Trouw; B. B. Brito Neves; M. J. De Wit (Orgs.); **West Gondwana: Pre-Cenozoic Correlations Across the South Atlantic Region (Special Publications)**. v. 294, p.69–99, 2008. London: Geological Society of London.

VAUCHEZ, A.; NEVES, S.; CABY, R. The Borborema shear zone system, NE Brazil. **Journal of South American Earth Sciences**, v. 8, n. 3–4, p. 247–266, 1995. **Vernon, 2004.**

VIEGAS, L. G. F.; ARCHANJO, C. J.; HOLLANDA, M. H. B. M.; VAUCHEZ, A. Microfabrics and zircon U-Pb (SHRIMP) chronology of mylonites from the Patos shear zone (Borborema Province, NE Brazil). **Precambrian Research**, v. 243, p. 1–17, 2014.

VIEGAS, L. G. F.; ARCHANJO, C. J.; VAUCHEZ, A. Fabrics of migmatites and the relationships between partial melting and deformation in high-grade transpressional shear zones: The Espinho Branco anatexite (Borborema Province, NE Brazil). **Journal of Structural Geology**, v. 48, p. 45–56, 2013.

VOLL, G. Recrystallisation of Quartz, Biotite, and Feldspars from Erstfeld to the Leventina Nappe, Swiss Alps, and its geological Significance. **Schweizerische Mineralogische und Petrographische Mitteilungen**, v. 56, n. 3, p. 641–647, 1976.

WEHRENS, P.; BERGER, A.; PETERS, M.; SPILLMANN, T.; HERWEGH, M. Deformation at the frictional-viscous transition: Evidence for cycles of fluid-assisted embrittlement and ductile deformation in the granitoid crust. **Tectonophysics**, v. 693, p. 66–84, 2016.

WENK, H. R. **Preferred Orientation in Deformed Metals and Rocks: An Introduction to Modern Texture Analysis**. Orlando: Academic Press, 1985.

WHEELER, J.; PRIOR, D. J.; JIANG, Z.; SPIESS, R.; TRIMBY, P. W. The petrological significance of misorientations between grains. **Contributions to Mineralogy and Petrology**, v. 141, p. 109–124, 2001.

WHITE, S. Geological Significance of Recovery and Recrystallization Processes in Quartz. **Tectonophysics**, v. 39, n. 1–3, p. 143–170, 1977.

WILLAIME, C.; CHRISTIE, J. M.; KOVACS, M. P. Experimental deformation of K-feldspar single crystals. **Bulletin de Minéralogie**, v. 102, n. 2–3, p. 168–177, 1979.

WILLAIME, C.; GANDAIS, M. Electron microscope study of plastic defects in experimentally deformed alkali feldspars. **Bulletin de la Société française de Minéralogie et de Cristallographie**, v. 100, n. 5, p. 263–271, 1977.

APÊNDICE 1 - SUPPLEMENTARY TABLE 1

Table 1 - Summarized sample descriptions of mylonites analysed in this study.

Sample	Fabric	Mineralogy (%)	Sample Description	Microstructures	
				Quartz	Feldspar
LMD-12 (HT)	Ultramylonite (Paleosome?)	Qtz(13) + Pl(48) + Kfs(13) + Bt(18) + Hbl(5)	Medium-grained polymineralic matrix intercalated with coarse-grained quartzo-feldspathic bands; Fabric cut by transgranular fractures along interphase boundaries filled with secondary minerals.	Isolated anhedral grains; common undulose extinction, deformation bands, subgrains and chessboard extinction. Occur as drop-like inclusions in feldspar grains or filling the interstices.	Common flame perthites; myrmekite; common undulose extinction, kink bands, deformation and bent twins.
LMD-11 (TM)	Protomylonite (Boudin of a Augen gneiss)	Qtz(16) + Pl(28) + Kfs(48) + Bt(5)	Fragmented feldspar porphyroclasts with seriate grain sizes cut by S-C surfaces which comprise fine-grained recrystallized aggregates, interconnected layers of biotite and quartz ribbons.	Equigranular elongated grains defining oblique foliation in ribbons; common deformation bands, subgrains and undulose extinction; form films along interstices and occur as drop-like inclusions in feldspar clasts.	Common perthites, undulose extinction, bent twins and myrmekite along high normal stress borders
LMD-01 (TM)	Protomylonite (Orthogneiss)	Qtz(28) + Pl(28) + Kfs(30) + Bt(12) ± Hbl(1)	Subelliptic and irregular feldspar porphyroclasts immerse in a matrix with quartz aggregates, quartz ribbons, biotite flakes and fine-grained recrystallized aggregates; fabric cut by C-C' type shear bands which separate domains with different compositions and transgranular fractures	Ameboid grains with dissection structures and left-over grains with polygonal subgrains in aggregates; equigranular elongated grains defining oblique foliation in ribbons; grains with undulose extinction, deformation bands and widespread formation of polygonal subgrain.	Common flame perthites, deformation twins, kink bands, sweeping undulose extinction and myrmekite along high normal stress borders; rare fracturing.
LMD-02 (TM)	Mylonite (Leucogranite-Orthogneiss Contact)	Qtz(39) + Pl(28) + Kfs(31) ± Bt(1)	Subelliptic, square-shaped and irregular Feldspar porphyroclasts immerse in a matrix with fine-grained recrystallized aggregates, quartz aggregates and quartz ribbons. Contact cut by micro-shear zone and orthogneiss layer cut but C'-type shear bands and transgranular fractures	Ameboid grains with dissection structures and left-over grains in rare aggregates; equigranular, slightly elongated polygonized grains defining oblique foliation in ribbons; Common undulose extinction, core-mantle structures, deformation bands and widespread formation of polygonal subgrain.	Common flame perthites, myrmekite along high normal stress borders, deformation twins, kink bands and sweeping undulose extinction; rare core-mantle structures and fracturing.
LMD-10 (LT)	Ultramylonite L-tectonite (orthogneiss)	Qtz(26) + Pl(57) + Kfs(6) + Bt(7) ± Hbl(2)	Equigranular feldspar aggregates with slightly elongated grains defining an oblique foliation, discontinuous quartz ribbons and aligned hornblende and biotite; Rare Kfs porphyroclasts.	Grains with sutured boundaries and fine grains along the borders; Common sweeping undulose extinction, deformation bands and fracturing.	Common flame perthites and fracturing in KFs grains; Pl grains are strain-free.
PSZ-21 (HT)	Diatexite (Espinho Branco)	Qtz(24) + Pl(23) + Kfs(39) + Bt(13)	Medium-grained biotite-rich bands with equigranular xenomorphic grains intercalated with coarse-grained quartz-feldspar bands; aligned biotite flakes define the foliation	Common undulose extinctions and deformation band.	Rare undulose extinction and flame perthites.
PSZ-17 (TM)	Mylonite (Metatexite)	Qtz(48) + Pl(24) + Bt(26) ± Kfs(1)	Medium-grained, equigranular, elongated, xenomorphic grains wrapped by interconnected layers of biotite flakes. Fabric cut by micro-shear zones and transgranular fractures along interphase boundaries.	Common undulose extinction, deformation bands and subgrains; fracturing along boundaries are frequent.	Strain-free grains with frequent fracturing along the boundaries.
PSZ-18 (LM)	Mylonite (Granite)	Qtz(18) + Pl(22) + Kfs(42) + Hbl(13) + Bt(5)	Subelliptic, tabular and sigmoidal Kfs porphyroclasts immerse in a fine-grained matrix with recrystallized banded aggregates of variable compositions, interconnected layers of hornblende and continuous quartz ribbons.	Elongated grains with slightly lobate boundaries; Common patchy undulose extinction, deformation bands and subgrains	Common flame perthites, undulose extinction and myrmekite along high normal stress borders; rare deformation bands and subgrains

APÊNDICE 2 - SUPPLEMENTARY FIGURE S1

Figure S1 – a) Additional pole figures displaying the (021) planes and [1-12] directions of plagioclase from the transitional mylonites LMD-01, LMD-02 and LMD-11. b) Correspondent Inverse pole figures with the planes and directions that define slip systems in plagioclase.

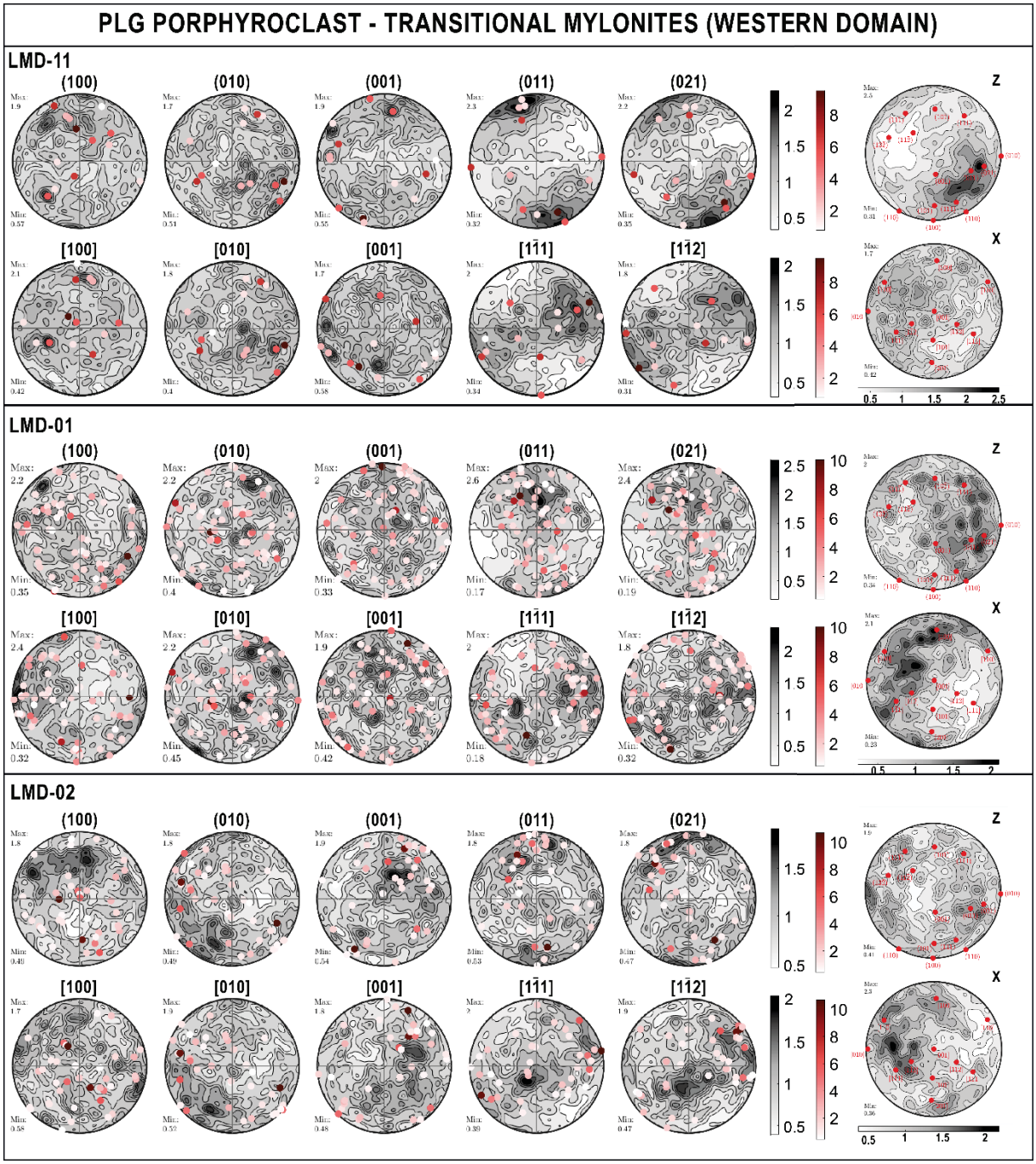

APÊNDICE 3 - SUPPLEMENTARY FIGURE S2

Figure S2 – EBSD data of K-feldspar porphyroclasts and the adject tail of recrystallized K-feldspar in the sample LMD-02. (a) Mis2Mean map of the Kfs porphyroclasts and grain orientation spread (GOS) maps of the (b) Kfs in recrystallized tails (Area I) and (c) recrystallized grains around the Kfs porphyroclasts (Area II). Pole figures for Kfs grains in (d) area I and (e) area II with respect the poles for Kfs porphyroclast color-coded according with the Mis2Mean. f) Misorientation angle distribution for the tail of recrystallized Kfs grains (area I).

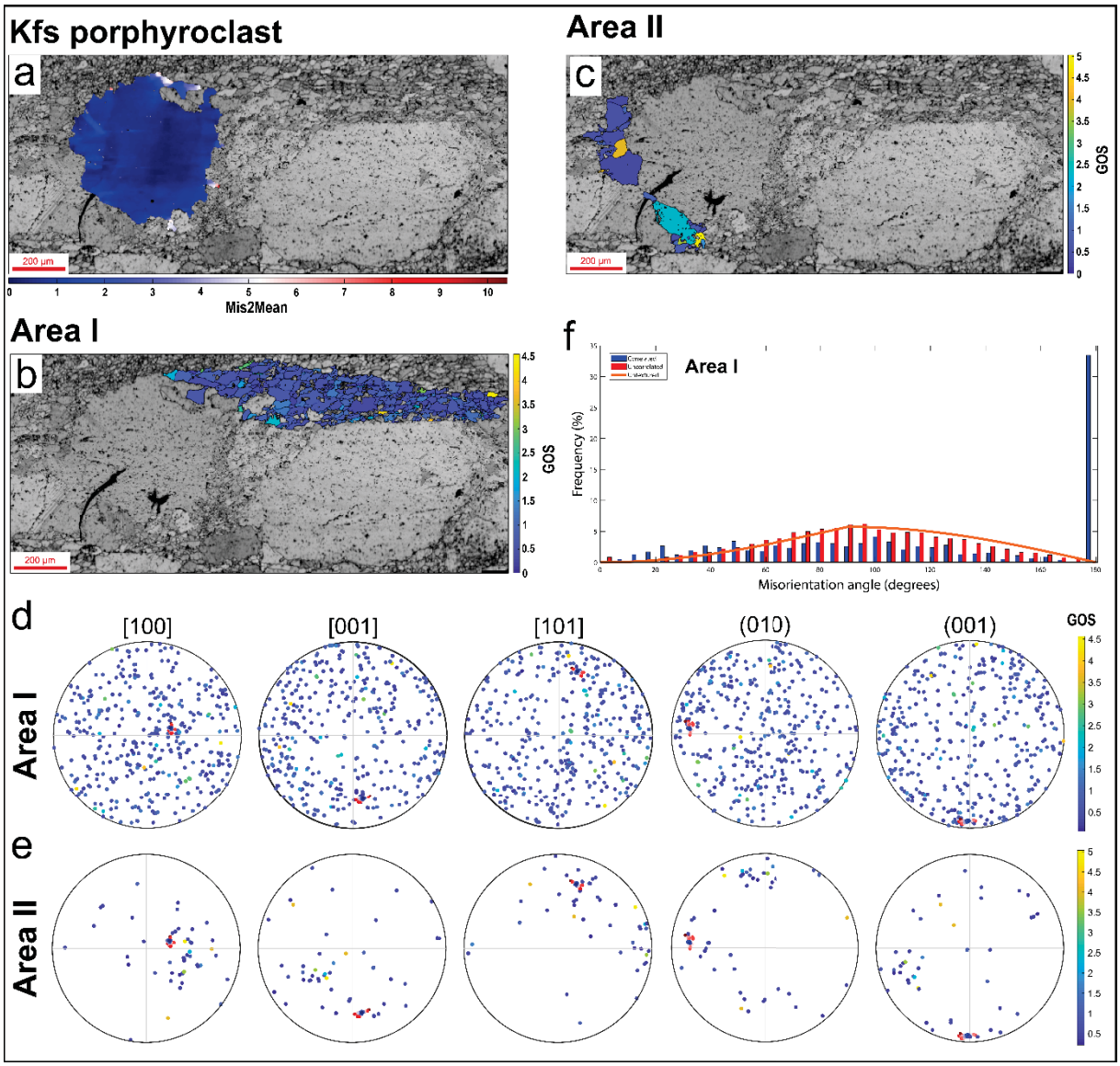

APÊNDICE 4 - SUPPLEMENTARY FIGURE S3

Figure S3 – Boundary trace and misorientation analysis of two plagioclase porphyroclasts in the sample LMD-02 (A and B). a) Mis2Mean map highlighting the high lattice distortion of Pl porphyroclasts expressed by the sweeping undulose extinction and deformation band. (a) Boundary trace analysis and (c) misorientation axes in crystal and specimen coordinate of Pl porphyroclast A. (e) Boundary trace analysis and (d) misorientation axes in crystal and specimen coordinate of Pl porphyroclast B.

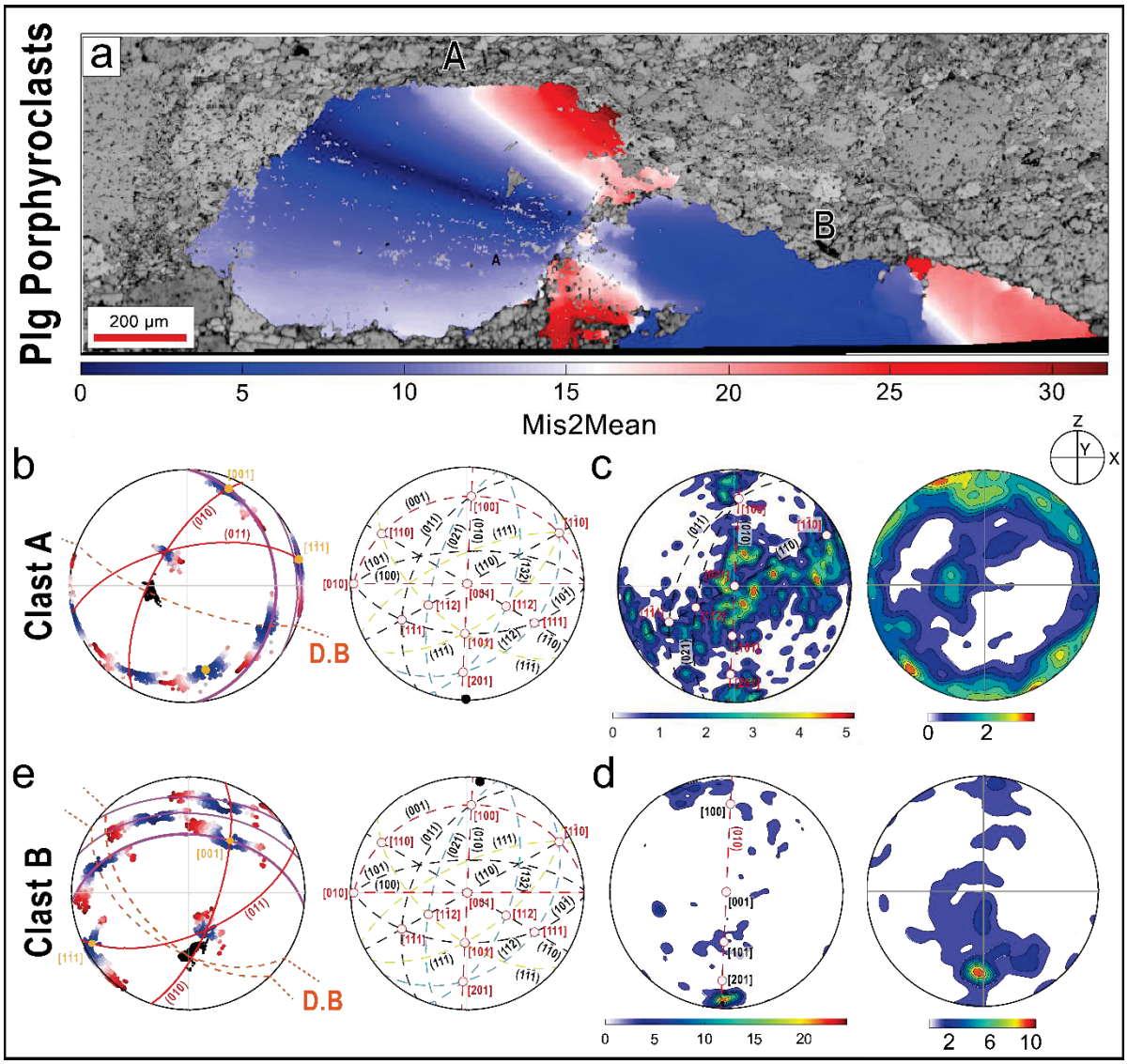

APÊNDICE 5 - SUPPLEMENTARY FIGURE S4

Figure S4 – a) EBSD map of a Kfs porphyroclast and the adjacent strain shadow with precipitated Kfs grains in the sample PSZ-18 indexed using both microcline (1) and monoclinic K-feldspar (2/m). b) Pole figures for the indexed microcline and orthoclase grains in the area correspondent to the porphyroclast. c) One pole per grain pole figures for the grains in the strain shadow.